NORTHWESTERN UNIVERSITY

Insights to Superconducting Radio-Frequency Cavity Processing from First Principles Calculations and Spectroscopic Techniques

A DISSERTATION

SUBMITTED TO THE GRADUATE SCHOOL
IN PARTIAL FULFILLMENT OF THE REQUIREMENTS

for the degree

DOCTOR OF PHILOSOPHY

Field of Chemical Engineering

By

Denise Christine Ford

EVANSTON, ILLINOIS

March 2013

© Copyright by Denise Christine Ford 2013

All Rights Reserved

ABSTRACT

Insights to Superconducting Radio-Frequency Cavity Processing from First Principles Calculations and Spectroscopic Techniques

Denise Christine Ford

Insights to the fundamental processes that occur during the manufacturing of niobium superconducting radio-frequency (SRF) cavities are provided via analyses of density functional theory calculations and Raman, infrared, and nuclear magnetic resonance (NMR) spectra. I show that during electropolishing fluorine is bound and released by the reaction of the acid components in the solution: $HF + H_2SO_4 <-> HFSO_3 + H_2O$. This result implies that new recipes can possibly be developed on the principle of controlled release of fluorine by a chemical reaction. I also show that NMR or Raman spectroscopy can be used to monitor the free fluorine when polishing with the standard electropolishing recipe.

Density functional theory was applied to calculate the properties of common processing impurities – hydrogen, oxygen, nitrogen, and carbon – in the niobium. These impurities lower the superconducting transition temperature of niobium, and hydride precipitates are at best weakly superconducting. I modeled several of the niobium hydride phases relevant to SRF cavities, and explain the phase changes in the niobium hydrogen system based on the charge transfer between niobium and hydrogen and the strain field inside of the niobium. I also present

evidence for a niobium lattice vacancy serving as a nucleation center for hydride phase formation. In considering the other chemical impurities in niobium, I show that the absorption of oxygen into a niobium lattice vacancy is preferred over the absorption of hydrogen, which indicates that oxygen can block these phase nucleation centers. I also show that dissolved oxygen atoms can trap dissolved hydrogen atoms to prevent niobium hydride phase formation. Nitrogen and carbon were studied in less depth, but behaved similarly to oxygen. Based on these results and a literature survey, I propose a mechanism for the success of the low-temperature anneal applied to niobium SRF cavities.

Finally, I present the beginning of a model to describe magnetic impurities in niobium SRF cavities, which can cause a loss of local superconductivity. I calculated magnetic configurations of niobium hydrides and oxides, and show that stoichiometric hydride and oxide structures are nonmagnetic, but defective oxide structures retain local magnetic moments.

ACKNOWLEDGEMENTS

I would like to thank my mentor, Dr. Lance Cooley at Fermilab, for his encouragement, support, and expertise in SRF cavity science and technology. I am also grateful for the many opportunities that he has provided for me to attend conferences, workshops, and specialized schools, where I was able to gain very specialized knowledge and expand my professional network. I would also like to thank Prof. David Seidman for welcoming me into his group at Northwestern University and his expertise in metallurgy.

This thesis benefited from collaborations with experimentalists at several institutions. I would like to thank Chad Thompson at Fermilab for handling the acids and discussions about electropolishing, Donald Bouchard at Anasazi Instruments, Inc. for obtaining nuclear magnetic resonance spectra and for thoughtful discussions, and Prof. Sandra Whaley Bishnoi at the Illinois Institute of Technology (IIT) for advising the Raman experiments and chemical analyses. I am also grateful to Brian Albee and Chaoyue Cao at the Illinois Institute of Technology for obtaining Raman spectra, and Donna Hicks at Fermilab for managing the chemical facilities.

My work has also benefited from discussions with Dr. Charlie Cooper at Fermilab, my officemate at Fermilab and fellow Ph.D. student Alex Dzyuba, Prof. John Zasadzinski at IIT, and many others at Fermilab, Northwestern University, and members of the Universities Collaboration.

I am also grateful to the Joint University – Fermilab Doctoral Program in Accelerator Physics and Technology for sponsoring my thesis research and the computational resources at Fermilab. Fermilab is operated by Fermi Research Alliance, LLC under Contract No. De-AC02-07CH11359 with the United States Department of Energy.

My career path has been inspired by many people and experiences over the years. I am particularly grateful to Prof. Manos Mavrikakis and his research group at the University of Wisconsin – Madison for inspiring and encouraging me to pursue a Ph.D. in chemical engineering and for introducing me to computational materials modeling. I am also grateful to my uncle Gerry Bellendir for introducing me to the world of physics and Fermilab.

Finally, I would like to thank my mom, Jackie Ford, and my sister, Parisa Ford, for their support and encouragement. My mom has made countless sacrifices for me and has always had faith in my abilities and my sister has never failed to recognize my nerdiness.

LIST OF ACRONYMS AND SYMBOLS

AC – alternating current

BCP – buffered chemical polishing

BCS – Bardeen, Cooper, Schrieffer

DC – direct current

DFT – density functional theory

DOS – densities of states

EP – electropolishing

FSA – fluorosulfonic acid

GAMESS – General Atomic and Molecular Electronic Structure System

GGA – generalized gradient approximation

HFA – hydrofluoric acid

ILC – International Linear Collider

IR – infrared

LDA – local density approximation

NMR – nuclear magnetic resonance

PAW – Projector-augmented wave

PBE – Perdew, Burke, Ernzerhof

RF – radio-frequency

RRR – residual resistivity ratio

SA – sulfuric acid

SRF – superconducting radio-frequency

VASP – Vienna Ab initio Simulation Package

ZPE – zero point energy

bcc – body-centered cubic

fcc – face-centered cubic

fco – face-centered orthorhombic

E, E_0 – energy, ground state energy

E^H – Hartree (electron-electron repulsion) energy

E_{xc} – exchange-correlation energy

$\vec{G}$ – reciprocal lattice vector

H_{c1} – lower critical magnetic field

H_{c2} – upper critical magnetic field

H_{RF} – radio-frequency field amplitude

H_{sh} – superheating critical field

$\hat{H}$ – Hamiltonian operator

J – on-site exchange energy

Q – quality factor

R – ratio of fluorine associated with hydrofluoric acid to fluorosulfonic acid

R_{BCS} – BCS surface resistance

R_{res} – residual resistance

R_s – total surface resistance

S – spin quantum number

T – temperature

T_c – superconducting transition temperature

T_s – kinetic energy of the non-interacting system

$\vec{T}$ – periodic length

U – on-site Coulomb energy

$V_{N\text{-}e}$ – nuclear-electronic interaction energy

a – lattice parameter

g – Landé g-factor

h, ħ – Planck's constant, reduced Planck's constant

k_B – Boltzmann's constant

$\vec{k}$ – wave vector

m – mass of a particle

$\vec{r}$ – vector distance between particles

t – time

v_F – Fermi velocity

α, α', β, δ, ε, λ, λ_c – niobium hydride phases

Δ – superconducting energy gap

ϕ_i, ϕ_i^{KS} – one-electron orbitals, Kohn-Sham orbitals

λ, λ_L – magnetic field penetration depth, London penetration depth

μ_B – Bohr magneton

μ_0 – permeability of free space

ν_i – frequency of ith vibrational mode

ρ, ρ_0, ρ_s– electron density, ground state electron density, electron density of the fictitious system

ξ – Cooper pair coherence length

Ψ - wave function

TABLE OF CONTENTS

ABSTRACT 3

ACKNOWLEDGEMENTS 5

LIST OF ACRONYMS AND SYMBOLS 7

TABLE OF CONTENTS 11

LIST OF TABLES 13

LIST OF FIGURES 15

1. INTRODUCTION 17

2. BACKGROUND 20
- Superconducting Radio-Frequency Cavity Design and Material 20
  - *Fundamentals* 20
  - *Impurities in Niobium* 22
- Superconducting Radio-Frequency Cavity Processing 24
- Superconducting Radio-Frequency Cavity Performance Limitations 31

3. METHODS 35
- Calculations Based on Density Functional Theory 35
- Experimental Tools 40

4. ELECTROPOLISHING SOLUTION ANALYSES 42
- Abstract 42
- Introduction 42
- Methods 42
- Results 43
  - *Raman Spectra* 43
  - *Infrared Spectra* 49
  - *Nuclear Magnetic Resonance Spectra* 52
- Discussion 54

5. NIOBIUM HYDRIDE PHASE FORMATION 57
- Abstract 57
- Introduction 57
- Methods 58
- Results and Discussion 60

Dissolved Hydrogen in Body-Centered Cubic Niobium 60
Interaction Between Hydrogen and Niobium Lattice Vacancies 62
Geometric and Electronic Aspects of Niobium-Hydride Phase Changes 64
Application to Niobium Superconducting Radio-Frequency Cavities 69
Summary and Conclusions 72

6. SUPPRESSION OF HYDRIDE PRECIPITATES 74
Abstract 74
Introduction 75
Methods 76
Results and Discussion 77
Interstitial Hydrogen, Oxygen, Nitrogen, and Carbon Atoms 77
Hydrogen Trapping by Other Interstitial Impurities 79
Hydrogen and Oxygen Trapping by Niobium Lattice Vacancies 82
Implications for Superconducting Radio Frequency Cavity Processing 84
Summary and Conclusions 88

7. MODELING MAGNETIC IMPURITIES IN NIOBIUM 90
Abstract 90
Introduction 90
General Models and Methods 91
Stoichiometric Niobium Hydrides and Oxides 92
Defective Oxides 95
Discussion 97

8. CONCLUSIONS AND FUTURE WORK 100

REFERENCES 103

APPENDIX 1 – CALCULATIONS OF THE VIBRATIONAL SPECTRA OF ELECTROPOLISHING SOLUTION SPECIES 118

APPENDIX 2 – CALCULATIONS OF THE PHONON SPECTRA OF THE OXIDES AND HYDRIDES OF NIOBIUM 121

VITA 125

LIST OF TABLES

Table 4.1. Raman peaks in the EP solution and sulfuric acid (SA) spectra. 45

Table 4.2. Raman and IR peaks of niobium-fluoride salts from [82]. 48

Table 4.3. IR peaks in new EP solution, sulfuric acid (SA), hydrofluoric acid (HFA), and water spectra. 52

Table 4.4. The fluorine distribution in mixtures of 96 % sulfuric acid (SA), 49 % hydrofluoric acid (HFA), fluorosulfonic acid (FSA), and water determined from ^{19}F NMR measurements. 55

Table 5.1. Charges and energetics of hydrogen in bcc niobium tetrahedral interstices. 61

Table 5.2. Charges on niobium atoms bound to hydrogen atoms and on the hydrogen atoms; absorption energies of hydrogen atoms in niobium lattice vacancies referred to the absorption energy of hydrogen atoms in tetrahedral interstitial sites; and lattice strain energies referred to the lattice strain energy of hydrogen atoms in tetrahedral interstitial sites. 63

Table 5.3. Charges on niobium atoms bound to hydrogen atoms and on the hydrogen atoms; absorption energies of hydrogen referred to bcc niobium and gas phase hydrogen molecules; and self-trapping and lattice strain energies caused by the absorption of hydrogen. 68

Table 6.1. Charges on the niobium atoms bonded to the interstitial impurity atoms – H, O, N and C – and on the interstitial impurities; binding energies of the interstitial impurities absorbed into a bcc niobium lattice interstitial site referred to bcc niobium and the impurity species as an atom in the gas phase; and the lattice strain energies caused by the impurity species residing in the interstice. 78

Table 6.2. Nb-interstitial impurity bond lengths. 78

Table 6.3. Charges on niobium atoms bonded to an impurity atom and on the impurity atoms; and binding and lattice strain energies of the impurity atoms in niobium lattice interstitial sites and vacancies referred to the isolated impurity atoms located in their preferred interstitial sites. 83

Table 6.4. Nb-impurity bond lengths when an impurity atom is located in a niobium lattice vacancy. 83

Table A1.1. Vibrational frequencies and Raman and IR intensities for the gas phase model of plausible species existing in the electropolishing solution. 119

Table A2.1. Vibrational frequencies of interstitial impurity atoms in the bcc niobium lattice from DFT calculations. 122

LIST OF FIGURES

Figure 2.1. Schematic of a TESLA style 9-cell SRF cavity. 20

Figure 2.2. Nb-H phase diagram from [23], which was based on the data in [32]. 24

Figure 2.3. Schematic of a Nb electropolishing cell. 26

Figure 2.4. Schematic of a niobium electropolishing polarization curve. 27

Figure 2.5. Schematic of cavity performance characterization curves exemplifying the impurity related limitations, Q-disease and Q-slope. 32

Figure 3.1. Schematic energy level diagram of some photon interactions with matter. 41

Figure 4.1. Raman spectra of new (unused) EP solution, its components (49 % hydrofluoric acid in water (HFA) and 96 % sulfuric acid (SA)), and the sample container. 44

Figure 4.2. Raman spectra of 1 volume 96% sulfuric acid (SA) diluted with 1 volume water. 45

Figure 4.3. Raman spectra of 49 % hydrofluoric acid (HFA) diluted with water; the ratios are by volume. 46

Figure 4.4. Raman spectra of new (unused) EP solution, 80 vol. % EP solution + 20 vol. % fluorosulfonic acid (FSA), 80 vol. % EP solution + 20 vol. % water, and used EP solution. 47

Figure 4.5. Infrared spectra of new (unused) EP solution and its components (49 % hydrofluoric acid (HFA) in water and 96 % sulfuric acid (SA)). 49

Figure 4.6. Infrared spectra of 49 % hydrofluoric acid (HFA) diluted with water; the ratios are by volume. 50

Figure 4.7. Infrared spectra of 1 volume 96% sulfuric acid (SA) diluted with 1 volume water. 50

Figure 4.8. Infrared spectra of new (unused) EP solution, 80 vol. % EP solution + 20 vol. % fluorosulfonic acid (FSA), 80 vol. % EP solution + 20 vol. % water, and used EP solution. 51

Figure 4.9. ^{19}F NMR spectra of new (unused) EP solution, 80 vol. % EP solution + 20 vol. % fluorosulfonic acid (FSA), 80 vol. % EP solution + 20 vol. % water, and used EP solution. 53

Figure 4.10. ^{19}F NMR spectra of 48 % hydrofluoric acid (HFA) diluted with various amounts of water and 95 % sulfuric acid (SA); the ratios are by volume. 54

Figure 5.1. Geometry of hydrogen dissolved in a niobium tetrahedral interstice (a) and a niobium lattice vacancy (b). 61

Figure 5.2. Energy difference between the niobium hydride phases and isolated hydrogen atoms in niobium tetrahedral interstices vs. hydrogen concentration. 65

Figure 5.3. Unit cell expansion (a is the lattice parameter) vs. hydrogen concentration. 66

Figure 5.4. Energetic comparison of relevant configurations of hydrogen and niobium. 71

Figure 6.1. Illustration of (a) tetrahedral, (b) octahedral, and (c) vacancy binding sites in bcc niobium. 79

Figure 6.2. Plot of binding energy, referred to a hydrogen atom in a bcc niobium tetrahedral interstice and an oxygen atom in an infinitely far away octahedral interstice, versus the distance between an oxygen atom in an octahedral interstice and a trapped hydrogen atom in a nearby tetrahedral interstice. A diagram of the lowest-energy configuration is also shown. 81

Figure 7.1. Total electronic DOS of bulk niobium, niobium hydrides, and niobium oxides. 93

Figure 7.2. The P2, also called h-, Nb_2O_5 structure. 95

Figure 7.3. The energy to form one oxygen vacancy from the P2 structure of Nb_2O_5 versus the total magnetic moment of the $Nb_{28}O_{69}$ unit cell. 96

Figure 7.4. Illustration of the creation of the lowest-energy configurations of $Nb_{28}O_{69}$ from P2 Nb_2O_5. 97

Figure A2.1. Phonon DOS of crystalline niobium oxides and hydrides. 123

Figure A2.2. Raman spectra of the edge of a topographical defect and a smooth spot of a niobium sample cutout from a cavity high-field Q-slope hot spot. 124

CHAPTER 1. INTRODUCTION

Superconducting radio-frequency (SRF) cavities are a key developing technology for high-performance linear particle accelerators. SRF cavities will be used in high-energy physics applications including Project X, which is a proposed 8 GeV proton source at Fermilab, and thInternational Linear Collider (ILC), which is a proposed positron-electron collider that would be created as an international collaboration to compliment the experiments performed at the Large Hadron Collider at CERN. This technology can also be used for waste management from nuclear power sources by transforming dangerous long-lived isotopes to more manageable ones, and synchrotron light and neutron sources for physical, chemical, biological, medical, and materials science research. SRF technology is currently employed in accelerators at several national laboratories, but this technology must be optimized and industrialized for future high performance applications.

SRF cavities offer a significant advantage over regular conducting cavities in that the losses due to surface resistance are reduced by five to six orders of magnitude. Operating in the superconducting state, however, requires very high purity materials with low surface roughness, and manufacturing SRF cavities to meet the requirements for ILC level performance has proved to be difficult. The ILC will require cavities to operate at an accelerating gradient of 31.5 MV/m and to withstand a peak electric field of over 63 MV/m and a peak magnetic field of over 134 mT [1].

SRF cavity performance is characterized by the accelerating gradient and the quality factor (Q, a measure of the stored energy versus the dissipated power), both of which are highly sensitive to the surface state of the cavity. Performance limitations include enhanced electron field emission, which is caused by the tunneling of electrons at sharp asperities to the interior of the cavity and is sensitive to contaminants on the surface such as dust particles or surface topography; multipacting, which is caused by release of electrons from the cavity material which are subsequently accelerated and impinged back onto the cavity's surface and is sensitive to the cavity shape; Q-disease, which the cause is unknown but is sensitive to impurities (specifically hydrogen) in the cavity material; and Q-drop or Q-slope, which the cause is also unknown but can be mitigated by mild heat treatment of the cavity.

Although many studies have been performed to understand the effects of processing SRF cavities on cavity performance, little is known about the fundamental mechanisms of these processes [2]. This thesis provides insights to some of the fundamental mechanisms of the empirically developed cavity processing procedures. Density functional theory (DFT) and Raman, infrared (IR), and nuclear magnetic resonance (NMR) spectroscopy have been employed to study the acid solution utilized in the electropolishing of the cavities, which provides insight to the chemical mechanisms occurring during this process. DFT has also been used to study the properties of chemical impurities in the cavity material, which provides insight to the mechanisms of the heat treatments applied to cavities. Finally, preliminary models of magnetic impurities were created, which may eventually lead to additional insight to the effects of cavity processing on performance. This thesis benefited from collaborations with experimental scientists at Fermi

National Accelerator Laboratory, the Illinois Institute of Technology, and Anasazi Instruments, Inc.

CHAPTER 2. BACKGROUND

Superconducting Radio-Frequency Cavity Design and Material

Fundamentals

An example of the geometry of a cavity that will employ SRF technology is the 9-cell TESLA design [3], which will be used in the ILC and is shown in Figure 2.1. This type of cavity accelerates particles with an electric field that switches sign at a radio frequency (RF). The length of each cell is designed to be half of the RF wavelength, the elliptical shape of the cells has been optimized to prevent multipacting, and the number of cells has been optimized to provide efficient particle acceleration while maintaining production and tuning feasibility [4].

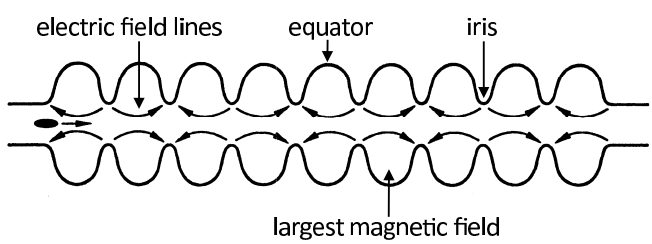

Figure 2.1. Schematic of a TESLA style 9-cell SRF cavity.

Niobium is the current material of choice for SRF cavities because it has both favorable superconducting properties [5] and is highly malleable. Niobium is a type II superconductor, characterized by two critical magnetic fields (H_{c1} and H_{c2}). Below H_{c1} and the superconducting transition temperature (T_c), niobium is in the superconducting state, where zero DC electrical resistance and the Meissner effect (magnetic flux is expelled from the bulk metal) are observed. The normal conducting state, in which magnetic flux penetrates the niobium and electrical resistance is present, is experienced above H_{c2}. A mixed state exists between H_{c1} and H_{c2}, where

magnetic flux tubes penetrate the bulk niobium, but are shielded by vortex currents. The time required to nucleate vortices is long compared to the RF period in SRF cavities, therefore in this situation an additional metastable superheating state exists, where superconductivity is still observed above H_{c1} and persists until the superheating critical field H_{sh}. The critical temperature and fields for niobium are $T_c = 9.2$ K, $B_{c1} = \mu_0 H_{c1} = 174$ mT, and $B_{c2} = \mu_0 H_{c2} = 400$ mT [6]; μ_0 is the permeability of free space.

Even in the superconducting state, the magnetic field penetrates the surface of a superconductor, but decays rapidly inside of a small depth [7]. The characteristic depth is the London penetration depth, λ_L, which is ~40 nm for niobium [6]. The Bardeen-Cooper-Schrieffer (BCS) theory [8] provides a microscopic description of superconductivity, in which it is explained that a supercurrent is carried by pairs of electrons, each with opposite spin and momentum, called Cooper pairs. The electrons pair below the superconducting transition temperature because the deformation caused to the lattice by one electron moving through the lattice creates a favorable path for the second electron to follow. Therefore, superconductors have a second characteristic length, the Cooper pair coherence length, ξ_0 [9], which is interpreted microscopically as the minimum distance between electrons in a pair and is ~38 nm for niobium [6]. The London penetration depth and Cooper pair coherence length are intrinsic properties of a pure superconductor; however, the penetration depth, λ, and coherence length, ξ, of a real material depend on purity through the electron mean free path and on temperature. Cooper pairs occupy the BCS ground state, which is lower in energy than the single electron ground state by $2\Delta(T)$,

where $\Delta(T)$ is the characteristic superconducting energy gap. BCS theory predicts the $\Delta(0)=1.76k_BT_c$, which varies slightly for real materials; k_B is Boltzmann's constant.

In the RF case, the alternating electric field causes a build up of electric current due to surface resistance and some power dissipation will occur in the superconducting state. The total surface resistance of a superconductor, R_s, is the sum of the inherent surface resistance described by BCS theory, R_{BCS}, and the residual resistance, R_{res}. R_{BCS} is a function of a superconductor's material properties, the radio frequency, and temperature. R_{res} results from defects, impurities in the superconductor, and impurities on the surface, and is typically 3 nΩ or larger [4]. The surface resistance is inversely proportional to the cavity's quality factor, Q_o.

Impurities in SRF Niobium

Common impurities in SRF niobium include hydrogen, oxygen, nitrogen, and carbon [10]. Niobium sheet specifications restrict the concentrations of dissolved oxygen, nitrogen, and carbon to <30 mass ppm (200 atomic ppm) [11]; however, oxygen is readily available for absorption and dissolution into the niobium during SRF cavity processing. The niobium surface grows an oxide coating when exposed to air or water, which is composed of layers of Nb_2O_5, NbO_2, NbO, and a gradient of dissolved oxygen in the niobium bulk. In pure form, NbO is metallic, NbO_2 is a Peierls semiconductor, and Nb_2O_5 is an insulator. The niobium oxides exist in broad ranges of stoichiometries; and some of these harbor local magnetic moments [12]. This is detrimental for superconductivity because magnetic impurities can create normal conducting states within Δ, and therefore lower T_c [13]. Dissolved oxygen can be present deep into the

niobium bulk and decreases niobium's T_c by ~1 K / at. % [14]. The distribution of oxygen in the oxide layers and bulk niobium is affected by the heat treatments applied to SRF cavities during processing [15-17].

SRF niobium typically contains a substantial amount of hydrogen, particularly in the top ~50 nm of the subsurface [18-22]. Hydrogen is easily absorbed into niobium during cavity processing [23], and can become trapped near the interface between the oxide and bulk niobium [24-27]. Dissolved hydrogen causes a reduction of the niobium T_c [28] and several of the ordered niobium hydride phases are not superconducting above 1-2 K [24, 29, 30].

The niobium-hydrogen phase diagram is shown in Figure 2.2. Several factors, aside from temperature and concentration, can affect the formation of hydrides. As discussed in a review by Khaldeev and Gogel [26], dissolved hydrogen atoms can become trapped by several mechanisms: (1) the elastic strain that they impart to the niobium lattice upon absorption, known as self-trapping; (2) interaction with other dissolved impurities; and (3) absorption into lattice imperfections – point, line and planar. Trapping enthalpies and their effects on hydrogen's diffusivity have been evaluated experimentally, and theoretical models have been constructed to include elastic, electronic, and tunneling contributions – a book by Fukai [31] provides detailed information about these topics as well as references to many prior studies. Fundamental pieces of information about the behavior of hydrogen in niobium are still missing, however, and are assessed via first principles calculations in this thesis.

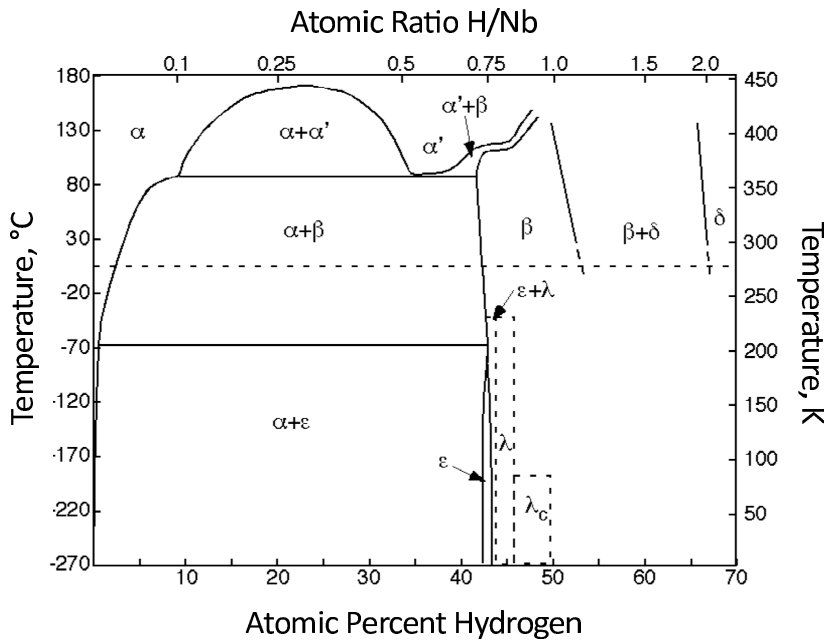

Figure 2.2. Nb-H phase diagram reproduced with permission from [23], which was based on the data in [32]. The α and α' niobium hydride phases consist of interstitial hydrogen atoms dispersed in body-centered cubic (bcc) niobium at differing low hydrogen concentrations, the β phase consists of face-centered orthorhombic (fco) niobium with ordered hydrogen interstitials and with an ~NbH stoichiometry, the δ phase has the fluorite structure with hydrogen in the tetrahedral sites of face-centered cubic (fcc) niobium and an ~NbH_2 stoichiometry, the ε phase is structured like the β phase with the ~Nb_4H_3 stoichiometry, and λ and λ_c phases are experimentally unconfirmed niobium hydride phases.

Superconducting Radio-Frequency Cavity Processing

SRF cavities undergo an intricate processing regimen to maximize the cavity quality factor and accelerating gradient, during which multiple chemical polishing and high vacuum annealing steps are coordinated. Typically the regimen includes plastic forming of the cavity, heavy chemical polishing to remove ~150 μm of the niobium surface, high-vacuum annealing at 600 or 800 °C and < 10^{-6} torr (hereafter called the high-temperature anneal), final chemical polishing to remove ~ 20 μm of the surface, and final high-vacuum annealing at 120 – 160 °C and < 10^{-6} torr (hereafter called the low-temperature anneal). Since the RF properties are determined over a few

magnetic penetrations depths, the regimen employed produces an empirical optimization of the near-surface nanostructure and nanocomposition. The detailed atomic and sub-atomic scale mechanisms at work in these processes remain elusive, however.

The detailed chemical mechanisms comprising the electropolishing process (which falls under the category of chemical polishing in the above list) are of concern particularly because this process has the capability to limit cavity performance by several mechanisms: hydrogen, oxygen, and other chemicals can become imbedded and dissolved in the surface, preferential etching can occur at grain boundaries or preexisting defects from the plastic forming steps of the cavities, or new defects can be created. Electropolishing is utilized in cavity processing because it reduces the roughness of a cavity's surface and removes the damaged layer created by forming the cavity, both reduce R_s and therefore increase Q [33]. Furthermore, cavities have complex geometries, which make the application of chemical polishing simpler than mechanical polishing, and electropolishing has proven industrial effectiveness. Other chemical polishing procedures, such as buffered chemical polishing (BCP), have been developed and are used for accelerator cavity applications; however, electropolished cavities demonstrate superior performance at higher accelerating gradients, therefore electropolishing is preferred when the required gradient is greater than 25 MV/m [34]. For these reasons, electropolishing remains in the cavity processing procedure and post-polishing procedures have been developed to correct the damage created by this process. These include high-pressure rinsing to clean the cavity's surface and high-temperature annealing to outgas absorbed hydrogen [35]. Laser melting is being developed to correct topographical defects [36]. However, better understanding of the

electropolishing process may lead to improvements in the process and potentially eliminate the need for post-processing corrections.

Electropolishing is accomplished with an electric current and viscous electrolyte, as shown schematically in Figure 2.3. The metal part to be polished forms the anode of the electrochemical cell, and a counter electrode serves as the cathode. Negatively charged ions attack and dissolve the metal at the anode, while a viscous solution is used to control the diffusion of these ions and therefore the polishing rate.

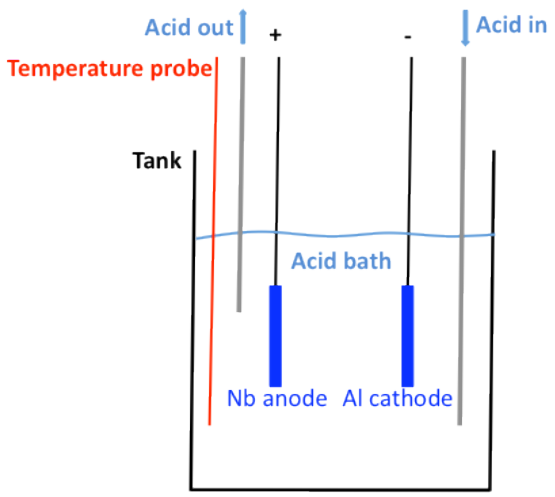

Figure 2.3. Schematic of a Nb electropolishing cell.

A general description of the electropolishing process mechanism as given by Tegart [37] is summarized here. The electropolishing process consists of two mechanisms: smoothing, where irregularities on the order of microns are removed, and brightening where irregularities as small as nanometer scale are eliminated. The diffusion of reaction products away from the anode directly affects the smoothing mechanism and the thin film formed on the surface of the anode

directly affects the brightening mechanism. The movement of ions is controlled by the current density, which is related to the applied DC voltage. The specific current - voltage relationship is determined experimentally, and contains the features shown in Figure 2.4. Polishing should occur near the upper end of the current plateau, where the process will be controlled by the diffusion of ions to the anode surface. Crystallographic etching occurs prior to the peak current, and gas bubble evolution, which creates surface imperfections, occurs after the plateau. Enhancement of surface defects, such as etching around grain boundaries, may occur in any of the polishing regions. Agitation and temperature must also be carefully controlled [38]. Agitation helps the active ions approach the surface, however, over-agitation disrupts the viscous layer formed on the anode surface causing pitting and etching. Temperature has an indirect effect on the electropolishing process in that increased temperature decreases the solution viscosity and increases the current density.

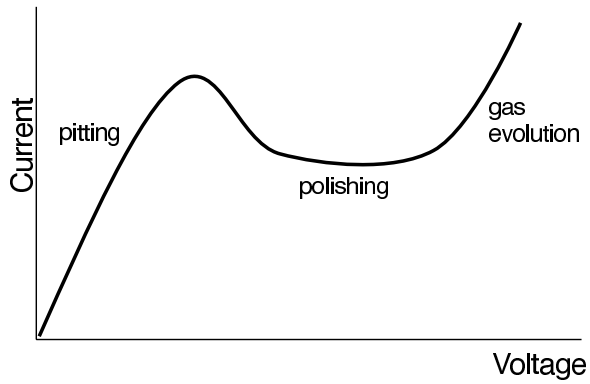

Figure 2.4. Schematic of a niobium electropolishing polarization curve.

Multiple processes for electropolishing SRF cavities are being developed, but since only the inner surface of an SRF cavity needs to be polished, the cathode is inserted through the center of the cavity and the cavity is filled with the electropolishing solution. In the standard recipe [39,

40] aluminum is used for the cathode and a 1:9 volume ratio of 49 % hydrofluoric acid, which provides the active polishing ion F^-, and 96 % sulfuric acid, which provides the viscous medium, comprise the solution. This recipe is not ideal from the standpoint of the safety and environmental impact associated with hydrofluoric acid.

Niobium electropolishing chemistry is a balance between processes that oxidize the metal, and those that dissolve the oxide. It is characterized by the following reactions [41]:

electro-oxidation:	$2Nb + 5SO_4^{2-} + 5H_2O \rightarrow Nb_2O_5 + 10H^+ + 5SO_4^{2-} + 10e$	R1
dissolution:	$Nb_2O_5 + 6HF \rightarrow H_2NbOF_5 + NbO_2F \cdot 0.5H_2O + 1.5H_2O$	R2
product formation:	$NbO_2F \cdot 0.5H_2O + 4HF \rightarrow H_2NbOF_5 + 1.5H_2O$	R3
overall:	$2Nb + 10HF + 2H_2O \rightarrow 2H_2NbOF_5 + 5H_2$	R4

Because electropolishing is an electrochemical process, one can expect oxidation reactions to occur at the anode (niobium surface) and reduction reactions to occur at the cathode (aluminum surface). The electrochemical oxidization reactions of niobium are [42]:

$NbO + 2H^+ + 2e^- \rightarrow Nb + H_2O$	$E_o = -0.733 - 0.0591\ pH$	R5
$NbO_2 + 2H^+ + 2e^- \rightarrow NbO + H_2O$	$E_o = -0.625 - 0.0591\ pH$	R6
$Nb_2O_5 + 2H^+ + 2e^- \rightarrow NbO_2 + H_2O$	$E_o = -0.289 - 0.0591\ pH$	R7

The Pourbaix diagram [42] shows that NbO_2 and NbO are unstable in aqueous solutions at any pH, so the oxide will continue to develop until the stable Nb_2O_5 is reached.

During electropolishing, Nb_2O_5 is dissolved by hydrofluoric acid, and the dissolved niobium is retained in solution with a complexing agent. Several plausible reactions involving niobium and the electropolishing component acids have been compiled by [43] and are summarized below. The dissolution reactions include:

$$Nb_2O_5 + 14\ HF \leftrightarrow 2\ H_6NbO_2F_7 + H_2O \qquad \text{R8}$$

$$Nb_2O_5 + 12HF \leftrightarrow 2HNbF_6 + 5H_2O \qquad \text{R9}$$

$$Nb_2O_5 + 10HF \leftrightarrow 2NbF_5 + 5H_2O \qquad \text{R10}$$

$$Nb_2O_5 + 10HF \leftrightarrow 2H_2NbOF_5 + 3H_2O \qquad \text{R11}$$

Niobium pentoxide is also dissolved by sulfuric acid according to the reaction:

$$Nb_2O_5 + nH_2SO_4 \rightarrow Nb_2O_{5-n}(SO_4)_n + nH_2O \qquad \text{R12}$$

but the reactivity is negligible compared to the action of hydrofluoric acid. Sulfuric acid, however, is efficient as a complexing agent, which may react with the dissolved niobium according to any of the following reactions:

$$NbF_5 + 2(SO_3, H_2O) \leftrightarrow NbF_3(SO_3F)_2, 2\ H_2O \qquad \text{R13}$$

$$2NbF_5 + 14SO_3 \leftrightarrow Nb_2O(SO_4)_4 + 5S_2O_5F_2 \quad \text{R14}$$

$$2NbF_5 + (5\text{-}n)H_2SO_4 + nH_2O \rightarrow Nb_2O_n(SO_4)_{5\text{-}n} + 10HF, \text{ where } n = 1\text{-}4 \quad \text{R15}$$

In addition to the electropolishing reactions, sulfuric acid and hydrofluoric acid may react with each other in solution according to the reaction [44]:

$$H_2SO_4 + HF \rightarrow H_2O + HFSO_3 \quad \text{R16}$$

Chemical contamination of SRF cavities may occur by adsorption and absorption of any of the species present in the electropolishing solution. Evidence for oxygen, hydrogen, and sulfur has been found in several studies [45-47]. Oxygen contamination occurs by the oxidation processes discussed previously. Hydrogen easily becomes imbibed by the niobium during start up and shut down of the electropolishing process when the current is not drawing it to the cathode. Sulfur contamination may occur from sulfuric acid interaction with the niobium surface, but additionally, dissolved sulfur is present in the electropolishing solution from reactions at the aluminum cathode.

Some effort has been extended to improve the electropolishing process by changing the chemical recipe, such as by adding lactic acid to increase the solution's viscosity, therefore offering superior control over the process [48], or eliminating hydrofluoric acid therefore reducing the hazard and environmental impact of the process [49]. Better understanding of the chemical mechanism of electropolishing will aid in the development of new recipes.

Superconducting Radio-Frequency Cavity Performance Limitations

The primary performance limitations related to impurities absorbed in niobium are Q-disease and Q-slope, which appear in cavity characterization curves as shown Figure 2.5. It was clear over 40 years ago [50] that the chemical polishing of a niobium surface results in a complicated interplay between hydrogen uptake, surface topographical features, and other atomic contaminants, such as oxygen, nitrogen, and carbon atoms [51]. Numerous reports, see the review by Knobloch [52], describe how SRF cavities tested immediately after heavy chemical polishing developed a rapid drop of Q starting with zero accelerating gradient, a phenomena called "Q-disease". Knobloch explains that a comparison of the phase diagrams, concentrations, diffusivities, and ability to enter or exit niobium during processing of these common impurities and cavity cool down rate versus performance statistics led to the belief that hydrogen is responsible for Q-disease. Quantitative evaluation of hydrogen in SRF cavities has been, however, difficult; and in situ observations have not been possible. Even direct observations of precipitates in coupons and cavity cut-outs via scanning electron microscopy and transmission electron microscopy have only recently been presented [18, 53]. Nevertheless, hydrogen is observed by residual gas analysis during high-vacuum annealing at 600 or 800 °C, which correlates with improved cavity performance, and thereby supports a connection between hydrogen and Q-disease.

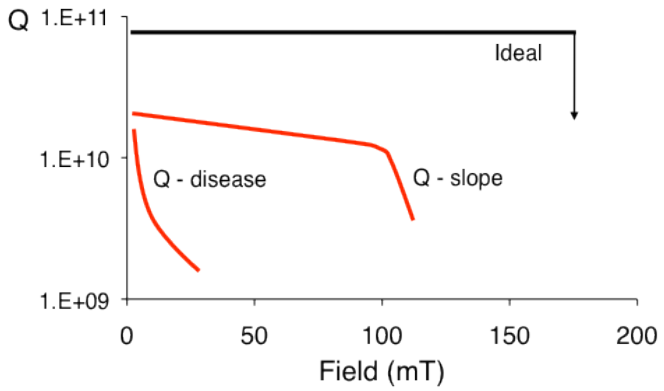

Figure 2.5. Schematic of cavity performance characterization curves exemplifying the impurity related limitations, Q-disease and Q-slope.

Above ~100 mT, Q-drop or high-field Q-slope typically plagues cavities. This phenomena has been characterized by experiments utilizing arrays of thermometers on the outside surface of a cavity, which demonstrate that as the field is increased, eventually local sources of dissipation arise and Q decreases [54]. The cause of the dissipation resulting in Q-drop is currently unknown; however, the condition is often mitigated by the low-temperature anneal. Consequently, the underlying mechanisms for this effect are also not well understood, although a number of models have been proposed [22]. Recent studies suggest connections to the oxygen and hydrogen concentrations and niobium vacancies. However, a single model that explains all these effects does not exist. The active elements are:

- **Oxygen –** Surface x-ray techniques [15-17] have demonstrated that a low-temperature anneal (120-160 °C) changes the composition of the surface niobium oxides from mostly Nb_2O_5 to lower oxides and enhanced concentrations of interstitial oxygen atoms. Measurements of oxygen diffusion in niobium yield a diffusion length of ~40-200 nm in 48 h in this temperature range [55]. Therefore, an oxygen diffusion model has been

proposed [56], which explains that during the low-temperature anneal, oxygen diffuses away from the niobium surface so that it can no longer affect cavity performance. Casalbuoni et al. [57], alternatively showed that low-temperature annealing increases the surface critical fields, consistent with the diffusion of oxygen into the near-surface region with a concomitant increase of electron scattering. Superconducting tunnel-junction measurements suggested a role is played by magnetic point defects, which could be created by vacant oxygen sites in the surface oxide [58, 59]. Experiments that compared cavity properties before and after baking could not, however, elucidate any direct role of oxygen contamination or changes in the surface oxide for the mitigation of Q-drop [22].

- **Hydrogen –** Visentin et al. [60] observed a correlation between positron annihilation – Doppler broadening parameters and a 145 °C anneal, which they attributed to release of hydrogen atoms from niobium vacancies. Romanenko [61] observed a reduction in the dislocation density after a 100-120 °C anneal, which he also attributed to the release of hydrogen from niobium vacancies resulting in an increased number of vacancies available to assist dislocation climb.

It has recently been suggested that hydride precipitates may be responsible for either Q-disease or Q-slope depending on the size of the precipitate [62]. While small niobium hydride precipitates embedded in the niobium should be weakly superconducting due to leakage of Cooper pairs from the niobium into the precipitate via the proximity effect [63]; they are nonetheless problematic under RF operating conditions because very strong currents, of order H_{RF}/λ, are induced next to the cavity wall. Here H_{RF} is the RF magnetic field amplitude. Strong

RF dissipation then occurs when the depairing current density for these coupled precipitates is exceeded [64]. For niobium the RF flux density, $\mu_0 H_{RF}$ can be >100 mT at the equatorial regions of SRF cavities. Hence, the surface currents decay with depth from ~2.5×10^{11} A m^{-2}.

Large precipitates gain little or no benefit from the proximity effect and produce dissipation at the onset of the RF magnetic field; therefore, they may be linked to Q-disease. The maximum size of a precipitate that can benefit from the proximity effect is determined by ξ in the precipitate. The hydride phases are metallic, so $\xi = (hv_F)/(2\pi k_B T)$, where h is Planck's constant, v_F is the Fermi velocity, and T is the temperature in degrees Kelvin. Assuming v_F is similar in niobium and the niobium hydride, and the cavities are operated at 2 K, an estimate for the lower limit for the diameter of problematic precipitates is ~ 0.5 μm.

CHAPTER 3. METHODS

Calculations Based on Density Functional Theory

Density functional theory is part of a class of simulation methods known as first principles, as it relies on quantum mechanics to predict the properties of a system of atoms. Density functional theory calculations have shed light on gas phase, solution phase, solid state, and interfacial systems [65, 66].

Quantum mechanical systems are described by the Shrödinger equation:

$$i\hbar \frac{\partial \Psi(\vec{r},t)}{\partial t} = \hat{H}\Psi(\vec{r},t)$$

where ħ is the reduced Planck's constant, $\hat{H}$ is the Hamiltonian operator, Ψ is the wave function, $\vec{r}$ is the vector distance between the particles, and t is time. For nonrelativistic systems

$$\hat{H} = -\frac{\hbar}{2m}\nabla^2 + V(\vec{r},t)$$

where the fist term on the right side of the equation is the kinetic energy, the second term is the potential energy, and m is the mass of the particle. The wave function is an unknown function which contains a complete description of the system. In chemical systems it includes terms for

each proton, neutron, electron, and interactions between them. This equation, however, is not analytically solvable or practically solvable even numerically for most systems. Several approximations can be often be made, though, which enable a practical solution. First, the time dependence can be separated from the spatial dependence to give the time-independent Schrödinger equation:

$$\hat{H}\Psi(\vec{r}) = E\Psi(\vec{r})$$

Second, the electrons move three orders of magnitude fasters than protons or neutrons, so the Born-Oppenheimer approximation can be applied, which allows one to separate the nuclear and electronic components. The electronic part of the Schrödinger equation is then solved, from which all ground state observables of a system can be extracted. The solution of the Schrödinger equation requires one to guess a form for the wave function, and iteratively solve the equation until a self-consistent solution is found.

Even once the above simplifications are made, most chemically and physically interesting systems involve many electrons, which makes the Schrödinger equation demanding to solve. Rather than solving a many-body Schrödinger equation, Hohenberg and Kohn [67] formulated a set of theorems, which state that the ground state electron density (ρ_0) determines the number of electrons in the system, the external potential, and the ground state energy (E_0). Kohn and Sham [68] then established that ρ_0 can be determined by solving a fictitious system of non-interacting electrons, each of which experience the same external potential. This potential causes the

fictitious system's ground state density, ρ_s, to equal ρ_0. Therefore, E_0 can be determined by minimizing the energy of the fictitious system, $E(\rho)$, so that $\rho=\rho_0$:

$$E(\rho)=T_s(\rho)+E^H(\rho)+V_{N\text{-}e}(\rho)+E_{xc}(\rho)=E_0$$

where $T_s(\rho)$ is the kinetic energy of the non-interacting system, $E^H(\rho)$ is the Hartree (electron-electron repulsion) energy, $V_{N\text{-}e}(\rho)$ is the nuclear-electronic interaction energy, and $E_{xc}(\rho)$ is the exchange-correlation energy. Although the formulation is exact, the form of $E_{xc}(\rho)$ is unknown. As the method continues to develop, new E_{ex} functionals are developed; however, all are parameterized.

Several classes of exchange-correlation functionals exist, each attempting to make an improvement over the limitations of the one created before it. The most basic class makes use of the local density approximation (LDA), which, as the name suggests, only accounts for the electron density at each specific point to calculate the energy at that point. The first improvement to this approximation additionally accounts for the gradient of the electron density at each point and is called the generalized gradient approximation (GGA). Further improvements include meta-GGA, which additionally accounts for second derivatives of the density; hyper-GGA, which includes 'exact exchange' calculated from the many-body Schrodinger equation; and hybrid functionals, which combine GGA and exact exchange with GGA or LDA correlation. Due to the computational demands of more advanced functionals and

the success of LDA and GGA at predicting many properties for many different systems, LDA and GGA functionals are still commonly used in chemistry and physics research. Furthermore, no single functional works well for all systems.

The ground state electron density is written as a function of the orbitals in the non-interacting system:

$$\rho = \sum_{i}^{N} \left| \phi_i^{KS}(\vec{r}) \right|^2$$

where ϕ_i^{KS} are the Kohn-Sham orbitals. For periodic systems, such as crystal structures, the Bloch theorem provides a mathematical description for the orbitals:

$$\phi_{\vec{k}}(\vec{r}) = u_{\vec{k}}(\vec{r}) \cdot e^{i\vec{k}\cdot\vec{r}}, \quad u_{\vec{k}}(\vec{r}) = u_{\vec{k}}(\vec{r} + \vec{T})$$

where $u_{\vec{k}}$ accounts for the periodicity, $\vec{k}$ is the wave vector, and $\vec{T}$ is the periodic length. The basis set is then formed by accounting for the reciprocal lattice vectors, $\vec{G}$, and the weight coefficients, c:

$$\phi_{i,\vec{k}}(\vec{r}) = \sum_{\vec{G}} c_{\vec{k}+\vec{G}} e^{i(\vec{k}+\vec{G})\vec{r}}$$

Only a finite sum is performed over certain special k-points in the Brilluoin zone describing the system and up to a specified kinetic energy cut-off, $(\hbar^2/2m)\left|\vec{k}+\vec{G}\right|^2$. The special k-points are selected according the system's symmetry and several schemes are available to select an efficient set. The accuracy of a calculation depends on the density of k-points and the energy cutoff that are used, so convergence tests must be performed for each new system in question.

Since electron density is larger near the core of an atom than at the valance, the wave functions oscillate rapidly in the core creating a large computational burden. These oscillations can be eliminated by using pseudopotentials to describe the cores rather than the plane wave basis set. For many systems, a good pseudopotential does not affect the prediction of chemical properties because only valance electrons participate in chemical bonding.

In addition to the application of density functional theory to solve the electronic structures of the model systems in this thesis, the system properties are determined as follows. The geometry optimizations employ the conjugate gradient method [69], which moves ions in the direction of the steepest decent of their calculated forces and stress tensor (predictor step) followed by a move to the where the anticipated energy minimum will be located (corrector step). A series of predictor-corrector steps are performed until sufficient accuracy is reached. Vibrational frequencies are calculated in the harmonic oscillator approximation from diagonalization of the Hessian matrix, which is a matrix of second derivatives of the energy with respect to position. Each atom is perturbed by 0.015 Å along each coordinate and the forces after each perturbation are calculated to create the matrix. Zero point energy (ZPE) is calculated from the formula E =

$0.5h\Sigma\nu_i$, and ν_i are the frequencies of the vibrational modes. Local properties, such as atomic charge and magnetic moment, are determined according to the Bader method [70-72], which searches for maxima and minima in the system's charge density distribution to assign the location and volume of each ion.

Experimental Tools

Raman and infrared spectroscopy are complimentary techniques based on molecular (or crystal) vibrations. Raman spectroscopy measures the inelastic scattered photons from a laser that is shined on a sample. A photon can be absorbed by a molecule, excite the molecule to a different energy level, and then be emitted at a different energy, Figure 3.1. The change in energy of the photons corresponds to the energy difference between the ground state and the excited vibrational mode of the molecule and is called the Raman shift. Stokes scattering occurs when the final energy of the molecule is higher than the initial energy and anti-Stokes scattering occurs when the final energy is lower than the initial; the intensity of Stokes scattering is typically much larger than anti-Stokes. The relative Raman intensity of one vibrational mode to other modes in the spectrum is directly proportional to the change in polarizability of the molecule during the vibration and the concentration of the species in the sample. IR spectroscopy detects the energies at which photons are absorbed by a molecule or crystal, which also corresponds to the energies of the vibrational modes. The IR intensity of a vibrational mode is dependent on the change in the dipole moment of the molecule during the vibration and the concentration of the species in the sample. Although some modes will be both Raman and IR active, molecules generally have a different fingerprint in Raman than IR spectroscopy.

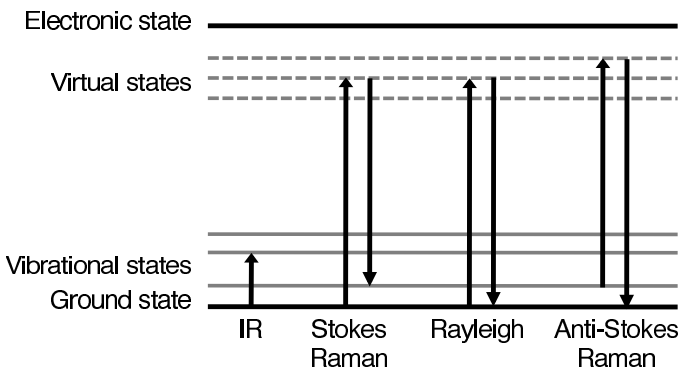

Figure 3.1. Schematic energy level diagram of some photon interactions with matter.

NMR spectroscopy is based on the nuclear spin of an atom. When a nucleus with a net spin is placed in a magnetic field, it will have two energy states: a low energy state where the magnetic field generated by the nuclear spin is aligned with the external magnetic field and a higher energy state where the two fields are opposed. Therefore, a nucleus has a characteristic resonance frequency, corresponding to the energy required to excite it to the higher energy spin state. The location of this frequency, or chemical shift, is dependent on the type of nucleus under consideration (e.g. ^{19}F) and the magnetic field strength. The local electronic environment around a nucleus partially shields it from the magnetic field, enabling different chemical shifts for the same type of nucleus located in different chemical environments (e.g. F in HF vs. $HFSO_3$). The intensity of the signal is proportional the concentration of the nuclei in the specific chemical environment.

CHAPTER 4. ELECTROPOLISHING SOLUTION ANALYSES

Abstract

In this section I discuss chemical analyses of the electropolishing solution. Vibrational and NMR spectroscopies were used to analyze the standard solution, and I show that fluorine is bound and released by the reaction of the acid components in the solution: $HF + H_2SO_4 <-> HFSO_3 + H_2O$. This result implies that new recipes can possibly be developed on the principle of controlled release of fluorine by a chemical reaction, which provides a route to improve the safety and effectiveness of electropolishing. I also show that NMR or Raman spectroscopy can be used to monitor the free fluorine when polishing with the standard electropolishing recipe.

Introduction

Although many studies have been performed by the SRF community to understand the effect of polishing parameters on SRF cavity performance [34, 40, 47, 57], as well as the mechanism and quality control of the process [38, 73-79]; the detailed chemistry remains elusive. Furthermore, simple inline process monitoring techniques are desired. In this study, vibrational and NMR spectroscopy were used to analyze the electropolishing solution.

Methods

A Renishaw, inVia, Raman microscope with a 785 nm diode laser and liquid sampling kit was used to obtain the Raman spectra at the Illinois Institute of Technology. The fluorescence backgrounds were subsequently removed by manually splining the spectra. A PerkinElmer

Spectrum One infrared spectrometer with a 633 nm laser and an attenuated total reflectance sampling probe was used to obtain the IR spectra at Fermilab, and drifting baselines were also subsequently corrected. Some of the Raman spectra were obtained during a PerkinElmer vendor visit at Fermilab. DFT based calculations of plausible species were performed to help identify unknown solution phase species and the results are given in Appendix 1.

The NMR spectra were measured on a 60 MHz NMR instrument at Anasazi Instruments, Inc. (www.aiinmr.com) operating at 56.4 MHz for ^{19}F. Five millimeter (5 mm) sample tubes were used with teflon inserts to avoid fluorine reaction with the borosilicate glass. No volume correction was applied to the teflon inserts, but the volume differences were determined to be less than 5%. A pulse-acquire program was used to acquire the spectrum with 8 scans. The repetition rate was 4 scans per minute to allow for complete relaxation of the ^{19}F species for a total measurement time of 2 minutes. Spectra were baseline flattened and integrated with fixed integrated regions using NUTS software (www.acornnmr.com). Chemical shifts are relative to $CFCl_3$ in acetone-d6 solvent.

Results

Raman Spectra

The spectra for freshly mixed electropolishing (EP) solution, 96% sulfuric acid, and 49% hydrofluoric acid are shown in Figure 4.1. Sulfuric acid has several strong peaks in its Raman spectrum while hydrofluoric acid doesn't appear to be distinguishable. Several new peaks (810

cm^{-1} and 1082 cm^{-1}) appear, however, in the EP solution spectrum that are not present in the sulfuric acid spectrum.

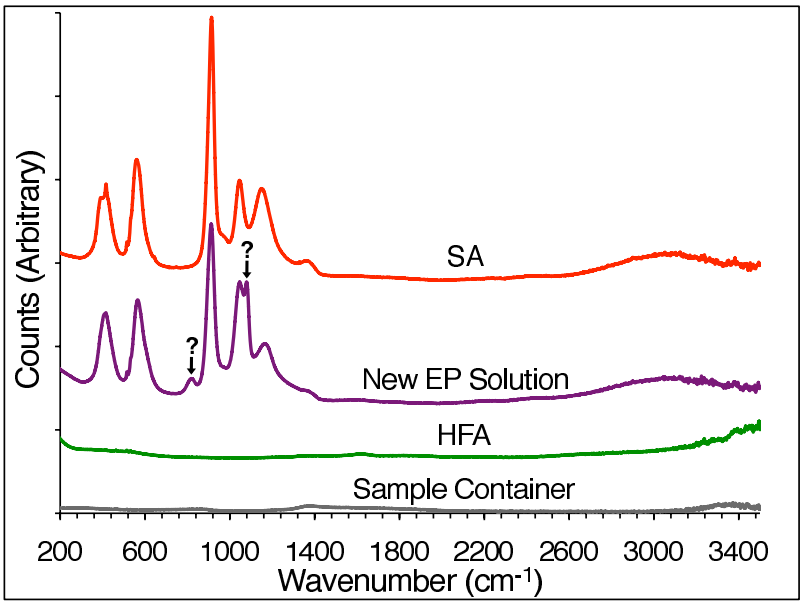

Figure 4.1. Raman spectra of new (unused) EP solution, its components (49 % hydrofluoric acid in water (HFA) and 96 % sulfuric acid (SA)), and the sample container. The spectra are plotted with an offset for clarity. The question marks/arrows indicate peaks in the new EP solution spectrum that cannot be explained by the separate component spectra.

Because sulfuric acid is a very strong acid, pK_{a1} = -3 in water, it is plausible that new peaks appear due to deprotonation upon the addition of the hydrofluoric acid solution. To test this hypothesis, the spectrum of sulfuric acid diluted with water was obtained, Figure 4.2. The relative intensities of the peaks in the sulfuric acid solution clearly change upon dilution, indicating differing concentrations of the ions comprising the sulfuric acid – water solutions at different concentrations. Namely, the loss of the peak at 1390 cm^{-1}, the change in the ratio between the ~915, 1050, and 1150 cm^{-1} peaks, and the growth of the peak at ~990 cm^{-1}. The peak locations and relative intensities for the new EP and sulfuric acid solutions are listed in

Table 4.1. These spectral changes do not explain the new peaks appearing upon the mixing of sulfuric and hydrofluoric acid, however.

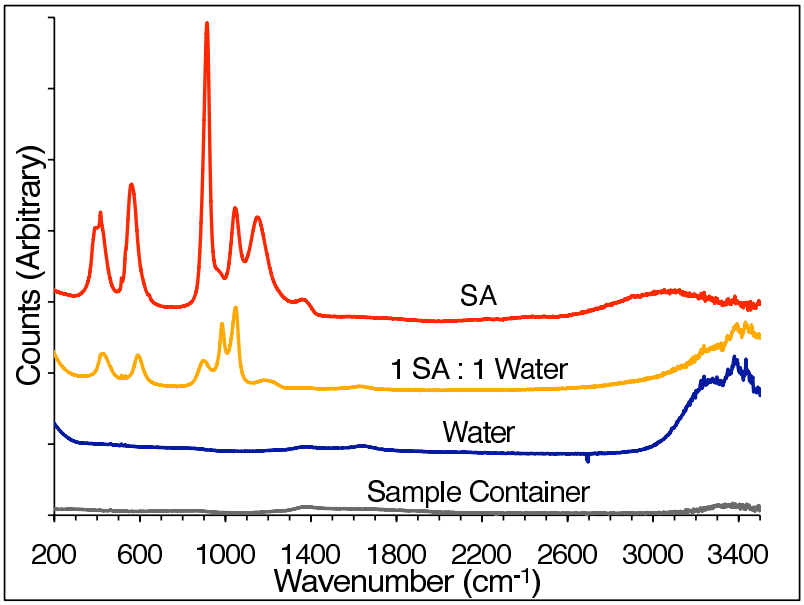

Figure 4.2. Raman spectra of 1 volume 96% sulfuric acid (SA) diluted with 1 volume water. The spectra of 96 % sulfuric acid (component of EP solution), water, and the sample container are shown for reference. The spectra are plotted with an offset for clarity.

Table 4.1. Raman peaks in the EP solution and sulfuric acid (SA) spectra.

New EP		1 vol. 96% SA : 0 vol. water		1 vol. 96% SA : 1 vol. water	
Location (cm^{-1})	Relative Intensity (%)	Location (cm^{-1})	Relative Intensity (%)	Location (cm^{-1})	Relative Intensity (%)
1390	4	1390	12	1210	18
1166	28	1150	38	1050	100
1082	65	1050	41	985	82
1053	68	990	20	910	40
915	100	915	100	600	47
810	8	570	49	435	48
565	65	415	40		
402	60				

The Raman spectrum of hydrofluoric acid was examined further for subtle features that may be useful for analysis. The spectra at several dilutions are shown in Figure 4.3. Hydrofluoric acid

is a very weak Raman scatterer [80]. Broad weak peaks appear around 1800 and 2200 cm^{-1} for the more concentrated hydrofluoric acid solutions, but they are clearly not suitable for tracking the fluorine concentration in dilute solutions.

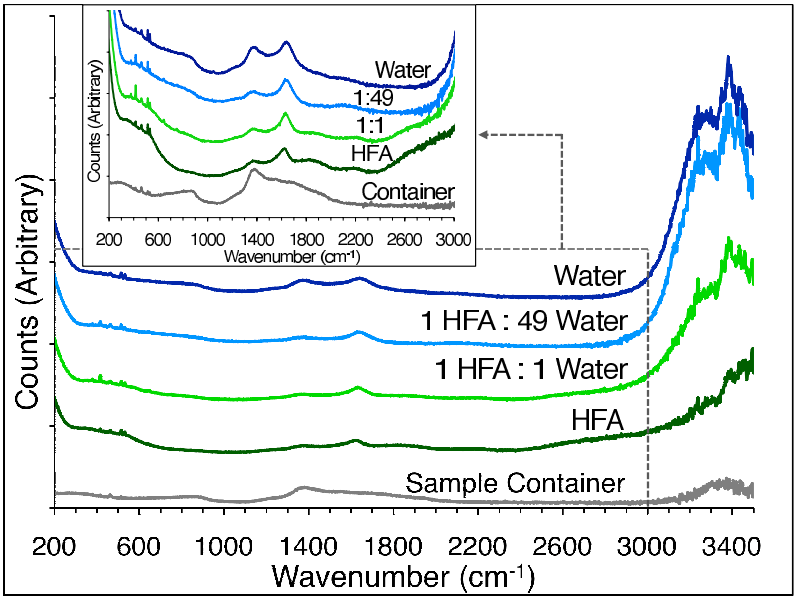

Figure 4.3. Raman spectra of 49 % hydrofluoric acid (HFA) diluted with water; the ratios are by volume. The spectra of 49 % hydrofluoric acid (component of EP solution), water, and the sample container are shown for reference. The spectra are plotted with an offset for clarity. The inset shows an expansion along the counts axis for the region 200-3000 cm^{-1}.

Based on the Raman spectra of Gillespie and Robison [81], a potential explanation of the new peaks in the EP solution is the production of fluorosulfonic acid from the reaction of sulfuric and hydrofluoric acids, R16.

The existence of fluorosulfonic acid in EP solution was previously determined by Eozenou, et al. [78], although they were not able to quantify it by their technique of ion chromatography.

The existence of fluorosulfonic acid in EP solution is confirmed by obtaining the spectra of EP solution with added fluorosulfonic acid and EP solution with added water, Figure 4.4. I was not able to obtain spectra of the concentrated fluorosulfonic acid due to safety and handling concerns. The spectrum of EP solution with added water is similar to the dilute sulfuric acid spectrum. Based on these spectra I attribute the peaks at 1082 and 810 cm^{-1} to fluorosulfonic acid. Based on the published spectra in [81] I assign the peak at 1082 cm^{-1} to the FSO_3^{-1} ion, since this peak appears in their spectrum of fluorosulfonic acid with 10% added water but not in their 100% fluorosulfonic acid spectrum. Fluorosulfonic acid can be deprotonated in EP solution since it is a stronger acid than both sulfuric and hydrofluoric acids, with a pK_a of 2.64 in sulfuric acid.

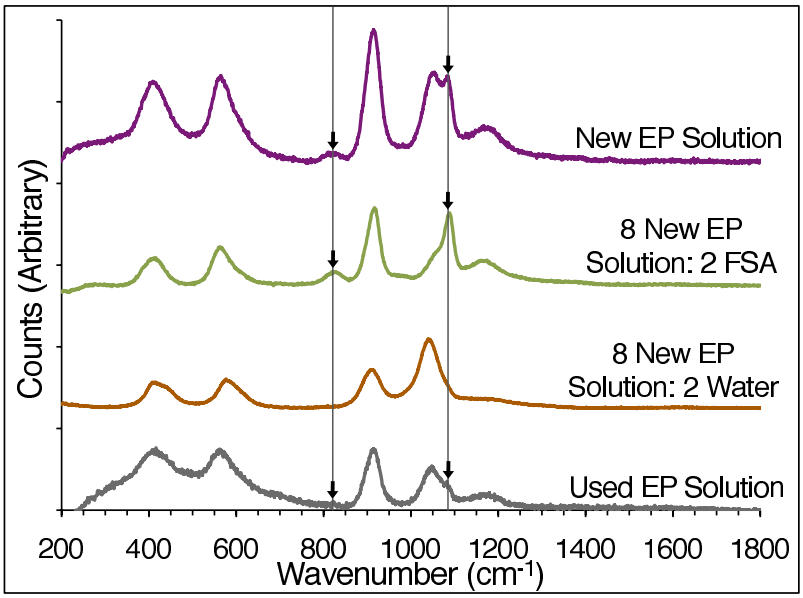

Figure 4.4. Raman spectra of new (unused) EP solution, 80 vol. % EP solution + 20 vol. % fluorosulfonic acid (FSA), 80 vol. % EP solution + 20 vol. % water, and used EP solution. The spectra are plotted with an offset for clarity. The arrows indicate peaks in the new and used EP solution spectra that are explained by the addition of fluorosulfonic acid.

The Raman spectrum of used EP solution is also shown in Figure 4.4. The used EP solution spectrum resembles the 96% sulfuric acid spectrum and the features representative of fluorosulfonic acid are reduced. This indicates that as free F^- is used during electropolishing, the fluorosulfonic acid that was produced upon the mixing of the solution components decomposes to produce more hydrofluoric acid, which is in turn used during the EP. Therefore, tracking the strongest fluorosulfonic acid peaks at 1082 and 810 cm^{-1} can be used as a method to track the amount of fluorine available for electropolishing.

Additional peaks are not evident in the used EP solution spectrum to indicate the formation of any electropolishing products. Based on the experiments of Keller [82] and von Barner et al. [83] niobium fluoride salts should have Raman and IR active vibrations in the 250-1100 cm^{-1} region. The peaks reported in [82] are listed in Table 4.2. Two possibilities exist for why these vibrations were not detected in this study: the concentration of the dissolved salts is too low or complexation with sulfuric acid reduces or eliminates their Raman activity.

Table 4.2. Raman and IR peaks of niobium-fluoride salts from [82].

K_2NbOF_5-H_2O (Raman)		$CsNbF_6$ (Raman)	
Location (cm^{-1})	Intensity	Location (cm^{-1})	Intensity
295	medium	280	medium
600	v. weak	562	weak
935	medium	683	strong
K_2NbOF_5-H_2O (IR, cm^{-1})		K_2NbF_7 (Raman)	
738	1626*	388	medium
932	3572*	630	v. strong
1083	3643*	782	weak

*from water of hydration

Infrared Spectra

The infrared spectra of the new EP solution, 96% sulfuric acid, and 49% hydrofluoric acid are shown in Figure 4.5, and their peak locations and relative intensities are listed in Table 4.3. Several differences exist between the Raman and infrared spectra; notably, hydrofluoric acid has IR active vibrational modes. These modes, however, still do not appear in the EP solution spectrum, as the feature at ~1650 cm^{-1} is from the water (Figure 4.6). As with Raman spectroscopy, peaks at 808 and 1076 cm^{-1} appear in the EP solution spectrum and can't be explained by the hydrofluoric acid dilutions (Figure 4.6) or the sulfuric acid dilutions (Figure 4.7): these peaks indicate the production of fluorosulfonic acid (Figure 4.8).

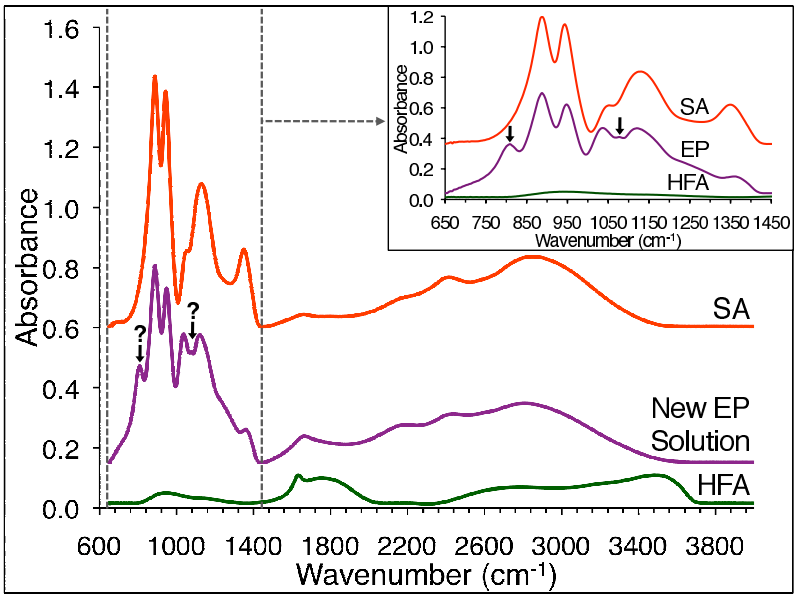

Figure 4.5. Infrared spectra of new (unused) EP solution and its components (49 % hydrofluoric acid (HFA) in water and 96 % sulfuric acid (SA)). The spectra are plotted with an offset for clarity. The inset shows an expansion of the region 650-1450 cm^{-1}. The question marks/arrows indicate peaks in the new EP solution spectrum that cannot be explained by the separate component spectra.

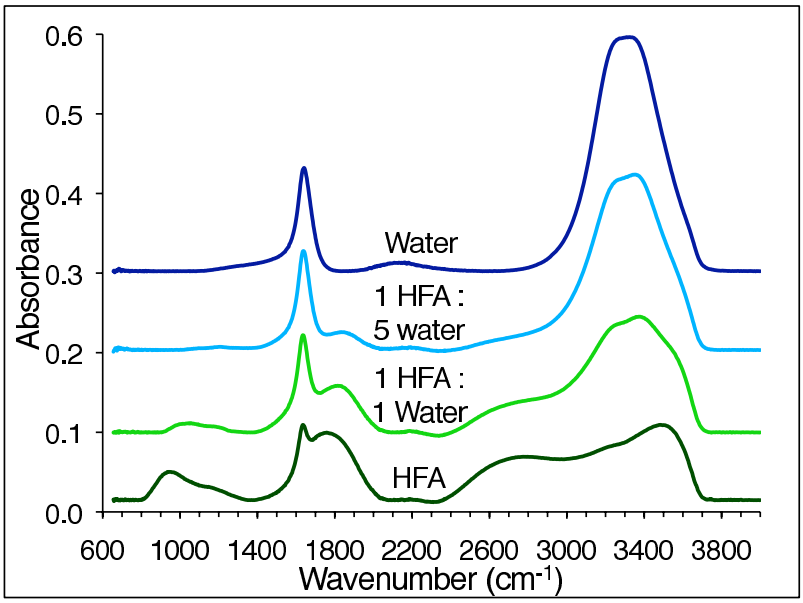

Figure 4.6. Infrared spectra of 49 % hydrofluoric acid (HFA) diluted with water; the ratios are by volume. The spectra of 49 % hydrofluoric acid (component of EP solution), and water are shown for reference. The spectra are plotted with an offset for clarity.

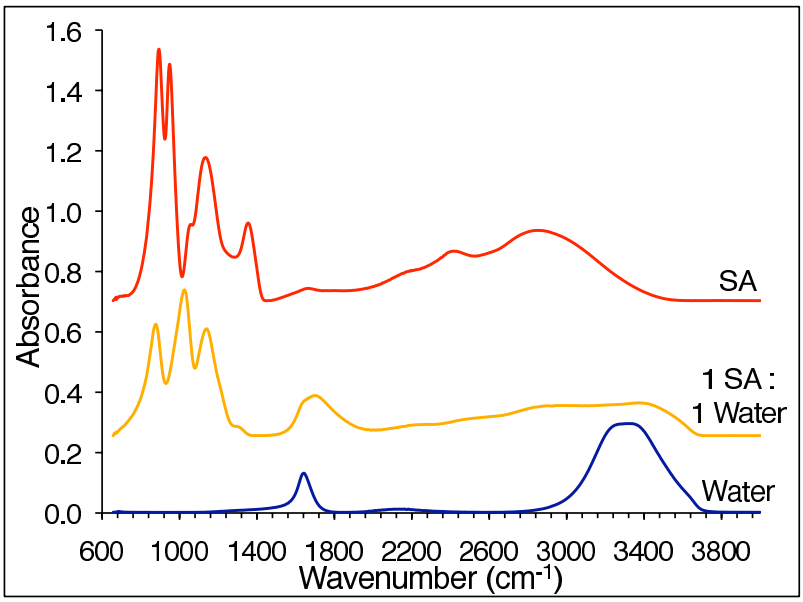

Figure 4.7. Infrared spectra of 1 volume 96% sulfuric acid (SA) diluted with 1 volume water. The spectra of 96 % sulfuric acid (component of EP solution) and water are shown for reference. The spectra are plotted with an offset for clarity.

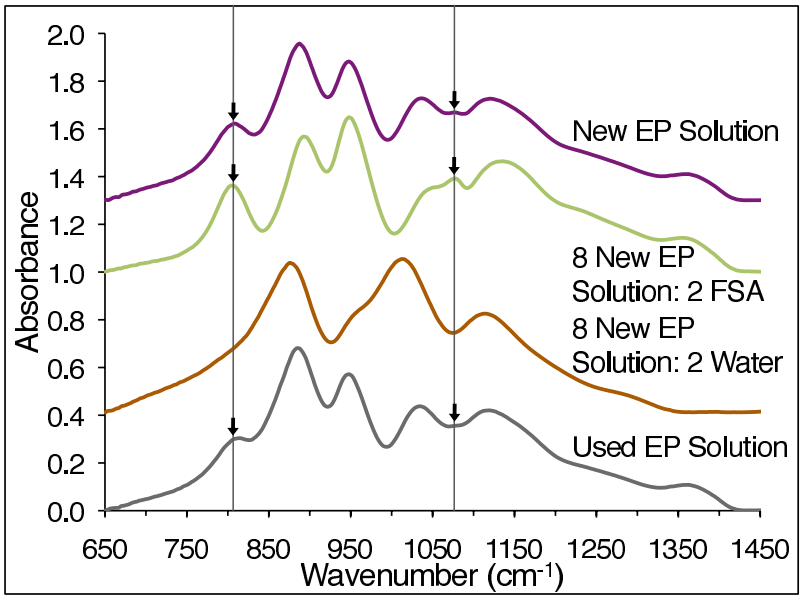

Figure 4.8. Infrared spectra of new (unused) EP solution, 80 vol. % EP solution + 20 vol. % fluorosulfonic acid (FSA), 80 vol. % EP solution + 20 vol. % water, and used EP solution. The spectra are plotted with an offset for clarity. The arrows indicate peaks in the new and used EP solution spectra that are explained by the addition of fluorosulfonic acid.

Table 4.3. IR peaks in new EP solution, sulfuric acid (SA), hydrofluoric acid (HFA), and water spectra.

New EP		1 vol. 96% SA : 0 vol. water		1 vol. 96% SA : 1 vol. water	
Location (cm^{-1})	Relative Absorbance (%)	Location (cm^{-1})	Relative Absorbance (%)	Location (cm^{-1})	Relative Absorbance (%)
2808	34	2849	28	3388	23
2437	29	2411	20	2893	21
2185	24	2162	12	2516	13
1660	18	1654	5	2210	9
1360	22	1348	31	1691	28
1120	67	1127	57	1291	8
1076	59	1053	31	1131	74
1036	67	941	94	1018	100
947	89	886	100	869	77
887	100	1 vol. 49% HFA : 0 vol. water		1 vol. 49 % HFA : 1 vol. water	
808	52	3484	100	3370	100
Water		~3284	~78	~3300	~95
3295	100	2779	63	~2783	~27
2114	7	2193	14	2179	1
1635	50	1755	91	1807	40
		1632	100	1630	84
		~1160	28	1175	5
		939	46	1026	8

The IR spectrum of used EP solution is also shown in Figure 4.8. The predominant fluorosulfonic acid feature (808 cm^{-1}) is reduced upon use of the EP solution, indicating that this peak can be tracked by IR to monitor the EP process. Again, no new peaks appear in the used EP spectrum to indicate electropolishing product formation.

NMR Spectra

The presence of fluorosulfonic acid in EP solution is also confirmed with ^{19}F NMR, and the spectra of new EP solution, new EP solution with added fluorosulfonic acid, and new EP solution with added water are shown in Figure 4.9. The NMR measurements allowed us to determine that new EP solution contains 1.61 mols of fluorine per kg of solution, of which 1.29

mols is bound in fluorosulfonic acid. Used EP solution, which contains ~ 2 g/l of dissolved niobium, also still contains 0.80 mols of fluorine bound in fluorosulfonic acid and only 0.01 mols of hydrofluoric acid per kg of solution. The used EP solution in this experiment does not represent completely exhausted solution. The peak near -170 ppm, which is representative of the fluorine associated with hydrofluoric acid downshifts a little in the new EP solution diluted with water. This is representative of the difference between the local chemical environment provided by each solvent as well as the differing relative concentrations of F^-, FHF^-, and HF in each solution [84, 85]. Although F^-, FHF^-, and HF each have a unique peak location, only one peak appears in hydrofluoric acid solutions due to rapid exchange between the ions, and the peak location indicates the relative concentrations of these ions. The peak location for various ratios of sulfuric acid/water/hydrofluoric acid is shown in Figure 4.10.

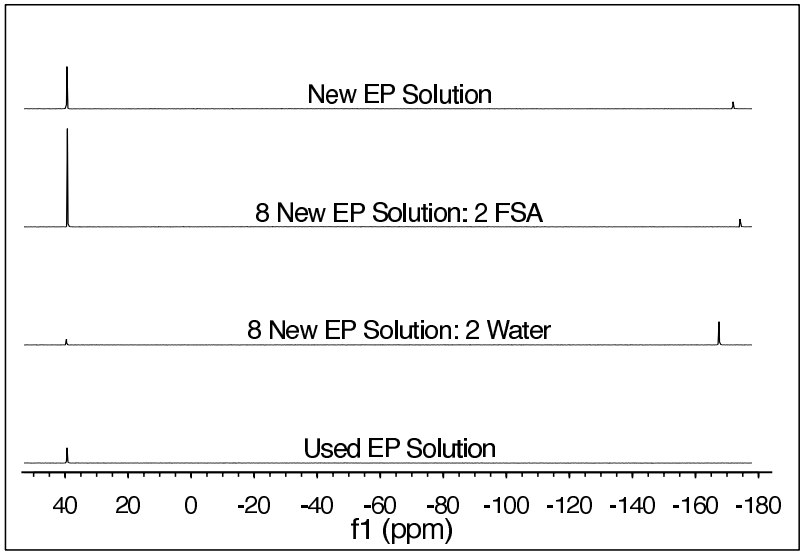

Figure 4.9. ^{19}F NMR spectra of new (unused) EP solution, 80 vol. % EP solution + 20 vol. % fluorosulfonic acid (FSA), 80 vol. % EP solution + 20 vol. % water, and used EP solution. The peak near 40 ppm indicates fluorosulfonic acid and the peak near -170 ppm indicates hydrofluoric acid.

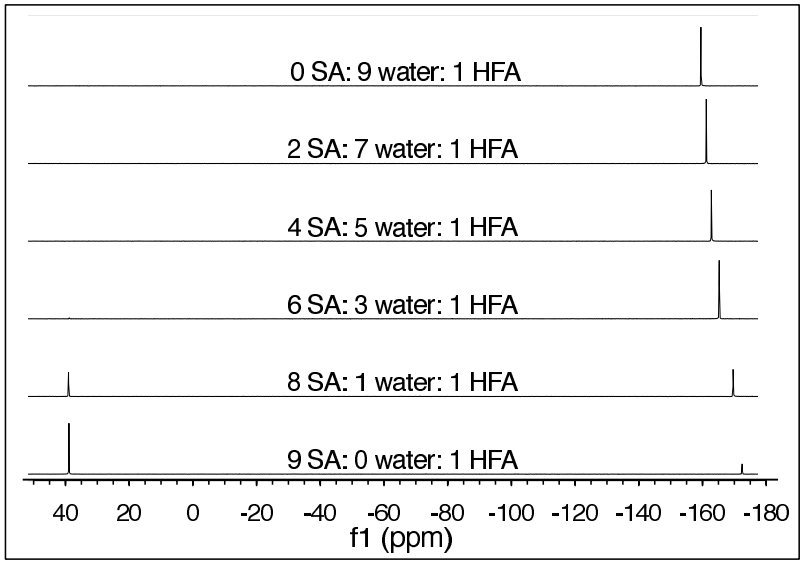

Figure 4.10. ^{19}F NMR spectra of 48 % hydrofluoric acid (HFA) diluted with various amounts of water and 95 % sulfuric acid (SA); the ratios are by volume. The peak near 40 ppm indicates fluorosulfonic acid and the peak near -170 ppm indicates hydrofluoric acid.

Discussion

The ratio of fluorine in hydrofluoric acid to fluorosulfonic acid, R = [HF]/[FSO_3^-], for various mixtures of hydrofluoric acid, sulfuric acid, fluorosulfonic acid, and water, and is presented in Table 4.4. I represent fluorosulfonic acid as the fluorosulfate ion, because fluorosulfonic acid is the strongest acid of the component species in the mixtures and the signature vibration of this ion was present in the Raman and IR spectra of new EP solution. Since hydrofluoric acid is a weaker acid, I represent it as HF, although its NMR signature contains contributions from HF, FHF^-, and F^-. I did not actually determine the ionization extent of either acid, and only intend to represent the balance between the fluorine related to each acid with R. For new EP solution, R is 0.25, so initially there is a small amount of fluorine available for dissolving the niobium, and as it is used (R16) runs in reverse, slowly supplying more fluorine. The equilibrium for this reaction has previously been briefly discussed in terms of niobium electropolishing by Saito et

al. [40], who suggested adding fluorosulfonic acid and water to used EP solution to refresh it. The NMR results presented in Table 4.4 show that water can simply be added to the EP solution to force the remaining fluorosulfonic acid to supply additional fluorine.

Table 4.4. The fluorine distribution in mixtures of 96 % sulfuric acid (SA), 49 % hydrofluoric acid (HFA), fluorosulfonic acid (FSA), and water determined from ^{19}F NMR measurements.

Initial Volume Ratios of Components in the Mixtures				$[HF]/[FSO_3^-]$
SA	HFA	FSA	Water	
0.900	0.100	0.000	0.000	0.25
0.891	0.099	0.010	0.000	0.24
0.855	0.095	0.050	0.000	0.21
0.720	0.080	0.200	0.000	0.11
0.720	0.080	0.000	0.200	6.26

Via conductivity measurements, Gillespie et al. [86] determined that the equilibrium constant for (R16) decreases with increasing temperature. Increasing the temperature also decreases the viscosity of the solution, therefore the free fluorine available for polishing is increased, and subsequently the etch rate, by two mechanisms. The addition of water also increases the amount of fluorine available for etching by the same two mechanisms. The NMR data presented in Table 4.4 show that increasing the amount of water in the solution increases the R, and the viscosities of sulfuric acid and water are 23 cp and 0.9 cp, respectively, at 25 °C [87]. Therefore, the etch rate would increase.

Not only do these results add to the knowledge of the chemistry of electropolishing, they also suggest that electropolishing could be controlled by a chemical component that binds the fluorine and slowly releases it. Thus we are provided with a route to explore potential new recipes for

niobium electropolishing with fluorinated components that are safer to handle and more effective than concentrated hydrofluoric acid.

Finally, I showed that the amount of fluorine available for polishing from the standard EP solution recipe can be tracked by NMR or Raman (or possibly very roughly by IR) spectroscopy. Raman spectroscopy is more suitable than IR because the differences between new and used EP solution are more striking than they are in IR and there are two fluorosulfonic acid peaks available for calibration, whereas there is only one suitable peak available in the IR spectrum. NMR provides two suitable signals in the ^{19}F spectrum for tracking.

CHAPTER 5. NIOBIUM HYDRIDE PHASE FORMATION

Abstract

In this chapter, I connect the fundamental properties of hydrogen in niobium to SRF cavity performance and processing. I modeled several of the niobium hydride phases relevant to SRF cavities and present their thermodynamic, electronic, and geometric properties determined from density functional theory based calculations. I find that hydrogen absorbs exothermically into niobium from the gas phase and becomes partially anionic. The absorption of hydrogen by niobium lattice vacancies is strongly preferred over absorption into interstitial sites. A single vacancy can accommodate six hydrogen atoms in the symmetrically equivalent lowest-energy sites and additional hydrogen in the nearby interstitial sites affected by the strain field: this indicates that a vacancy can serve as a nucleation center for hydride phase formation. Small hydride precipitates may then occur near lattice vacancies upon cooling. I also explain the phase changes in the niobium hydrogen system based on the charge transfer between niobium and hydrogen, the strain field inside of the niobium, and the geometry of the phases. The results of this study stress the importance of not only the hydrogen content in niobium, but also the recovery state of niobium for the performance of SRF cavities.

Introduction

The current forming and processing procedures for niobium SRF cavities afford many opportunities for hydrogen to be absorbed. The binding of hydrogen to niobium lattice defects and grain boundaries, moreover, serves as a potential reservoir of hydrogen; and in

polycrystalline sheets that have undergone various cold-working steps, the numerous dislocations and grain boundaries created permit hydrogen to access the bulk interior, despite the existence of a native oxide coating. It is not surprising, therefore, that hydrogen concentrations can be substantial in the near-surface region, to ~100 nm deep, which is relevant to cavity performance.

In this chapter, I present discuss models of the α, α', β, and ε phases of the niobium-hydrogen system, in which I determined the phase properties from density functional theory based calculations. I assess the roles of interstitial sites and Nb lattice vacancies for sequestering hydrogen, and discuss the nucleation of precipitates. I also examine the role of lattice strain, which may provide low energy pathways for hydrogen migration to newly-formed precipitates.

Methods

All calculations were performed utilizing the Vienna Ab-initio Simulation Package (VASP) [88, 89], using DFT, periodic boundary conditions, and a plane wave basis set with a 400 eV kinetic energy cutoff. The GGA-PBE exchange-correlation functional [90] was used, and the core electrons were described by the projector-augmented-wave (PAW) pseudopotentials [91, 92]. All of the structure optimizations were calculated with all of the atom and cell degrees of freedom relaxed. Forces were converged to 0.02 eV/Å. The geometry was optimized for each crystal structure with a 0.25 $Å^{-1}$ gamma-centered Monkhorst-Pack [93] k-point mesh. The partial occupancies for the wave functions were set by the 1st order Methfessel-Paxton method with a smearing width of 0.2 eV.

The interactions between interstitial hydrogen atoms and the niobium lattice were assessed in 4x4x4 unit cells (128 atoms) of bcc niobium. This unit cell was chosen to be computationally efficient while minimizing interactions between the periodic images. It is not intended to represent a specific concentration of defects. The calculated lattice constant in the absence of impurity atoms is 3.32 Å, which is in good agreement with the experimental lattice constant of 3.30 Å [94]. Tetrahedral and octahedral interstices were considered for impurity absorption. This unit cell was also used to assess the interactions between hydrogen atoms and a niobium lattice vacancy. The vacancy was created by removing one niobium atom, which corresponds to a vacancy concentration of ~0.8 at.%. The calculated vacancy formation energy is 2.71 eV, which is in good agreement with the experimentally determined range of 2.6-3.1 eV given in a review by Schultz and Ehrhart [95] and other first principles calculations [96, 97].

The niobium hydride structures were modeled as follows: β (NbH, 4 formula units per unit cell), and ε (Nb_4H_3 – NbH with one H atom removed from the unit cell containing 4Nb and 4H atoms). Both the cccm and cmma structures were considered for NbH and the formation of Nb_4H_3. The lowest energy structures resulted from the cccm NbH in both cases, and further analyses were only performed on these structures. The calculated lattice parameters for NbH are 3.50, 4.88, and 4.93 Å, which are within ~1% of the experimental values [98]. The α and α'- niobium hydride phases were modeled as bcc niobium (16 atoms per unit cell) with hydrogen atoms inserted into tetrahedral interstices. The properties for each concentration considered are reported as an average from two disordered configurations. An ordered configuration was also

considered for the $Nb_{16}H_{16}$ structure, which did exhibit some significantly different properties from the disordered structures, and is presented for comparison.

Several energetic properties are discussed in the results section for comparison between structures. Binding energies were calculated from various reference states, as were appropriate for the discussion, and these are specified in the results section. Negative (-) binding energies indicate that the bound state is lower in energy than the unbound state. Self-trapping energies were calculated as the difference between the impurity configuration optimized in a relaxed niobium lattice versus that optimized in a rigid niobium lattice. Strain energies were calculated as the difference in energy between the niobium lattice expanded by the impurity atom and the ideal bcc niobium lattice. ZPE is included in all energy calculations. The vibrational frequencies have been calculated for all of the atoms in the $Nb_{16}H_x$ unit cells. The change in ZPE is approximated for unit cells containing 127 or 128 niobium atoms as resulting only from the difference in vibrations of the impurity atoms. For example, the ZPE associated with the migration of H from an interstitial absorption site in bcc niobium to an absorption site in a niobium lattice vacancy was calculated as ZPE($Nb_{127}H$, H only relaxed) – ZPE($Nb_{128}H$, H only relaxed).

Results and Discussion

Dissolved Hydrogen in Body-Centered Cubic Niobium

Niobium absorbs hydrogen exothermically. The calculated absorption energy for hydrogen in tetrahedral sites is -0.28 eV relative to H_2 in the gas phase and pure bcc niobium, which is in

good agreement with previous DFT calculations [99, 100] and the experimental heat of solution [101, 102]. Hydrogen is found to be unstable in octahedral sites. Because niobium has a smaller Pauling electronegativity than hydrogen, 1.6 [103] and 2.2 [104], respectively, hydrogen becomes somewhat anionic when dissolved and expands the radius of a tetrahedral site from 0.52 Å to 0.59 Å. The lattice deformation causes 'self-trapping' of the hydrogen atom at strength of 0.18 eV. Hydrogen gains 0.65 e upon dissolution. The calculated absorption energy, charges, and lattice strain energies for the hydrogen are listed in Table 5.1 and the absorption geometry is depicted in Figure 5.1.

Table 5.1. Charges and energetics of hydrogen in bcc niobium tetrahedral interstices.

	$Nb_{128}H$
Charge on bonded Nb (e)	0.14
Charge on H (e)	-0.65
Absorption energy relative to $H_{2,gas}$ (eV)	-0.28
Lattice strain energy (eV)	0.11

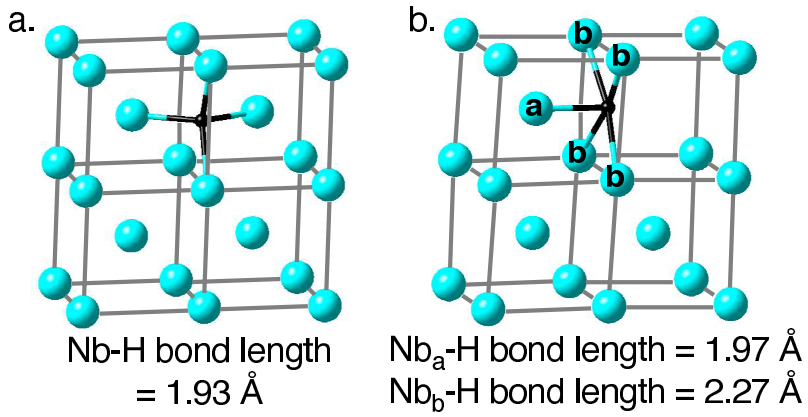

Figure 5.1. Geometry of hydrogen dissolved in a niobium tetrahedral interstice (a) and a niobium lattice vacancy (b). Small black spheres represent hydrogen atoms and large light-blue spheres represent niobium atoms.

Interaction Between Hydrogen and Niobium Lattice Vacancies

The charge distribution, absorption energy, and lattice strain energy caused by different amounts of hydrogen absorbed into a niobium lattice vacancy are given in Table 5.2. The absorption geometry of one hydrogen atom in a niobium lattice vacancy is displayed in Figure 5.1, and is similar to octahedral binding with one niobium atom missing. The addition of one hydrogen atom to a vacant niobium lattice site causes a reduction in the charge on the hydrogen by 0.09 e and change in bonding from four niobium atoms with a +0.14 e charge to four niobium atoms with a +0.13 e charge and one with a +0.11 e charge. As more hydrogen atoms are added to the vacancy, the charge on the hydrogen atoms is only slightly reduced; the charge, however, on the four niobium atoms with longer bonds to each hydrogen atom (type b, see Figure 5.1) continues to increase. The lowest energy configuration consists of six hydrogen atoms, each filling one of the six symmetrically equivalent octahedral-like binding sites in the vacancy. Furthermore, I found that hydrogen can continue to cluster around a vacancy after six hydrogen atoms have entered the vacancy at small energy gains (I attempted to add up to 6 additional hydrogen atoms), indicating that a niobium lattice vacancy can serve as a nucleation center for hydride phase formation.

Table 5.2. Charges on niobium atoms bound to hydrogen atoms and on the hydrogen atoms; absorption energies of hydrogen atoms in niobium lattice vacancies referred to the absorption energy of hydrogen atoms in tetrahedral interstitial sites; and lattice strain energies referred to the lattice strain energy of hydrogen atoms in tetrahedral interstitial sites. A vacancy binding site consists of one type a (charge given first in table) and four type b niobium atoms. See Figure 5.1 for the definition of type a and b niobium atoms.

	Nb_{128}	$Nb_{128}H$	Nb_{127}	$Nb_{127}H$	$Nb_{127}H_4$	$Nb_{127}H_6$
Charge on bonded Nb (e)	-0.01/0.01	0.14	0.08	0.11/0.13	0.08/0.26	0.11/0.32
Charge on H (e)	-	-0.65	-	-0.56	-0.53	-0.52
Absorption energy per H (eV)	-	0.00	-	-0.41	-0.39	-0.34
Lattice strain energy per H (eV)	-	0.00	-	-0.09	-0.09	-0.09

Hydrogen occupancy in metal vacancies has been the subject of prior studies (see the review by Pundt and Kirchheim [105], and references therein). Predictions of six deuterium atoms occupying a niobium lattice vacancy with a binding energy of -0.55 eV each has been advanced by Nordlander et al. [106] based on effective medium theory calculations, and six hydrogen atoms with a binding energy of -0.46 eV each by Koike et al. [107] based on temperature, pressure, and concentration dependent resistivity measurements. Čížek and coworkers [108, 109] have performed several studies on hydrogen in niobium vacancies using positron annihilation, showing the existence of vacancies containing up to four hydrogen atoms; however, based on calculations at several levels of theory, they predicted that the mean-positron life-time in a one-vacancy-six hydrogen cluster would be nearly the same as in the bulk niobium, so they would not be able to detect this arrangement. Both Čížek et al. and Koike et al. measured an increase in vacancy concentration with increasing hydrogen concentration, although the hydrogen-induced vacancy concentration remained three orders of magnitude smaller than the total hydrogen concentration, and was comparable to the expected thermally-induced vacancy formation near the melting point. Rao, et al. showed a similar result based on DFT and statistical modeling [100]. The addition of hydrogen to metals including niobium is believed to induce

vacancy formation, since several neighboring hydrogen atoms would be energetically stabilized by the presence of a vacancy [110, 111]. I find that the absorption energy of a single hydrogen atom into a vacancy is 0.41 eV greater than into a tetrahedral interstitial site. The total calculated absorption energy of six hydrogen atoms into a lattice vacancy from tetrahedral interstices is -2.05 eV, which would reduce the formation energy of a vacancy to ~0.66 eV.

Geometric and Electronic Aspects of Niobium-Hydride Phase Changes

Figure 5.2 shows the energy difference between isolated interstitial hydrogen atoms occupying tetrahedral sites in bcc niobium and the various niobium-hydride phases. These results highlight the thermodynamic favorability for the phase changes to occur at specific concentrations. The general shape of the solid-solution plot indicates that continual dissolution of hydrogen into niobium is favored with increasing hydrogen content up to a certain concentration at which the trend reverses. This behavior is common among transition metals and is related to a balance of the effects of metal lattice strain, hydrogen-metal attraction, and hydrogen-hydrogen repulsion [31]. A closer look at the plot reveals a distinct change in interaction energy at an atomic ratio of hydrogen to niobium (H/Nb) of 0.32. Prior to this point the energy decrease was mild with increasing hydrogen concentration, and afterwards the energy difference increases more quickly. This correlates with a change in the elastic modulus, which signals the phase change from the α to the α' phase. The addition of more hydrogen atoms continues to drive the energy decrease until an H/Nb ratio of 0.75 is reached, at which point the ordered fco phases ε and β become energetically favored. While a configuration of ordered hydrogen in the tetrahedral interstices of bcc niobium is plausible, this configuration is found to be higher in energy than that of fco β.

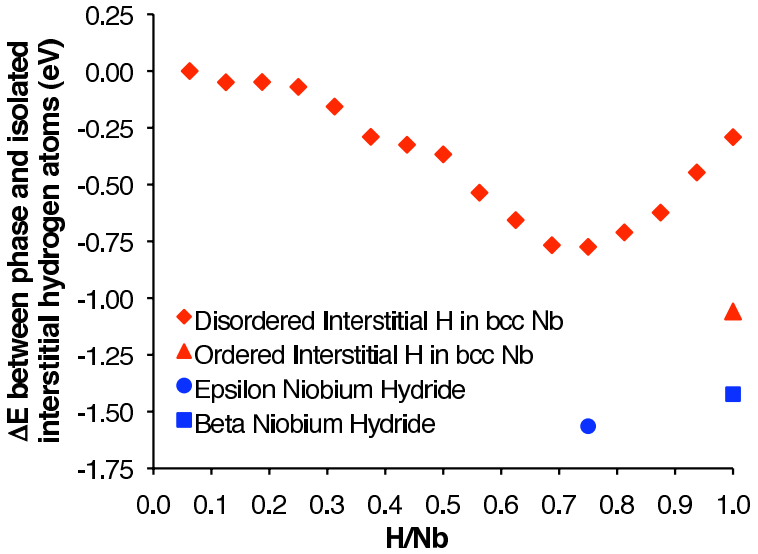

Figure 5.2. Energy difference between the niobium hydride phases and isolated hydrogen atoms in niobium tetrahedral interstices vs. hydrogen concentration.

The elastic deformation of the lattice with respect to hydrogen concentration in the solid-solution is shown in Figure 5.3. The results are in good agreement with the temperature-dependent X-ray diffraction data of Albrecht et al. [112] at 0.10 and 0.54 H/Nb ratio. Albrecht et al., however, measure a smaller expansion at 0.25 H/Nb, which is near the divide between the α and α' regions. The known slope of the lattice parameter increase (Δa/a) versus H/Nb plot (0.058 [113]) for the α phase is well-reproduced in this study (0.057). The deformation increases linearly in both solid-solution phases, but at a faster rate in the α than in the α' phase.

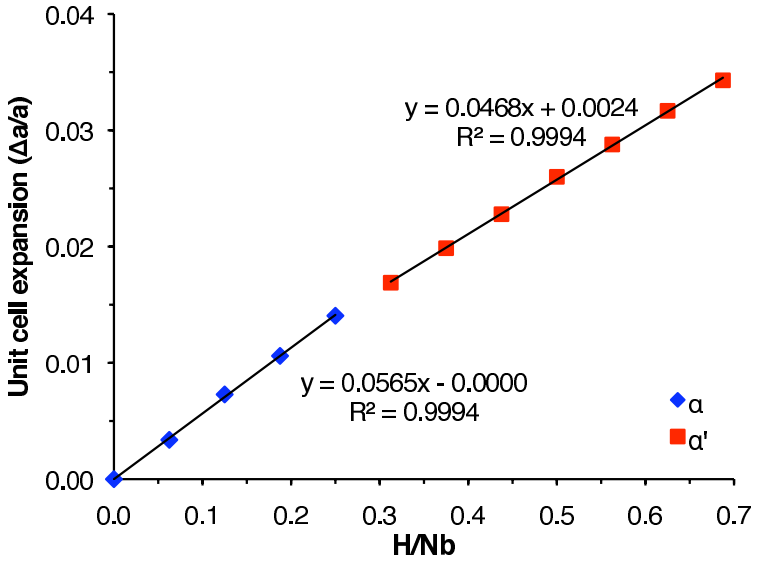

Figure 5.3. Unit cell expansion (a is the lattice parameter) vs. hydrogen concentration. Least squares fits to the data are also given. The α and α' phases are divided at ~20 at. %, based on the division in the experimental phase diagram.

The importance of charge distribution for phase formation was suggested by Aboud and Wilcox [99], who studied the electronic charge state of hydrogen in niobium, vanadium, tantalum, palladium and palladium-niobium alloys utilizing DFT and Bader charge analysis. They found an increase in hydrogen's electronic charge, the host metal's lattice parameter, and the absorption energy for hydrogen into vanadium and tantalum for an increase in hydrogen concentration from 0.0625 to 0.125 H/host atomic ratio; however, the electronic charge on hydrogen decreased when the hydrogen concentration was further increased to 0.25 H/host ratio. The reduction in hydrogen charge was accompanied by an increase in absorption energy and host lattice parameter. When the concentration was increased to 0.5 H/host ratio, they calculated a higher H charge and smaller absorption energy. The transition to the β phase for vanadium and tantalum occurs at 0.5 H/host ratio. They explained their observations as competition between

short-range repulsion between the dissolved hydrogen atoms and the attractive interaction between the hydrogen and host metal. Once short-range repulsion overtakes the attractive interaction a phase change will occur from solid solution to β phase. They also suggested that minimizing the hydrogen charged is favored, but the data were not definitive. For niobium, they found the increase in hydrogen concentration caused an increase in hydrogen's electronic charge, niobium's lattice parameter, and the energy of absorption of hydrogen into niobium for all of the concentrations that they studied; however, they did not include results past the pure β phase onset at H/Nb ratio ~0.7.

I performed a Bader analysis on representative concentrations of hydrogen in niobium for the α, α', ε, and β phases, and present the results in Table 5.3. The electronic charge on the hydrogen atoms, absorption energy, and self-trapping energy are all approximately the same for the two concentrations that represent the α phase, however the charge on the bonded niobium atoms varies within each configuration for H/Nb atomic ratios greater than 0.0625. The absorption and self-trapping energies both increase in the α' phase, and the electronic charge on the hydrogen atoms varies within each configuration at higher concentrations. The average value for the α' phase is -0.66 e. The average electronic charge on the hydrogen atoms slightly decreases for the 0.75 H/Nb (bcc) system to -0.65 e and further decreases to -0.64 e for 1.00 H/Nb (bcc).

Table 5.3. Charges on niobium atoms bound to hydrogen atoms and on the hydrogen atoms; absorption energies of hydrogen referred to bcc niobium and gas phase hydrogen molecules; and self-trapping and lattice strain energies caused by the absorption of hydrogen.

	$Nb_{16}H$	$Nb_{16}H_3$	$Nb_{16}H_8$	$Nb_{16}H_{12}$	$Nb_{16}H_{16}$	$Nb_{16}H_{16}$-o	Nb_4H_3-ε	NbH-β
Charge on bonded Nb (e)	0.13	0.07-0.32	0.12-0.57	0.36-0.69	0.50-0.75	0.64-0.71	0.52	0.70
Charge on H (e)	-0.66	-0.66	-0.63--0.69	-0.62--0.68	-0.56--0.68	-0.67	-0.67/-0.70	-0.70
Absorption energy per H (eV)	-0.24	-0.26	-0.29	-0.31	-0.26	-0.31	-0.37	-0.33
Self-trapping energy per H (eV)	-0.18	-0.18	-0.22	-0.25	-0.31	-0.27	-0.01	0.00
Strain energy per H (eV)	0.11	0.12	0.14	0.16	0.18	0.17	0.15	0.18

Consideration of the fco ε and β phases allows for a greater H charge than the bcc phases at the same concentrations, and the charges on the niobium atoms do not vary within the ε or β phases. The calculated lattice strain energies are also given in Table 5.3 and show that the strain is similar in the fco and bcc phases at the same hydrogen concentrations; therefore the transition to the fco phases occurs to maximize the electronic interaction between the niobium and hydrogen constituents. This assertion is confirmed by the fact that the NbH configuration with ordered hydrogen atoms in bcc niobium has a greater absorption energy and hydrogen charge than the configuration with disordered hydrogen atoms, but both of these properties are smaller in magnitude than they are for the fco (β phase) configuration. Additionally, the shortest Nb-H bond in the β phase is 1.94 Å, which is shorter than the shortest Nb-H bond in the ordered configuration of hydrogen in bcc niobium (1.95 Å). Hydrogen-hydrogen repulsion is also reduced in the β phase compared to the ordered configuration of hydrogen in bcc niobium, as the nearest neighbor H-H distances are 2.47 Å and 2.42 Å, respectively.

Application to Niobium Superconducting Radio-Frequency Cavities

The concentration and morphology of hydrogen in SRF cavities are affected by numerous steps in the SRF cavity forming and processing procedure. Beginning with the ingot, forging and rolling occur, which create vacancies and dislocations that can sequester hydrogen. After Nb sheets are rolled, they are annealed at 700-1000 °C to recrystallize the niobium and degas the dissolved hydrogen, but then the half-cells are plastically deep-drawn, which reintroduces lattice imperfections. The half-cells are then welded together, which creates a further damaged zone near the weld bead. The chemical or electrochemical polishing process that is applied to remove the surface layer that was damaged from forming provides a source of hydrogen, and also removes the protective oxide coating on the niobium, affording the possibility for hydrogen to be absorbed. This has been recognized [50] and therefore a high-temperature high vacuum anneal (800 °C for 2 hr or 650 °C for 10 hr), is employed to once again outgas the hydrogen. But are cavities hydrogen or hydride free at this point? Hydrogen gas is detected in and removed from the furnace during heat treatment; however, various recent experimental studies [19-22, 114] have shown that large hydrogen concentrations (10-50 at. %) are still present in the near-surface region.

Since niobium forms an oxide coating if exposed to air or water, the cavity immediately reforms an oxide surface layer once it is removed from the acid bath. However, the hydrogen that has already absorbed into the niobium is attracted to the near surface region due to the lattice strain field [27, 115-122]. In this chapter, I have explained the effect of the strain field in the niobium lattice on the relative stability of niobium-hydrogen complexes. The strain field also strongly

affects the diffusion of the hydrogen in niobium. Blomqvist, et al. [123] showed via ab initio molecular dynamics simulations that different activation energies characterize hydrogen diffusion in the regions 400–650 K, 650–1500 K, and at temperatures greater than 1500 K. They attributed this effect to a difference between the average Nb-H bond length in each temperature regime, which leads to unbinding to different degrees. At temperatures below room temperature the hydrogen plus binding-site pair and the strain field are considered to be fully coupled, and at temperatures below 244 K phonon-assisted tunneling dominates hydrogen diffusion [124]. The strain field also correlates with hydrogen concentration, as demonstrated by NMR [125] and Gorsky effect [126] studies, which display increasing activation energies for hydrogen diffusion in the α- and α'-phases with increasing hydrogen concentration. My calculations support these observations because I find an increase in strain energy with increasing concentration, and I also find an increase in the self-trapping energy per hydrogen atom. All of these observations imply that as the hydrogen concentration increases or temperature decreases, hydrogen's diffusivity decreases. Imperfections in the niobium lattice such as vacancies and dislocations, however, expand sites in the niobium lattice, thereby proving sites with lower energy barriers for hydrogen to hop between. This increases hydrogen's diffusivity and provides pathways for hydrogen atoms to find each other and form precipitated phases. Based on these assessments, two changes to the SRF cavity processing procedure might be considered: A cold acid polishing process, which might be self-arresting for hydrogen uptake, and annealing cavities prior to heavy chemical polishing, which will eliminate many of the defects that can enhance hydrogen uptake.

My results show that the trapping energy of hydrogen by lattice vacancies is significantly greater than the trapping energy of hydrogen by other dissolved hydrogen atoms, which suggests the favorability of heterogeneous nucleation of hydride phases over homogeneous nucleation. The relative binding strengths of hydrogen in niobium in the different situations examined in this study are depicted in Figure 5.4. Since the high-temperature anneal removes many of the dislocations and other imperfections introduced by metal forming, nucleation of large precipitates along extended defects should be rare. The reduction of nucleation centers for large precipitates may be an under-appreciated change that occurs during the high-temperature anneal and repair of Q disease. Only recently has the SRF community begun to consider the relief of lattice imperfections in cavity processing; so further studies, such as in situ measurements of hydride precipitate stoichiometry and size at different levels of recovery, could prove to be very useful.

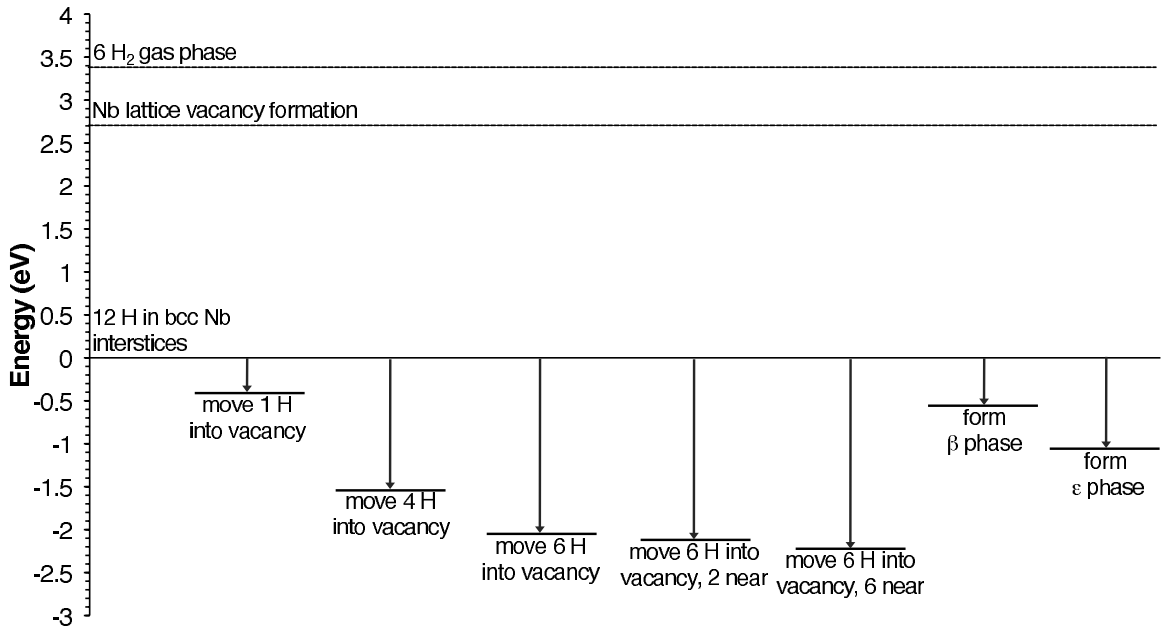

Figure 5.4. Energetic comparison of relevant configurations of hydrogen and niobium.

Finally, there are several reasons to eliminate the α' phase, even in the absence of heterogeneous nucleation centers. First, I have shown the favorability in terms of the electronic interaction for the α' phase to transform to the β or ε phase at high hydrogen concentrations. Second, Jisrawi et al. [28] demonstrated that T_c decreases with increasing hydrogen concentration in the solid-solution phases, so the performance of the SRF cavity could still be affected in the absence of ordered hydride phases.

Summary and Conclusions

I performed a density functional theory study of hydrogen in niobium, where I evaluated hydrogen in interstitial lattice sites, hydrogen in niobium lattice vacancies, and the formation of the α, α', ε, and β phases of niobium hydride. I discussed charge transfer from niobium to hydrogen (due to hydrogen becoming somewhat anionic in all cases), niobium lattice strain energy, and hydrogen-hydrogen repulsion as drivers for changes between phases. I compared homogenous to heterogeneous nucleation on lattice vacancies of ordered hydride phases. I found specifically:

- The absorption energy of hydrogen in niobium is -0.28 eV, and hydrogen gains 0.65 e upon absorption into a tetrahedral site. Hydrogen is not stable in octahedral sites in my model.
- A single vacancy in the bcc niobium crystal lattice is able to absorb significant amounts of hydrogen, being most stable for six hydrogen atoms, and the system energy continues

to decrease with additional hydrogen atoms absorbing near the vacancy. Thus single lattice vacancies can serve as nucleation centers for hydride phases.

- Phase changes from disordered hydrogen in body-centered cubic niobium to ordered hydrogen in face-centered orthorhombic niobium occur to maximize the charge transfer from niobium to hydrogen and to minimize the repulsion between hydrogen atoms.
- Self-trapping energies increase with increasing hydrogen concentration, indicating that hydrogen diffusion is hindered with increasing hydrogen concentration.

The results were discussed in terms of the processing of niobium superconducting radio-frequency cavities. The tendencies to cluster hydrogen near niobium lattice vacancies (and, by extension, clusters of vacancies and extended lattice defects) drive the formation of hydride precipitates upon cooling a cavity in preparation for superconducting operation. Hydride precipitates can then disrupt the flow of RF currents and possibly result in the reduction of cavity quality factor. The importance of removing both hydrogen and hydride phase nucleation centers from the cavities to prevent Q-disease and Q-drop was stressed, and in situ experimental studies of precipitate size and structure at various stages of recovery were advised. Finally, I recommend consideration of two changes to the cavity processing procedure: using cold acid for chemical polishing and annealing the cavities prior to chemical treatment.

CHAPTER 6. SUPPRESSION OF HYDRIDE PRECIPITATES

Abstract

This study provides guidance for cavity processing based on density functional theory calculations of the properties of common processing impurity species – hydrogen, oxygen, nitrogen, and carbon – in the bcc niobium lattice. I demonstrate that some fundamental properties are shared between the impurity atoms, such as anionic character in niobium; however, the strain field produced by hydrogen atoms is both geometrically different and substantially weaker than the strain field produced by the other impurities. The focus of this study is on the interaction between oxygen and hydrogen atoms in the lattice, and I demonstrate that the elastic interactions between these species and the bcc niobium lattice cause trapping of hydrogen and oxygen atoms by bcc niobium lattice vacancies. I also show that the attraction of oxygen to a lattice vacancy is substantially stronger than the attraction of hydrogen to the vacancy. Additionally hydrogen dissolved in niobium tetrahedral interstitial sites can be trapped by oxygen, nitrogen, and possibly carbon atoms dissolved in octahedral interstitial sites. These results indicate that the concentration of oxygen, and possibly also the other atomic impurities, in the bcc lattice can have a strong impact on the ability of hydrogen to form detrimental phases. Based on these results and a literature survey, a mechanism is proposed for the success of the low-temperature annealing step applied to niobium SRF cavities. I also recommend further examination of nitrogen and carbon in bcc niobium, and particularly the role that nitrogen can play in preventing detrimental hydride phase formation.

Introduction

Many SRF cavities are operated immediately following the high-temperature anneal because only a small decrease of Q is observed with increasing RF field, often remaining above 10^{10} at surface RF magnetic fields up to ~100 mT. At this point, Q-slope often occurs, which may be related to the hydrogen, oxygen, and defect concentrations and structures. The presence of oxygen, nitrogen, and carbon, may be beneficial to SRF cavity performance at low concentrations, however. The SRF community has observed that Q-disease usually does not occur in cavities made with lower purity reactor grade niobium [52], which has a carbon and nitrogen specification of < 0.01 wt. % and O specification of < 0.015 wt. %. High purity niobium, which is susceptible to Q-disease, typically has an oxygen, nitrogen, and carbon concentrations < 10 wt. ppm [52].

Hydrogen is present in the top 50 nm of the cavity subsurface region at greater concentrations than the equilibrium solubility after the high-temperature anneal, as demonstrated by recoil spectroscopy measurements [19, 20], atom-probe tomography measurements [18], nuclear reaction analyses [21], and secondary ion mass spectrometry [22]. This may be a result of hydrogen absorption during the light chemical polishing (removal of 20 μm) of the surface that is typically performed after the high-temperature anneal [23]. This hydrogen can then become trapped inside of the cavity because the oxide layer hinders the transport of hydrogen in or out of the niobium [24]. The enhanced concentration of hydrogen in the subsurface region may be due to trapping of dissolved hydrogen atoms by niobium lattice imperfections – such as vacancies, dislocations, or grain boundaries – other dissolved impurity atoms such as the oxygen provided

by the oxide coating, or the interface between the oxide and niobium [25-27].

Motivated by these issues, I performed a density functional theory based study of hydrogen and oxygen atoms in niobium. I calculated the electronic and geometric properties of the impurity atoms dissolved in the interstices of the bcc niobium lattice as well as near niobium lattice vacancies. I also touched upon the properties of nitrogen and carbon in niobium. I then discuss the results in terms of the formation of niobium hydride precipitates, and explain their implications for SRF cavity processing.

Methods

All calculations were performed with utilizing DFT in VASP [88, 89]. The properties of the interstitial impurities H, O, N, and C in bcc niobium were assessed in 4x4x4 unit cells (128 atoms), and the selected calculation parameters are the same as what was used for the 128 Nb atom unit cell in Chapter 5. Tetrahedral and octahedral interstices were considered as absorption sites for these impurity species. This unit cell was also used to assess the interactions between hydrogen and oxygen atoms, and a niobium lattice vacancy.

Several energetic properties are discussed in the results section for comparison between structures. Binding energies were calculated from various reference states as were appropriate for the discussion, and these are specified in the results section. Negative (-) binding energies indicate that the bound state is lower in energy than the unbound state. Strain energies were calculated as the difference in energy between the niobium lattice expanded by the impurity atom

and the ideal bcc niobium lattice. ZPE is included in all of the energy calculations unless otherwise noted. The contribution is approximated as resulting only from the difference in vibrations of the impurity atoms. For example, the ZPE associated with the migration of H from an interstitial absorption site in bcc niobium to an absorption site in a niobium lattice vacancy was calculated as ZPE($Nb_{127}H$, H only relaxed) – ZPE($Nb_{128}H$, H only relaxed).

Results and Discussion

Interstitial Hydrogen, Oxygen, Nitrogen, and Carbon Atoms

Dissolved oxygen, nitrogen, and carbon all occupy octahedral lattice interstitial sites. The charge acquired by these interstitial impurity atoms when absorbed into bcc niobium is 2-3 times greater than the charge acquired by interstitial hydrogen atoms; and their binding energies, referred to the impurity atoms in the gas phase, is about 2.5-3.5 times greater than that of hydrogen (Table 6.1). The atomic radii of these impurity atoms and their bond lengths are given in Table 6.2, which shows that the diameters of O, N, and C are at least 0.78 Å larger than the shortest distance between niobium atoms surrounding an octahedral site, and at least 0.40 Å smaller than the longest distance between niobium atoms surrounding an octahedral site. Thus, an anisotropic lattice deformation consisting of an increase in the short distance between niobium atoms and a decrease in the long distance between niobium atoms surrounding an octahedral site occurs when an octahedral site absorbs an oxygen, nitrogen or carbon atom. I have already shown in Chapter 5 that hydrogen occupies tetrahedral lattice interstitial sites in bcc niobium, and its atomic radius is comparable to the size of a tetrahedral site; thus a much smaller lattice deformation occurs upon the absorption of hydrogen into the niobium lattice interstices. Additionally, all four of the

bonded niobium atoms are pushed outwards upon absorption of a hydrogen atom into the interstice. The geometries of tetrahedral and octahedral sites are depicted in Figure 6.1. Since interstitial oxygen is present in large and variable quantities in SRF niobium due to oxidation of the surface and contact with water, and the properties of nitrogen, carbon, and oxygen interstitials are similar, the effects of oxygen on hydrogen absorption and phase formation is the focus of the remainder of this study.

Table 6.1. Charges on the niobium atoms bonded to the interstitial impurity atoms – H, O, N and C – and on the interstitial impurities; binding energies of the interstitial impurities absorbed into a bcc niobium lattice interstitial site referred to bcc niobium and the impurity species as an atom in the gas phase; and the lattice strain energies caused by the impurity species residing in the interstice. H occupies tetrahedral binding sites; and O, N, and C occupy octahedral binding sites. The charge for Nb atoms with 'b' bonds to the impurity atoms is given first in the table and for Nb atoms with 'c' bonds is given second. See Figure 6.1 for an illustration of the binding geometries.

	Nb_{128}	$Nb_{128}H$	$Nb_{128}O$	$Nb_{128}N$	$Nb_{128}C$
Charge on bonded Nb (e)	-0.01/0.01	0.14	0.12/0.23	0.21/0.31	0.26/0.37
Charge on interstitial atom (e)	-	-0.65	-1.35	-1.63	-1.76
Binding energy (eV)	-	-2.41	-7.02	-7.39	-8.48
Lattice strain energy (eV)	-	0.11	0.83	0.83	0.96

Table 6.2. Nb-interstitial impurity bond lengths. Tetrahedral (tet.) sites provide four equidistant bonds, 'a' and octahedral (oct.) sites provide two *equidistant short bonds,* 'b', and four *equidistant long bonds*, 'c'. An n/a table entry means not applicable. The geometries are depicted in Figure 6.1.

	Impurity–Nb Bond Length (Å)			Atomic Radius
	A	b	c	(Å)[49]
Nb128 tet. site*	1.86	n/a	n/a	1.45 (Nb)
Nb128H	1.94	n/a	n/a	0.25 (H)
Nb128 oct. site*	n/a	1.66	2.35	1.45 (Nb)
Nb128O	n/a	2.04	2.30	0.60 (O)
Nb128N	n/a	2.05	2.24	0.65 (N)
Nb128C	n/a	2.08	2.24	0.70 (C)

* hypothetical bond lengths in the lattice sites that are not deformed by impurity absorption.

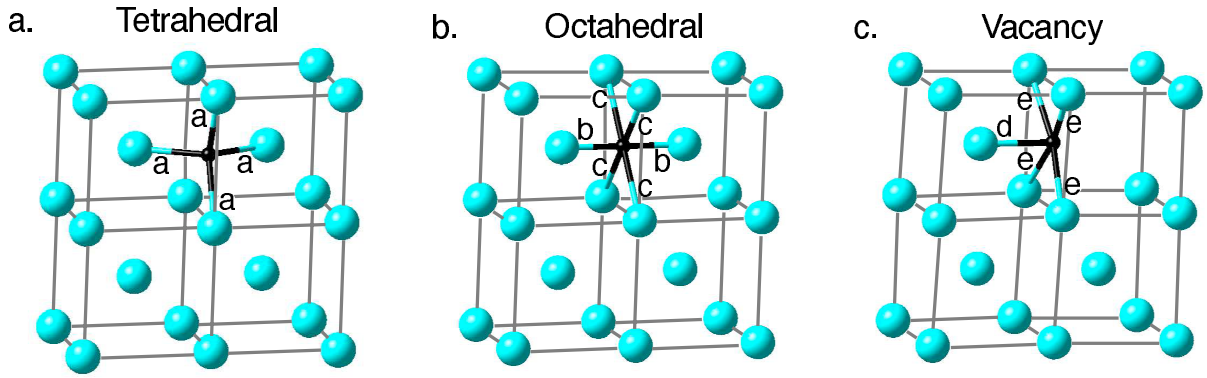

Figure 6.1. Illustration of (a) tetrahedral, (b) octahedral, and (c) vacancy binding sites in bcc niobium. A small black sphere represents an impurity atom and large light-blue spheres represent niobium atoms. The niobium-impurity atom bonds labeled 'a' are equidistant, niobium-impurity atom bonds labeled 'b' are equidistant, etc. The bond lengths are given in Tables 6.2 and 6.4.

Hydrogen Trapping by Other Interstitial Impurities

Dissolved hydrogen atoms can become trapped by several mechanisms, including other interstitially dissolved impurity atoms. Prior studies have demonstrated that a dissolved oxygen or nitrogen atom can bind one hydrogen atom in a nearby absorption site with a binding energy, referred to a hydrogen atom dissolved in a bcc niobium tetrahedral interstice infinitely far away from the trapping impurity, of approximately -0.1 eV [127-130]. The trapping effect has been explained by an expansion of the some of the nearby interstitial absorption sites resulting from the lattice deformation caused by the absorption of the other impurity atom into an octahedral site. The ideal trapping site is both close enough to the other impurity to benefit from the elastic expansion of the lattice, yet sufficiently far away to minimize the Coulomb repulsion between the two impurity atoms. Several theoretical [129, 131] and experimental [132-136] studies have been performed to identify the trapping configuration, but there still remains controversy.

Occupation of tetrahedral sites by trapped hydrogen atoms has been established by neutron spectroscopy [136], although the site is not equivalent to a tetrahedral site that is not in the vicinity of the trapping impurity. The non-equivalency has been demonstrated by ion channeling experiments with a nuclear reaction [135], where the authors propose occupation of displaced tetrahedral sites. Additionally x-ray scattering experiments [134] demonstrate a change in symmetry from cubic for free interstitial hydrogen to tetragonal for trapped hydrogen. I showed in the previous section that the bcc niobium lattice is distorted substantially in the neighborhood of an absorbed oxygen or nitrogen atom.

I determined the O-H trapping configuration by calculating the binding energy for a hydrogen atom in absorption sites up to 8.5 Å away from an oxygen atom in an octahedral site. All of my initial configurations included hydrogen atoms in tetrahedral sites; however, the coordinates of all of the atoms were relaxed during the geometry optimization calculations, so the hydrogen atom would have been free to move into nearby octahedral, trigonal, etc. sites. I find that the only significantly favorable (binding energy of -0.06 eV) site is a tetrahedral site in-plane with the four long Nb-O bonds; this site provides one bond to one of these niobium atoms and three bonds to niobium atoms that are not bonded to the oxygen atom, Figure 6.2. The configuration represents a 6th nearest-neighbor pair with an O-H distance of 4.11 Å. The bond lengths between the four niobium atoms and the hydrogen atom are not exactly equivalent in my suggested configuration, with the hydrogen atom being displaced slightly toward the oxygen atom. The differences in the Nb-H bond lengths are ~0.04 Å. In agreement with [136], I only find small differences in the energies of hydrogen's three vibrational modes (two occur at the same energy)

between the trapped and free states: -2 and 7 meV. I also find only small differences in charges between the trapped and free states: +0.02 e on the oxygen atom and -0.02 e on the hydrogen atom.

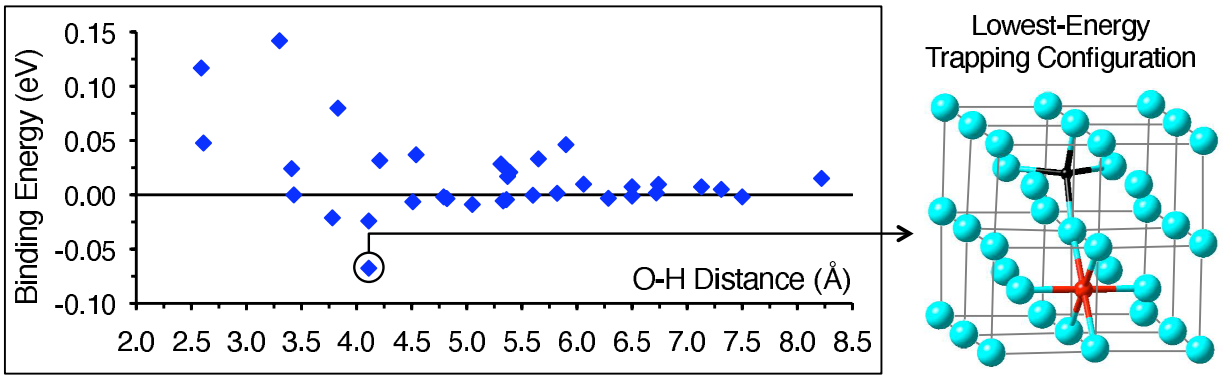

Figure 6.2. Plot of binding energy, referred to a hydrogen atom in a bcc niobium tetrahedral interstice and an oxygen atom in an infinitely far away octahedral interstice, versus the distance between an oxygen atom in an octahedral interstice and a trapped hydrogen atom in a nearby tetrahedral interstice. The highest-energy configuration is not shown on the plot because it is substantially higher in energy than all of the other configurations; its coordinates are (2.17, 0.36). ZPE was neglected in these binding energy calculations, but the contribution was checked for the lowest-energy configuration and found to be ~0.005 eV. A diagram of the lowest-energy configuration is also shown. Niobium atoms are represented by large light-blue spheres, the oxygen atom by a medium red sphere, and the hydrogen atom by a small black sphere.

I also calculated the trapping energy for the lowest-energy O-H trapping configuration while replacing the oxygen atom with a nitrogen atom, -0.10 eV. The similar but slightly larger binding energy for a nitrogen atom compared to an oxygen atom is in agreement with experiments [127, 128, 130], and consistent with my report of the lattice deformation being similar but larger in magnitude for a nitrogen atom compared to an oxygen atom (Table 6.2).

Finally, it may be possible for each oxygen or nitrogen atom to trap more than one hydrogen atom when a niobium specimen is cooled rapidly [137, 138]. The site occupied by a hydrogen

atom in my lowest-energy trapping configuration exists in eight symmetrically equivalent sites around the oxygen atom, and four of these sites are available for the simultaneous occupation of different hydrogen atoms. A kinetic study is, however, required to shed further light on the trapping of multiple hydrogen atoms by a single oxygen or nitrogen atom, which is outside of the scope of this study.

Hydrogen and Oxygen Trapping by Niobium Lattice Vacancies

The charge distribution, and binding and lattice strain energies (referred to the appropriate number of hydrogen atoms in bcc niobium tetrahedral interstices and oxygen atoms in octahedral interstices) caused by different numbers of hydrogen and oxygen atoms residing in a niobium lattice vacancy are listed in Table 6.3. Both hydrogen and oxygen occupy the same type of vacancy binding site, which is similar to an octahedral binding site, less one niobium atom that would form a short bond (Figure 6.1 and Table 6.4). I have already shown in Chapter 5 that six hydrogen atoms occupying the six symmetrically equivalent octahedral-like sites was the most stable configuration, and was strongly preferred to hydrogen atoms occupying the tetrahedral lattice interstices. In this chapter, I report that that the binding energy to a vacancy is twice as large for an oxygen atom as it is for a hydrogen atom, and a niobium lattice vacancy can bind a maximum of four oxygen atoms. The calculated binding energies of -0.79 eV for an oxygen atom and -0.41 eV for a hydrogen atom are in good agreement with values obtained from experiments [107, 139].

Table 6.3. Charges on niobium atoms bonded to an impurity atom and on the impurity atoms; and binding and lattice strain energies of the impurity atoms in niobium lattice interstitial sites and vacancies referred to the isolated impurity atoms located in their preferred interstitial sites. Where two table entries are present, the first one applies to a niobium atom in a type 'b' or 'd' bond and the second entry applies to a niobium atom in a type 'c' or 'e' bond. See Figure 6.1 for the definition of bond types.

	Nb_{128}	$Nb_{128}H$	Nb_{127}	$Nb_{127}H$	$Nb_{127}H_4$	$Nb_{127}H_6$
Charge on bonded Nb (e)	- 0.01/0.01	0.14	0.08	0.11/0.13	0.08/0.26	0.11/0.32
Charge on H (e)	-	-0.65	-	-0.56	-0.53	-0.52
Binding energy per H (eV)	-	0.00	-	-0.41	-0.39	-0.34
Lattice strain energy per H (eV)	-	0.00	-	-0.09	-0.09	-0.09
	Nb_{128}	$Nb_{128}O$	Nb_{127}	$Nb_{127}O$	$Nb_{127}O_4$	$Nb_{127}O_6$
Charge on bonded Nb (e)	- 0.01/0.01	0.12/0.23	0.08	0.09/0.29	0.20/0.54	0.22/0.74
Charge on O (e)	-	-1.35	-	-1.32	-1.28	-1.19
Binding energy per O (eV)	-	0.00	-	-0.79	-0.24	0.20
Lattice strain energy per O (eV)	-	0.00	-	-0.59	-0.43	-0.31

Table 6.4. Nb-impurity bond lengths when an impurity atom is located in a niobium lattice vacancy. The geometry is similar to the octahedral binding geometry, Figure 6.1, and consists of one *short bond,* 'd', and four *equidistant long bonds*, 'e'.

	Impurity – Nb Bond Length (Å)	
	d	e
Nb127H	1.97	2.27
Nb127O	2.14	2.19

A Bader analysis of the local charges shows that the addition of one oxygen atom to a vacancy causes only a 0.04 e decrease in the charge on an oxygen atom, and the bonding changes from four niobium atoms with a +0.23 e charge and two with a +0.12 e charge to four with a +0.29 e charge and one with a +0.09 e charge. Given the small change in the charge on an oxygen atom when residing in a vacancy, the decrease in binding energy can be attributed largely to the relaxation of the lattice strain. Addition of more oxygen atoms to a vacancy is favored, although the stability decreases for each additional oxygen atom. The charge on each oxygen atom also continues to decrease and the charges on the bonded niobium atoms continue to increase, which

destabilizes these configurations. The lattice strain energy, however, is still less than what it would be if the oxygen atoms were residing in isolated octahedral interstices. Six oxygen atoms residing in one vacancy is less stable than dispersing them to six octahedral interstices. Although lattice strain energy is reduced for hydrogen migration from a tetrahedral binding site to a vacancy binding site, the magnitude is considerably less than for oxygen migration from an octahedral site to a vacancy site.

One hydrogen atom and one oxygen atom can occupy a single vacancy at about the same energy compared to when they are located in different vacancies. When the vacancy is, however, filled with four oxygen atoms, it becomes unfavorable for hydrogen atoms to fill the remaining two octahedral-like absorption sites. Furthermore, similar to the distribution shown in Figure 6.2 for hydrogen atom trapping by an interstitial oxygen atom, many of the tetrahedral sites surrounding a vacancy occupied by oxygen atoms are blocked from occupation by hydrogen atoms. I found a similar trapping configuration for an oxygen atom in a vacancy binding site and a hydrogen atom in a tetrahedral lattice site as for an oxygen atom in an octahedral site and a hydrogen atom in a tetrahedral site with a similar trapping energy, -0.10 eV; therefore, oxygen atoms do not lose their ability to trap hydrogen atoms by occupying niobium lattice vacancies.

Implications for Superconducting Radio-Frequency Cavity Processing

Based on my results and a literature review, I suggest a mechanism for the success of the low-temperature anneal (120-160 °C): 1. Hydrogen atoms are released from the ordered niobium hydride phases and niobium vacancies, and they diffuse into the niobium bulk. 2. Oxygen atoms

are released from the octahedral niobium interstitial sites and from the oxide layers, and then migrate into the vacancies within the first 100 nm subsurface region; this prevents hydride phases from precipitating around niobium defect nucleation sites in the subsurface region. 3. Hydrogen atoms become trapped by oxygen, nitrogen, and possibly carbon atoms dissolved in the niobium, so they cannot find each other to form the precipitated phases. The evidence is discussed in the following paragraphs.

The niobium-hydrogen phase diagram [32] indicates that there shouldn't be precipitated niobium hydride phases above 90 °C for a hydrogen concentration of up to ~34 at. %. Therefore, the low temperature anneal should be sufficient to dissociate any pre-existing ordered niobium hydride precipitate phases. The low temperature anneal should also be sufficient to dissociate vacancy-hydride clusters, since Hautojärvi et al. [140] demonstrated via positron–annihilation spectroscopy that this occurs at ~110 °C.

I have demonstrated that the binding energy of oxygen atoms to niobium vacancies is stronger than the binding energy of hydrogen atoms to vacancies, and researchers performing internal friction experiments have shown that oxygen atoms cannot escape from the vacancies below 200 °C [139]. It has also been shown via resistivity experiments that oxygen can migrate to and become trapped at lattice vacancies between 100-175 °C [141, 142]. Oxygen can be supplied to the vacancies by the oxide layers, as it has been shown via x-ray scattering experiments that the oxide phases begin to dissociate in the temperature range of the low-temperature anneal [15-17], or by interstitial oxygen atoms, as it has been determined via multiple experimental methods that

oxygen atoms can diffuse at least 40 nm in niobium in this temperature range [55]. Thus, oxygen from the oxide layers or oxygen dissolved in niobium interstices may become mobile during the low temperature anneal, but get trapped in sinks such as niobium vacancies: this prevents the oxygen in the top 100 nm from diffusing far into the bulk, consistent with the results of the diffuse x-ray scattering experiments [15] which showed that the oxygen released from the oxide layers after a 5 h anneal at 145 °C remained within 10 nm of the oxide-niobium interface. Additionally, when the annealing temperature in [15] was increased to 300 °C the dissolved oxygen had diffused beyond the 10 nm probing depth of the grazing x-rays, consistent with oxygen becoming detrapped from vacancies, and by extension other lattice imperfections, above 200 °C.

The defect concentration of SRF niobium has recently been studied via positron annihilation – Doppler broadening [60]. The researches compared the results of a cavity annealed in air to a cavity annealed in argon for 3 h at 145 °C and did not think that the introduction of oxygen into the cavity from air annealing significantly affected the niobium vacancy concentration. However, the low momentum annihilation fraction (S), which is sensitive to the defect concentration, did exhibit a noticeable difference between these samples (albeit less significant than the difference between samples that were annealed compared to samples that were not annealed, which was interpreted as the detrapping of hydrogen from niobium vacancies during the anneal). Therefore, the migration of oxygen atoms into the vacancies may have occurred during this experiment, but the effect was not pronounced for the specific experimental conditions. Therefore, I suggest further studies into oxygen migration to niobium lattice

vacancies at conditions relevant to SRF cavity processing. For example, it would be useful to perform an isothermal aging experiment at different temperatures between 120 and 160 °C on SRF niobium. Also, positron lifetime experiments may be able to elucidate the difference between oxygen occupied, hydrogen occupied, and unoccupied niobium lattice vacancies. The results of my calculations demonstrate the rearrangement of electrons for these different situations, and the calculated wave functions of the atoms involved in these scenarios can aid in the interpretation of positron experiments.

I have also demonstrated that dissolved oxygen and nitrogen atoms can trap dissolved hydrogen atoms in the bcc niobium lattice; therefore, these impurities can inhibit significantly the kinetics for precipitation of niobium hydrides. I have also shown that dissolved carbon atoms have similar properties to dissolved oxygen and nitrogen atoms, so by extension, carbon can also participate in the prevention of niobium hydride precipitation. These results are consistent with observations of reactor grade niobium being less susceptible to Q-disease than high purity niobium [52].

Finally, experimental studies have demonstrated that nitrogen atoms require a higher temperature to both trap (~300 °C) and liberate (~500 °C) them from a niobium vacancy [139, 141]. Therefore, nitrogen could be used for more aggressive hydrogen sequestration. Furthermore, tetragonal and cubic niobium nitrides have superconducting transition temperatures > 10 K, so their formation would not be detrimental to cavity performance. Therefore, I suggest further

research concerning nitrogen in niobium in the context of suppressing niobium hydride formation.

Summary and Conclusions

I performed a density functional theory study of the electronic and geometric properties of interstitial hydrogen, oxygen, nitrogen, and carbon atoms in niobium, and hydrogen and oxygen atoms in niobium site vacancies. I find that:

- Interstitial hydrogen atoms occupy tetrahedral sites in the bcc niobium lattice; whereas interstitial oxygen, nitrogen, and carbon atoms occupy octahedral sites. Hence, interstitial hydrogen atoms cause a different type of lattice deformation than the other interstitial impurity atoms.
- The niobium lattice strain energy is 0.72 eV less for the absorption of a hydrogen atom than for the absorption of an oxygen or a nitrogen atom, and 0.85 eV less than for the absorption of a carbon atom.
- Dissolved hydrogen atoms can become trapped by dissolved oxygen, nitrogen, and possibly carbon atoms.
- All of the interstitial impurity atoms have partially anionic character in the bcc niobium lattice. Therefore, their Coulomb interactions are repulsive and the trapping of hydrogen atoms by the other types of impurity atoms is due to the elastic deformation of the lattice in the neighborhood of the trapping atom.

- One niobium vacancy is able to absorb up to six hydrogen atoms or four oxygen atoms; however, the absorption of an oxygen atom by a lattice vacancy is 0.38 eV more favorable than the absorption of a hydrogen atom.
- The absorption of an oxygen atom into a niobium lattice vacancy does not prevent the oxygen atom from trapping a hydrogen atom.

Based on the results of this study, oxygen, nitrogen, carbon, and hydrogen atoms, and niobium lattice vacancies may all be involved in the alleviation of Q drop resulting from the low-temperature (120 – 160 °C) anneal. The following mechanism is proposed to explain the extant experimental observations:

- Hydrogen atoms are released from the ordered niobium hydride phases and niobium vacancies, and they diffuse into the niobium bulk.
- Oxygen atoms are released from the octahedral niobium interstitial sites and from the oxide layers, and then migrate into the vacancies in the niobium subsurface: this prevents hydrogen atoms from returning to the vacancies that served as nucleation centers for hydride precipitates.
- Hydrogen atoms become trapped by oxygen, nitrogen, or possibly carbon atoms dissolved in the niobium, so they cannot find each other to form precipitated phases.

Finally, I suggest that nitrogen is further studied in the context of preventing niobium hydride precipitation.

CHAPTER 7. MODELING MAGNETIC IMPURITIES IN NIOBIUM

Abstract

In this chapter I present modeling efforts to describe magnetic impurities in niobium SRF cavities. I used density functional theory to calculate the electronic and magnetic states in the niobium hydrides and oxides, and show that the stoichiometric forms of several of the hydrides and oxides do not retain local magnetic moments. However, models of oxygen deficient niobium pentoxide exhibit local magnetism. The current models represent only a preliminary effort to describe local magnetism in SRF cavities, but are an important beginning to forming a connection between magnetic impurities in niobium and the manufacturing procedure of SRF cavities.

Introduction

It has been suggested within the SRF community that hydrogen [143] and oxygen [58, 59] could create magnetic impurities in niobium which contribute to Q-slope. As discussed in the previous chapters the concentrations of and structures formed by hydrogen and oxygen in the niobium are very sensitive to the processing procedures applied to the cavities. Since the physical origin of magnetic impurities in SRF cavities is not known, an excellent opportunity exists for first principles modeling to shed light on this phenomenon.

In this chapter I present my attempts to model the electronic and magnetic properties of the niobium hydrides and oxides utilizing density functional theory based calculations. The current

models are not yet complete, but nevertheless, an important beginning to understanding the physical origins of magnetic impurities in SRF cavities.

General Models and Methods

Density functional theory implemented in VASP [88, 89] was used to calculate the properties of the α, α', β and ε niobium hydrides and NbO, NbO_2, and Nb_2O_5. The niobium hydrides were modeled as described in Chapter 5. The niobium oxides were modeled as their lowest energy forms: NbO (Pm-3m, 3 formula units per unit cell), NbO_2 (l4-1, 8 formula units per unit cell), and Nb_2O_5 (P2, 14 formula units per unit cell). Defective Nb_2O_5 structures were created by removing 1 of the 70 oxygen atoms in the P2 unit cell; and due to the thin z-dimension of the unit cell, this is equivalent to a chain of oxygen vacancies and a vacancy concentration of ~ 1.4%. This type of chain defective structure is relevant for the defective oxides [12].

The calculation parameters were the same as what was described in Chapters 5 and 6, except the partial occupancies for the wave functions of nonmetallic structures (NbO_2, Nb_2O_5, and $Nb_{28}O_{69}$) were set by the tetrahedron method with Blöchl corrections. All of the structures were initially optimized in the nonmagnetic state. Experimentally determined lattice parameters for NbO [144], NbO_2 [145], and Nb_2O_5 [146] are available in the literature and are < 1% different from my calculated values. Spin polarization was checked for each structure by providing initial positive magnetic moments on all of the atoms in each structure and reoptimizing their geometries. The electronic DOS were calculated with an approximately 0.15/Å gamma-centered k-point mesh and the tetrahedron method with Blöchl corrections.

Stoichiometric Niobium Hydrides and Oxides

The electronic densities of states (DOS) of the niobium hydrides are displayed in Figure 7.1. All of the hydrides are metallic. New states are created just below the niobium d-band as hydrogen is added to the system, which agrees with first principles calculations found in the literature [28, 99, 147]. These new states have little effect on the Fermi energy, but decrease the DOS at the Fermi energy. According to the BCS theory, the superconducting transition temperature decays exponentially with the inverse of the DOS at the Fermi level multiplied by an electron-phonon coupling parameter. Although the electron-phonon coupling parameter is not calculated here, it is clear that the reduction in the DOS at the Fermi level is correlated with the reduction of T_c in the hydride phases [24, 28-30]. All of the hydride structures converged to nonmagnetic states, and no indication of localized spin states is observed.

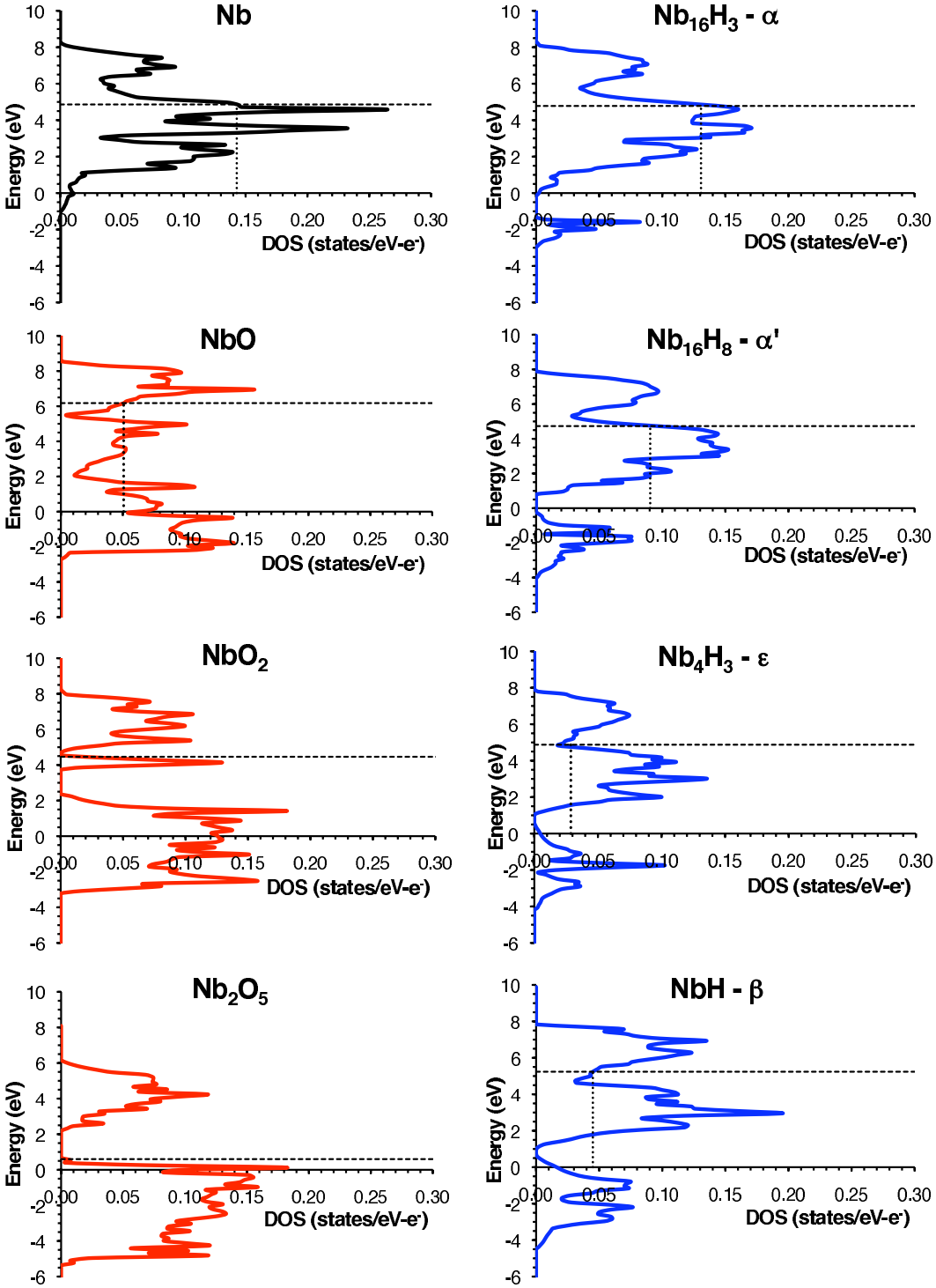

Figure 7.1. Total electronic DOS of bulk niobium, niobium hydrides, and niobium oxides. The dashed horizontal lines indicate the Fermi energy and the dashed vertical lines indicate the DOS at the Fermi level.

The electronic DOS of the niobium oxides are also displayed in Figure 7.1, showing that NbO is metallic and NbO_2 has a small band gap (~0.25 eV), which are well known properties of these materials. A 1.7 eV band gap is found for Nb_2O_5, which is underestimated compared to the 3.4 eV gap determined from UV-Vis DRS measurements [148]. Since DFT was developed to calculate ground state properties, it is not expected to accurately model the excited states and is known to underestimate the band gap in many transition metal oxides. Therefore, I considered the rotationally invariant DFT+U method of Dudarev et al. [149], which is commonly applied to partially correct this problem. This method adds additional on-site Coulomb and exchange terms to the DFT Hamiltonian to account for the poor description of localized d – electrons in standard DFT. U (Coulomb) - J (exchange) is treated as a fitting parameter that is often determined by trial and error until acceptable properties (e.g. band gap) are produced. However, my attempts revealed no significant improvement in the Nb_2O_5 band gap for including a U-J term of up to 10 eV, and at this point the cell volume had increased significantly (~7%). Therefore, I did not continue to use the DFT+U method. Additionally, I tried the GGA-PW91, GGA-PBEsol, and LDA exchange-correlation functionals in place of PBE, and including semi-core s electrons in the basis sets but there was still no significant improvement. Considering the accurate geometries of the structures and qualitative electronic DOS obtained from PBE and standard DFT, the results presented for the oxides in this chapter should be considered qualitatively. Nb_2O_5, NbO_2, and NbO all converged to nonmagnetic states.

Defective Niobium Oxides

The niobium oxides exist in broad ranges of stoichiometries, described as Nb_2O_{5-d}. This family of structures can be represented by NbO_6 octahedra connected into blocks of columns along shared edges. In some structures, NbO_4 units exist near the corners of the columns to provide the correct stoichiometry. This arrangement accommodates oxygen vacancies by allowing the blocks to shear along the edges. The P2 structure of Nb_2O_5 can be represented this way, as shown in Figure 7.2.

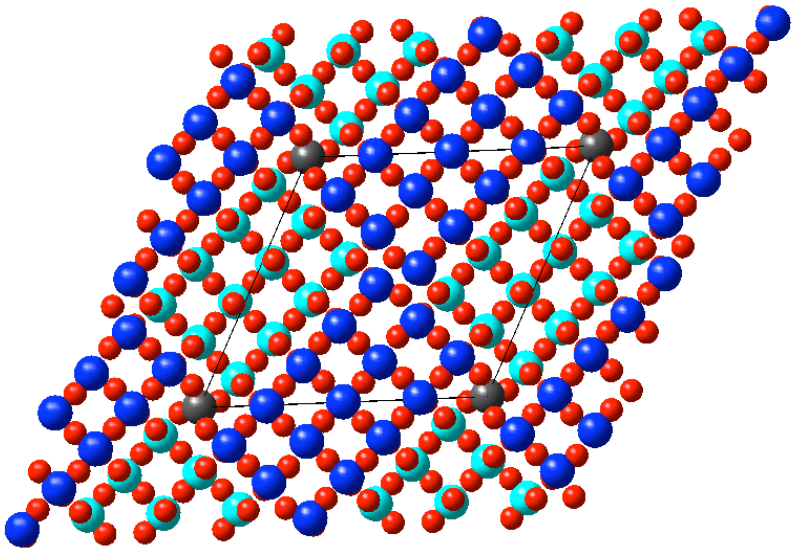

Figure 7.2. The P2, also called h-, Nb_2O_5 structure. Large dark and light blue spheres represent niobium atoms that are octahedrally coordinated to oxygen atoms; the light spheres are one plane below the dark spheres. Large grey spheres represent niobium atoms that are tetrahedrally coordinated to oxygen atoms and small red spheres represent oxygen atoms. The unit cell is outlined in black.

Many magnetic structures were produced by removing one oxygen from the P2 Nb_2O_5 unit cell, Figure 7.3. The structures that required the least amount of energy to create have localized magnetic moments, Figure 7.4, and were created by removing one of the oxygen atoms near the

tetrahedrally coordinated niobium atom. Cava, et al. [12] created several Nb_2O_{5-d} structures by gettering and determined from magnetic susceptibility measurements that the concentration of magnetic impurities increases with increasing d. They discussed possible modeling of Nb_2O_{5-d} structures as $Nb_x^{4+}Nb_y^{5+}O_z$, but the effective magnetic moment extracted from their data set indicated only 0.8 μ_B (~0.45 e^-) / Nb^{4+}. This indicates that not all of the electrons are localized, which corroborates with the decrease in electrical resistivity that they measured with increasing d and the qualitative electron DOS that I present in Figure 7.1. The magnitude of the effective magnetic moments that I calculate for my models is similar to what Cava, et al. finds. The effective magnetic moment is calculated as $g(S(S+1))^{1/2}$, where g Landé g-factor (2.0023 for an electron) and S is the spin quantum number. Writing the chemical composition of my defective oxide model, $Nb_{28}O_{69}$, as $Nb_x^{4+}Nb_y^{5+}O_z$ gives x=2 and y=26. Therefore the lowest energy structure that I calculated would have an effective magnetic moment of 0.58 μ_B / Nb^{4+}.

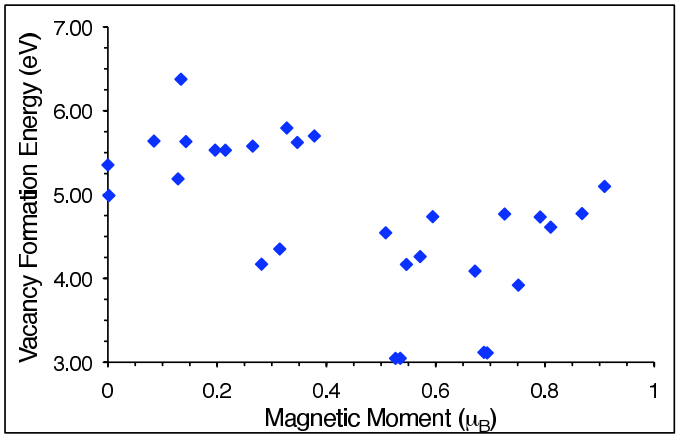

Figure 7.3. The energy to form one oxygen vacancy from the P2 structure of Nb_2O_5 versus the total magnetic moment of the $Nb_{28}O_{69}$ unit cell. This data set includes the removal of each of the symmetrically unique oxygen atoms.

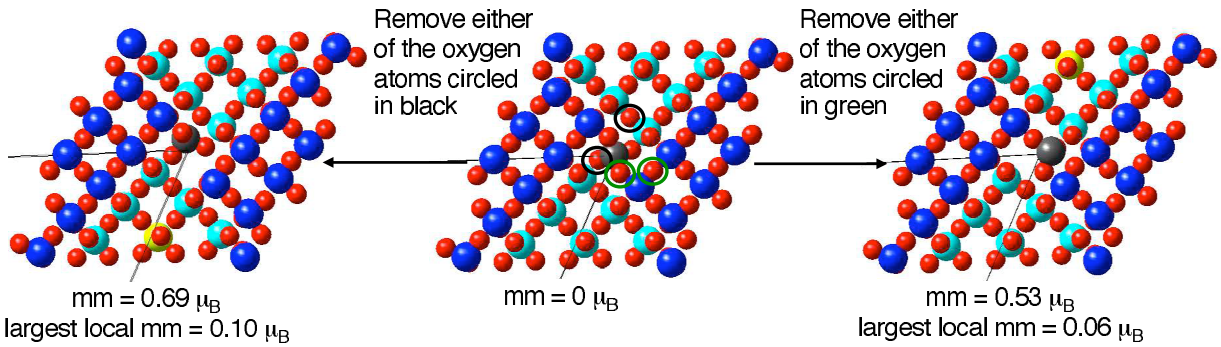

Figure 7.4. Illustration of the creation of the lowest-energy configurations of $Nb_{28}O_{69}$ from P2 Nb_2O_5. The vacancy formation energies are 3.11 eV for the structure on the left and 3.05 eV for the structure on the right. The color coding of the niobium atoms (shades of blue and grey) reflects the coordination and location of the atoms in the ideal P2 Nb_2O_5 structure, see Figure 7.2 for details. The niobium atom retaining the largest local magnetic moment in each unit cell is colored yellow. The oxygen atoms are represented by small red spheres.

The oxygen vacancy formation energies plotted in Figure 7.3 were calculated as $E(Nb_{28}O_{69}) - E(Nb_{28}O_{70}) + ½ E(\text{gas phase } O_2)$. GGA and LDA are both known to give substantial error in the calculation of the gas phase O_2 atomization energy, although the bond length for O_2 is accurately predicted by GGA calculations; therefore, a correction of 1.36 eV has been established for the O_2 gas phase energy for use in the data analysis of GGA calculations [150]. With the correction, the heats of formation of the NbO, NbO_2, and Nb_2O_5 are within 8% of the values determined experimentally [151], which indicates the magnitude of error in the energy that can be expected for Nb-O systems.

Discussion

The thickness, structure, and stoichiometry of the oxide layers depend strongly on their formation conditions. Differences in the stoichiometry and thickness of the oxide coating were observed after different heat and chemical treatment by atom probe tomography [152-154].

When water is present, the oxide forms at a rate of 0.1 nm/s and has a high defect concentration, whereas dry oxidation in an O_2 atmosphere is much slower, $5x10^{-6}$ nm/s, and forms a more uniform oxide layer [27]. The composition of the oxides is also affected by the low-temperature anneal [15-17]. Therefore, it is important to understand how the properties of the oxides affect niobium SRF cavities. The preliminary models that I presented, as well as the magnetic susceptibility measurements in [12], indicate that Nb_2O_{5-d} structures could contain localized magnetic moments. Furthermore, single oxygen vacancies may exist for $d < 0.015$, and electrical resistance experiments indicate that single oxygen vacancies can be singly or doubly charged with a formation energy of only ~2.8 eV [155]. Therefore, it may important to include these types of defects in the future development of models of magnetic impurities in niobium.

The possibility of magnetic impurities produced by means other than defects in the surface oxides should also be considered. Casalbuoni et al. [57] measured the magnetic susceptibility of SRF niobium and found evidence for magnetic impurities at concentrations two orders of magnitude higher than would be expected from d=0.17 in a 5 nm thick surface oxide. They therefore suggested that other absorbed or surface chemical impurities may be responsible. Although my initial attempts to search for magnetic impurities created by hydrogen did not find any, only a subset of possible structures was examined. Additionally, only ferromagnetic structures were searched.

In conclusion, given the potential importance of understanding the role of magnetic impurities provided by hydrogen and oxygen in niobium to cavity performance and the results from the

current modeling attempts, it would be beneficial to build rigorous quantitative first principles models of magnetic impurities in SRF cavities.

CHAPTER 8. CONCLUSIONS AND RECOMMENDED FUTURE WORK

Density functional theory and Raman, infrared, and nuclear magnetic resonance spectroscopy have been utilized to provide insight to the fundamental processes that occur during the manufacturing of niobium superconducting radio-frequency cavities.

I presented chemical analyses of the acid solution used in the electropolishing process that indicated that fluorine is bound and released by a reaction between the acid components in the solution: $HF + H_2SO_4 <-> HFSO_3 + H_2O$. This result implies that new recipes can possibly be developed on the principle of controlled release of fluorine by a chemical reaction, which provides a route to improve the safety and effectiveness of electropolishing. Additionally, a detailed understanding of why this specific recipe works so well could aid in the development of fluorine free recipes. Therefore, further studies into the mechanisms of electropolishing niobium with the standard recipe are recommended. For example, density theory calculations paired infrared spectroscopy could potentially aid in the understanding of the chemical reactions occurring on the niobium surface.

I also presented the results of density functional theory calculations of chemical impurities absorbed into the niobium during processing. I showed that hydrogen absorbs exothermically into niobium from the gas phase and becomes partially anionic. I presented evidence that a vacancy can serve as a nucleation center for hydride phase formation, so then small hydride precipitates could occur near the lattice vacancies during cavity cool-down. I also explained the

phase changes in the niobium hydrogen system based on the charge transfer between niobium and hydrogen, the strain field inside of the niobium, and the geometry of the phases. These results suggest that the recovery state of niobium should be monitored during processing. By extension of the vacancy nucleation results and other studies in the archival literature, the nucleation of hydride phases around dislocations and grain boundaries may be of basic and practical interest to further examine. Therefore, I recommend creating first principles models of these structures to obtain fundamental details about the occurrences of these processes.

I also provided guidance for cavity processing based on density functional theory calculations of the properties of common processing impurity species – hydrogen, oxygen, nitrogen, and carbon – in the bcc niobium lattice. I demonstrated that some fundamental properties are shared between the impurity atoms, such as anionic character in niobium, but the strain field produced by the hydrogen atoms is both geometrically different and substantially weaker than the strain field produced by the other impurities. I demonstrated that the elastic interactions between hydrogen and oxygen with the bcc niobium lattice cause trapping of these species by niobium lattice vacancies. I also show that the attraction of oxygen to a lattice vacancy is substantially stronger than the attraction of hydrogen to the vacancy, indicating that oxygen can block vacancies from absorbing hydrogen. Additionally I showed that dissolved oxygen atoms can trap dissolved hydrogen atoms, which prevents hydrogen atoms from finding each other to form detrimental phases. These results provide insight to the mechanism of the low-temperature anneal applied to SRF cavities and give indication of improvements that may be made to the process. However, several complimentary experimental studies were recommended to further

validate the predictions of these calculations. Although the focus of this study was on the interaction between oxygen and hydrogen atoms in the lattice, I also showed from some simple calculations that the behavior of nitrogen and carbon in niobium is similar to that of oxygen. Therefore, I recommend further examination of nitrogen and carbon in bcc niobium, and particularly the role that nitrogen can play in preventing detrimental hydride phase formation.

Finally, I presented the beginning of a computational model to describe magnetic impurities in niobium SRF cavities. From density functional theory calculations, I showed that the stoichiometric forms of several niobium hydrides and oxides do not retain local magnetic moments. However, preliminary models of oxygen deficient niobium pentoxide exhibit local magnetism. I discussed several deficiencies in the current models, but based on the preliminary results and intriguing experimental results presented in the literature, I recommend construction of comprehensive quantitative models based on first principles calculations to describe magnetic impurities in SRF niobium.

REFERENCES

[1] 2011 International Linear Collider A Technical Progress Report. ed E Elsen, *et al*.

[2] Kneisel P 2003 Surface characterization of bulk Nb: What has been done, what has been learnt? In: *11th Workshop on RF Superconductivity,* (Lübeck, Germany p 206)

[3] Aune B, Bandelmann R, Bloess D, Bonin B, Bosotti A, Champion M, Crawford C, Deppe G, Dwersteg B, Edwards D A, Edwards H T, Ferrario M, Fouaidy M, Gall P-D, Gamp A, Gossel A, Graber J, Hubert D, Huning M, Juillard M, Junquera T, Kaiser H, Kreps G, Kuchnir M, Lange R, Leenen M, Liepe M, Lilje L, Matheisen A, Moller W-D, Mosnier A, Padamsee H, Pagani C, Pekeler M, Peters H-B, Peters O, Proch D, Rehlich K, Reschke D, Safa H, Schilcher T, Schmuser P, Sekutowicz J, Simrock S, Singer W, Tigner M, Trines D, Twarowski K, Weichert G, Weisend J, Wojtkiewicz J, Wolff S and Zapfe K 2000 Superconducting TESLA cavities *Phys. Rev. ST Accel. Beams* **3** 092001

[4] Schmuser P 2002 Superconductivity in high energy particle accelerators *Prog. Part. Nucl. Phys.* **49** 155-244

[5] Bonin B 1995 Materials for Superconducting Cavities. In: *CERN Accelerator School Superconductivity in Particle Accelerators,* ed S Turner (Hamburg, Germany pp 191-200)

[6] French R A 1968 Intrinsic type-2 superconductivity in pure niobium *Cryogenics* **8**

[7] London F and London H 1935 *Proc. R. Soc. London, Ser. A* **149** 71-88

[8] Bardeen J, Cooper L N and Schrieffer J R 1957 *Phys. Rev.* **108**

[9] Pippard A B 1953 *Proc. R. Soc. London, Ser. A* **216** 547-68

[10] Singer W, Singer X and Wen H M 2003 *Materiaux & Techniques* **91** 13-8

[11] Cooley L and Champion M 2007 Technical specifications for high RRR grade niobium sheet and rod for use in superconducting cavities. In: *Fermilab Engineering Specification*

[12] Cava R J, Batlogg B, Krajewski J J, Poulsen H F, Gammel P, Peck W F and Rupp L W 1991 Electrical and magnetic-properties of Nb2O5-delta crystallographic shear structures *Phys. Rev. B* **44** 6973-81

[13] Abrikosov A A and Gor'kov L P 1961 Contribution to the theory of superconducting alloys with paramagnetic impurities *Sov. Phys. JETP* **12** 1243-53

[14] DeSorbo W 1963 Effect of dissolved gases on some superconducting properties of niobium *Phys. Rev.* **132** 107

[15] Delheusy M, Stierle A, Kasper N, Kurta R P, Vlad A, Dosch H, Antoine C, Resta A, Lundgren E and Andersen J 2008 X-ray investigation of subsurface interstitial oxygen at Nb/oxide interfaces *Appl. Phys. Lett.* **92** 101911

[16] Ma Q, Ryan P, Freeland J W and Rosenberg R A 2004 Thermal effect on the oxides on Nb(100) studied by synchrotron-radiation x-ray photoelectron spectroscopy *J. Appl. Phys.* **96** 7675-80

[17] Tian H 2007 Surface oxide study on solid niobium for superconducting RF accelerators using variable photon energy XPS. In: *SRF Workshop,* (Fermilab, Batavia, IL)

[18] Kim Y-J, Tao R, Klie R F and Seidman D N 2013 Direct atomic-scale imaging of Nb-hydrides and oxides using atom-probe tomography and aberration-corrected STEM/EELS *ACS Nano* **7** 732-9

[19] Romanenko A and Goncharova L V 2011 Elastic recoil detection studies of near-surface hydrogen in cavity-grade niobium *Supercond. Sci. Tech.* **24** 105017

[20] Antoine C 1991 Hydrogen in niobium : the analytical approach. In: *Proc. of the 5th Workshop on RF superconductivity,* (DESY, Hambourg, Germany)

[21] Ciovati G 2004 Effect of low-temperature baking on the radio-frequency properties of niobium superconducting cavities for particle accelerators *J. Appl. Phys.* **96** 1591-601

[22] Ciovati G, Myneni G, Stevie F, Maheshwari P and Griffis D 2010 High field Q slope and the baking effect: review of recent experimental results and new data on Nb heat treatments *Phys. Rev. ST Accel. Beams* **13** 022002

[23] Ricker R E and Myneni G R 2010 Evaluation of the propensity of niobium to absorb hydrogen during fabrication of superconducting radio frequency cavities for particle accelerators *J. Res. Natl. Inst. Stand. Technol.* **115** 353-71

[24] Isagawa S 1980 Hydrogen absorption and its effect on low-temperature electric properties of niobium *J. Appl. Phys.* **51** 4461-70

[25] Myers S M, Baskes M I, Birnbaum H K, Corbett J W, DeLeo G G, Estreicher S K, Haller E E, Jena P, Johnson N M, Kirchheim R, Pearton S J and Stavola M J 1992 Hydrogen interactions with defects in crystalline solids *Rev. Mod. Phys.* **64** 559-617

[26] Khaldeev G V and Gogel V K 1987 Physical and corrosion-electrochemical properties of the niobium hydrogen system *Russ. Chem. Rev.* **56**

[27] Halbritter J 1987 On the oxidation and on the superconductivity of niobium *Appl. Phys. A* **43** 1-28

[28] Jisrawi N M, Ruckman M W, Thurston T R, Reisfeld G, Weinert M, Strongin M and Gurvitch M 1998 Reversible depression in the Tc of thin Nb films due to enhanced hydrogen adsorption *Phys. Rev. B* **58** 6585-91

[29] Ohlendorf D and Wicke E 1979 Heat capacities between 1.5 and 16 K and superconductivity of V/H and Nb/H alloys *J. Phys. Chem. Solids* **40** 721-8

[30] Welter J-M and Johnen F J 1977 Superconducting transition temperature and low temperature resistivity in the niobium-hydrogen system *Z. Physik B* **27** 227-32

[31] Fukai Y 2005 *The Metal-Hydrogen System* (Berlin: Springer)

[32] Manchester F D and Pitre J M 2000 (Materials Park, OH: ASM International)

[33] Dzyuba A, Romanenko A and Cooley L D 2010 Model for initiation of quality factor degradation at high accelerating fields in superconducting radio-frequency cavities *Supercond. Sci. Tech.* **23**

[34] Saito K, Inoue H, Kako E, Fujino T, Noguchi S, Ono M and Shishido T 1998 Superiority of electropolishing over chemical polishing on high gradients *Part. Accel.* **60** 193-217

[35] Cooley L 2010 Materials issues from recent cavity experience and in view of a 650 MHz option for Project X. In: *SRF Materials Workshop,* (Tallahassee, Florida)

[36] Ge M, Wu G, Ruan J, Nicol T and Cooley L 2010 Restoration of maximum gradient by laser re-melting a cavity pit. In: *SRF Materials Workshop,* (Tallahassee, Florida)

[37] Tegart W J M 1959 *The Electrolytic and Chemical Polishing of Metals in Research and Industry* (London: Pergamon Press Ltd)

[38] Cooley L D, Burk D, Cooper C, Dhanaraj N, Foley M, Ford D, Gould K, Hicks D, Novitski R, Romanenko A, Schuessler R, Thompson C and Wu G 2010 Impact of forming, welding, and electropolishing on pitting and the surface finish of SRF cavity niobium *Ieee T. Appl. Supercon.* **21** 2609-14

[39] Diepers H, Schmidt O, Martens H and Sun F S 1971 New method of electropolishing niobium *Phys. Lett. A* **A 37** 139-40

[40] Saito K, Kojima Y, Furuya T, Mitsunobu S, Noguchi S, Hosoyama K, Nakazato T, Tajima T and Asano K 1989 In: *Proceedings of the 4th Workshop on RF Superconductivity,* (KEK, Tsukuba, Japan pp 635-94)

[41] Kneisel P, Stoltz O and Halbritter J 1974 Surface preparation and measurement of niobium used in high-frequency cavities *J. Appl. Phys.* **45** 2296-301

[42] Pourbaix M 1966 *Atlas of Electrochemical Equilibria in Aqueous Solution* (London: Pergamon)

[43] Aspart A and Antoine C Z 2004 Study of the chemical behavior of hydrofluoric, nitric and sulfuric acids mixtures applied to niobium polishing *Appl. Surf. Sci.* **227** 17-29

[44] Lange W 1933 Das gleichgewicht H2SO4+HF<->HSO3F+H2O und seine beeinflussung durch starke säuren *Z. Anorg. Allgem. Chem.* **215** 321-32

[45] Antoine C Z and Berry S 2003 H in niobium: origin and method of detection *Aip Conf. Proc.* **671** 176-89

[46] Aspart A, Eozenou F and Antoine C 2006 Aluminum and Sulfur Impurities in Electropolishing Baths *Physica C* **441** 249-53

[47] Zhao X, Geng R-L, Tyagi P V, Hayano H, Kato S, Nishiwaki M, Saeki T and Sawabe M 2010 Surface characterization of Nb samples electropolished with real superconducting rf accelerator cavities *Phys. Rev. ST Accel. Beams* **13** 124702

[48] Wu A T, Mammosser J, Phillips L, Delayen J, Reece C, Wilkerson A, Smith D and Ike R 2007 Smooth Nb surfaces fabricated by buffered electropolishing *Appl. Surf. Sci.* **253** 3041-52

[49] Inman M, Taylor E J and Lozano-Morales A 2010 Faradayic electropolishing of niobium in an HF-free electrolyte. In: *6th SRF Materials Workshop,* (Tallahassee, Florida)

[50] Hoyt E W 1972 Niobium surfaces for rf superconductors *J. Vac. Sci. Technol.* **9** 144-54

[51] Padamsee H 2009 *RF Superconductivity Science, Technology and Applications* vol II (Weinheim: Wiley-VCH)

[52] Knobloch J 2003 The "Q disease" in superconducting niobium RF cavities. In: *Hydrogen in Materials & Vacuum Systems: First International Workshop on Hydrogen in Materials and Vacuum Systems,* ed G R Myneni and S Chattopadhyay (Melville, New York: AIP) pp 133-50

[53] Barkov F, Romanenko A and Grassellino A 2012 Direct observation of hydrides formation in cavity-grade niobium *Phys. Rev. ST Accel. Beams* **15** 122001

[54] Ciovati G 2006 Review of the frontier workshop and Q-slope results *Physica C* **441** 44-50

[55] Powers R W and Doyle M V 1959 Diffusion of interstitial solutes in the group V transition metals *J. Appl. Phys.* **30** 514-24

[56] Ciovati G 2006 Improved oxygen diffusion model to explain the effect of low-temperature baking on high field losses in niobium superconducting cavities *Appl. Phys. Lett.* **89** 022507

[57] Casalbuoni S, Knabbe E-A, Kotzler J, Lilje L, Sawilski L v, Schmuser P and Steffen B 2005 Surface superconductivity in niobium for superconducting RF cavities *Nucl. Instrum. Meth. A* **538** 45-64

[58] Proslier T, Zasadzinski J, Cooley L, Pellin M, Norem J, Elam J, Antoine C Z, Rimmer R A and Kneisel P 2009 Tunneling study of SRF cavity-grade niobium *Ieee T. Appl. Supercon.* **19** 1404-8

[59] Proslier T, Zasadzinski J F, Cooley L, Antoine C, Moore J, Norem J, Pellin M and Gray K E 2008 Tunneling study of cavity grade Nb: Possible magnetic scattering at the surface *Appl. Phys. Lett.* **92** 212505

[60] Visentin B, Barthe M F, Moineau V and Desgardin P 2010 Involvement of hydrogen-vacancy complexes in the baking effect of niobium cavities *Phys. Rev. ST Accel. Beams* **13** 052002

[61] Romanenko A and Padamsee H 2010 The role of near-surface dislocations in the high magnetic field performance of superconducting niobium cavities *Supercond. Sci. Tech.* **23** 045008

[62] Romanenko A, Barkov F, Cooley L D and Grassellino A 2013 Proximity breakdown of hydrides in superconducting niobium cavities *Supercond. Sci. Tech.* **26** 035003

[63] de Gennes P G 1989 *Superconductivity of Metal and Alloys* (Redwood City, CA: Addison-Wesley)

[64] Gurevich A and Ciovati G 2008 *Phys. Rev. B* **77** 104501-21

[65] Hafner J 2008 Ab-initio simulations of materials using VASP: Density-functional theory and beyond *J. Comp. Chem.* **29**

[66] Kirchner B, Dio P J d and Hutter J 2011 Real-world predictions from ab initio molecular dynamics simulations *Top. Curr. Chem.* **307** 109-54

[67] Hohenberg P and Kohn W 1964 *Phys. Rev.* **136** B864

[68] Kohn W and Sham L J 1965 *Phys. Rev.* **140** A1133

[69] Press W H, Flannery B P, Teukolsky S A and Vetterling W T 1986 *Numerical Recipes* (New York: Cambridge University Press)

[70] Tang W, Sanville E and Henkelman G 2009 *J. Phys. Condens. Mat.* **21** 084204

[71] Sanville E, Kenny S D, Smith R and Henkelman G 2007 *J. Comput. Chem.* **28** 899

[72] Henkelman G, Arnaldsson A and Jónsson H 2006 *Comput. Mater. Sci.* **36** 254

[73] Tian H, Corcoran S G, Reece C E and Kelley M J 2008 The mechanism of electropolishing of niobium in hydrofluoric-sulfuric acid electrolyte *J. Electrochem. Soc.* **155** D563-D8

[74] Lee S-J, Lai J-J and Lin Y-T 2005 Simulation of the formation mechanism of a viscous layer for the electropolishing process *WIT Trans. Eng. Sci.* **48** 203-13

[75] Subramanian S, Xue Q, Trabia M, Chen Y and Schill R J 2002 Modeling and optimization of the chemical etching process in niobium cavities. In: *2002 International Congress on Advances in Nuclear Power Plants,* (Hollywood, Florida)

[76] Ciovati G, Higo T, Kneisel P, Mammosser J, Matheisen A, Michelato P, Padamsee H, Reschke D, Rothgeb T, Saeki T, Saito K, Visentin B, Weise H and Oevermann C 2008 Final surface preparation for superconducting cavities - an attempt to describe an optimized procedure. In: *TTC - Reports*

[77] Tian H and Reece C E 2010 Evaluation of the diffusion coefficient of fluorine during the electropolishing of niobium *Phys. Rev. ST Accel. Beams* **13** 083502

[78] Eozenou F, Aspart A, Antoine C and Malki B 2003 Electropolishing of niobium: best EP parameters. In: *CARE*

[79] Bruchon M, Visentin B and Eozenou F 2007 Electropolishing on single and multi-cell: Comsol modeling. In: *13th International Workshop on RF Superconductivity,* (Beijing, China)

[80] Kang G, Lee K, Park H, Lee J, Jung Y, Kim K, Son B and Park H 2010 Quantitative analysis of mixed hydrofluoric and nitric acids using Raman spectroscopy with partial least squares regression *Talanta* **81** 1413-7

[81] Gillespie R J and Robinson E A 1961 The Raman spectra of sulphuric, deuterosulphuric, fluorosulphuric, chlorosulphuric, and methanesulphonic acids and their anions *Can. J. Chem.* **40** 644-57

[82] Keller O L 1963 Identification of complex ions of niobium(V) in hydrofluoric acid solutions by Raman and infrared spectroscopy *Inorg. Chem.* **2** 783-7

[83] Vonbarner J H, Christensen E, Bjerrum N J and Gilbert B 1991 Vibrational-spectra of niobium(V) fluoro and oxo fluoro complexes formed in alkali-metal fluoride melts *Inorg. Chem.* **30** 561-6

[84] Schaumburg K and Deverell C 1968 Fluorine-19 nuclear magnetic resonance chemical shift of hydrofluoric acid in H2O and D2O solutions *J. Am. Chem. Soc.* **90** 2495-9

[85] Christe K O and Wilson W W 1990 Nuclear magnetic resonance spectrum of the fluoride anion *J. Fluorine Chem.* **46** 339-42

[86] Gillespie R J, Milne J B and Senior J B 1966 *Inorg. Chem.* **5** 1233-5

[87] Dorsey N E 2003 Viscosity of water, sulfuric acid, liquid carbon dioxide, and certain organic liquids. In: *International Critical Tables*: (Knovel)

[88] Kresse G and Hafner J 1993 Abinitio molecular-dynamics for liquid-metals *Phys. Rev. B* **47** 558-61

[89] Kresse G and Furthmuller J 1996 Efficient iterative schemes for ab initio total-energy calculations using a plane-wave basis set *Phys. Rev. B* **54** 11169-86

[90] Perdew J P, Burke K and Ernzerhof M 1996 *Phys. Rev. Lett.* **77** 3865

[91] Kresse G and Joubert D 1999 *Phys. Rev. B* **59** 1758-75

[92] Blöchl P E 1994 *Phys. Rev. B* **50** 17953-79

[93] Monkhorst H J and Pack J D 1976 *Phys. Rev. B* **13** 5188-92

[94] Huber K P and Herzberg G 1979 *Molecular Spectra and Molecular Structure. IV. Constants of Diatomic Molecules* (New York: Van Nostrand Reinhold Co.)

[95] 1991 *Atomic Defects in Metals* vol 25 (Berlin: Springer-Verlag)

[96] Korzhavyi P A, Abrikosov I A and Johansson B 1999 First-principles calculations of the vacancy formation energy in transition and noble metals *Phys. Rev. B* **59** 11693-703

[97] Korhonen T, Puska M J and Nieminen R M 1995 Vacancy-formation energies for fcc and bcc transition metals *Phys. Rev. B* **51** 9526-32

[98] Schober T, Pick M A and Wenzl H 1973 Electron microscopy of b-hydride in niobium *Phys. Status Solidi A* **18** 175-82

[99] Aboud S and Wilcox J 2010 A density functional theory study of the charge state of hydrogen in metal hydrides *J. Phys. Chem. C* **114** 10978-85

[100] Rao J-P, Ouyang C-Y, Lei M-S and Jiang F-Y 2011 Vacancy and H interactions in Nb *Chin. Phys. Lett.* **28** 12701

[101] Veleckis E and Edwards R K 1969 Thermodynamic properties in the systems vanadium-hydrogen, niobium-hydrogen, and tantalum-hydrogen *J. Phys. Chem.* **73** 683-92

[102] Pryde J A and Titcomb C G 1972 Thermodynamic data of the hydrogen-niobium system *J. Phys. C* **5** 1301-8

[103] Pauling L 1960 *The Nature of the Chemical Bond*: (Cornell University)

[104] Allred A L 1961 *J. Inorg. Nucl. Chem.* **17** 215-21

[105] Pundt A and Kirchheim R 2006 Hydrogen in metals: Microstructural aspects *Annu. Rev. Mater. Res.* **36** 555-608

[106] Nordlander P, Nørskov J K, Besenbacher F and Myers S M 1989 Multiple deuterium occupancy of vacancies in Pd and related metals *Phys. Rev. B* **40** 1990-2

[107] Koike H, Shizuku Y, Yazaki A and Fukai Y 2004 Superabundant vacancy formation in Nb–H alloys; resistometric studies *J. Phys.: Condens. Matter* **16** 1335–49

[108] Cizek J, Prochazka I, Becvar F, Kuzel R, Cieslar M, Brauer G, Anwand W, Kirchheim R and Pundt A 2004 Hydrogen-induced defects in bulk niobium *Phys. Rev. B* **69** 224106

[109] Cizek J, Prochazka I, Danis S, Brauer G, Anwand W, Gemma R, Nikitin E, Kirchheim R, Pundt A and Islamgaliev R K 2009 Hydrogen-vacancy complexes in electron-irradiated niobium *Phys. Rev. B* **79** 054108

[110] Fukai Y and Okuma N 1993 *Japan J. Appl. Phys.* **32** L1256

[111] Fukai Y and Okuma N 1994 *Phys. Rev. Lett.* **73** 1640

[112] Albrecht W M, Goode W D and Mallett M W 1959 Reactions in the niobium-hydrogen system *J. Electrochem. Soc.* **106** 981-6

[113] Peisl H 1978 *Hydrogen in Metals I, Topics in Applied Physics* vol 28 (Berlin: Springer-Verlag)

[114] Kim Y-J, Seidman D N, Tao R and Klie R F Direct atomic-scale imaging of Nb-hydrides and oxides using atom-probe tomography and aberration-corrected STEM/EELS *submitted to Nat. Mater.*

[115] Romero A H, Schuller I K and Ramirez R 1998 Subsurface bonding of hydrogen in niobium: A molecular-dynamics study *Phys. Rev. B* **58** 15904-8

[116] Lagos M, Martinez G and Schuller I K 1984 Kinetics of hydrogen absorption in transition metals and subsurface bonding *Phys. Rev. B* **29** 5979-81

[117] Lagos M and Schuller I K 1984 Enhancement of hydgrogen uptake in metals and subsurface bonding *Surf. Sci.* **138** L161-L7

[118] Li Y, Erskine J L and Diebold A C 1986 High-resolution electron-energy-loss spectroscopy of hydrogen chemisorption at Nb(100) surfaces: Evidence for subsurface absorption sites *Phys. Rev. B* **34** 5951-4

[119] Fang B-S, Ballentine C A and Erskine J L 1987 Electronic properties of Nb and H-treated Nb surfaces *Phys. Rev. B* **36** 7360-3

[120] Smith R J 1980 Characterization of the hydrogen adsorption/absorption process for Nb(110) with surface spectroscopy *Phys. Rev. B* **45** 1277-80

[121] Smith R J 1980 Photoemission studies of hydrogen chemisorption on Nb *Phys. Rev. B* **21** 3131-6

[122] Cabrera A L, Espinosa-Gangas J, Jonsson-Akerman J and Schuller I K 2002 Kinetics of subsurface hydrogen adsorbed on niobium: Thermal desorption studies *J. Mater. Res.* **17** 2698-704

[123] Blomqvist A, Pálsson G K, Araújo C M, Ahuja R and Hjörvarsson B 2010 Significance of self-trapping on hydrogen diffusion *Phys. Rev. Lett.* **105** 185901

[124] Sundell P G and Wahnstrom G 2004 Self-trapping and diffusion of hydrogen in Nb and Ta from first principles *Phy. Rev. B* **70** 224301

[125] Mauger P, Williams W and Cotts R 1981 Diffusion and NMR spin lattice relaxation of 1H in alpha' TaHx and NbHx *J. Phys. Chem. Solids* **42** 821-6

[126] Bauer H, Völkl J, Tretkowski J and Alefeld G 1978 Diffusion of hydrogen and deuterium in Nb and Ta at high concentration. *Z. Physik B* **29** 17-26

[127] Baker C and Birnbaum H K 1973 Anelastic studies of hydrogen diffusion in niobium *Acta Metall.* **21** 865-72

[128] Pfeiffer G and Wipf H 1975 The trapping of hydrogen in niobium by nitrogen interstitials *J. Phys. F: Met. Phys.* **6** 167-79

[129] Shirley A I, Hall C K and Prince N J 1983 Trapping of hydrogen by oxygen and nitrogen impurities in niobium, vanadium and tantalum *Acta Metall.* **31** 985-92

[130] Mattas R F and Birnbaum H K 1975 Isotope effects on the motion of O-H clusters in Nb *Acta Metall.* **23** 973-7

[131] Blanter M S 1994 Interaction of dissolved atoms and "hydrogen snoek-type relaxation" in Nb and Ta (computer simulation) *J. Alloy Compd.* **211/212** 45-9

[132] Schiller P and Nijam A 1975 *Phys. Stat. Sol. A* **31** K77

[133] Zapp P E and Birnbaum H K 1980 Solute trapping of hydrogen in niobium - symmetry of the O-H pair *Acta Metall.* **28** 1275-86

[134] Metzgert T H, Schubert U and Peisl J 1985 The trapping of hydrogen at nitrogen in niobium investigated by diffuse X-ray scattering *J. Phys. F: Met. Phys.* **15** 779-97

[135] Yagi E, Hirabayashi K, Murakami Y, Koike S, Higami N, Hayashi T, Takebayashi A, Yoshida T, Sugi C, Sugawar T, Shishido T and Ogiwara K 2008 Site change of hydrogen in Nb due to interaction with oxygen *J. Phys. Soc. Japan* **77** 054802

[136] Magerl A, Rush J J, Rowe J M, Richter D and Wipf H 1983 Local hydrogen vibrations in Nb in the presence of interstitial (N,O) and substitutional (V) impurities *Phys. Rev. B* **27** 927-34

[137] Hanada R 1977 Recovery of H and D quenched to 4.2K in interstitial impurities doped Nb and Ta. In: *Second International Congress on Hydrogen in Metals,* (Paris, France p 1B6)

[138] Huang K F, Granato A V and Birnbaum H K 1985 Ultrasonic relaxation from trapped hydrogen in rapidly cooled niobium *Phys. Rev. B* **32** 2178-83

[139] Igata N, Miyahara K, Ohno K and Hakomori K 1982 Detrapping of nitrogen and oxygen atoms from neutron irradiation induced defects of niobium during post-irradiation annealing *J. Nucl. Mater.* **108 & 109** 234-9

[140] Hautojärvi P, Huomo H, Puska M and Vehanen A 1985 Vacancy recovery and vacancy-hydrogen interaction in niobium and tantalum studied by positrons *Phys. Rev. B* **32** 4326-31

[141] Wechsler M S and Murty K L 1989 Impurity-defect interactions and radiation hardening and embrittlement in bcc metals *Metall. Trans. A* **20A** 2637-49

[142] Brown B S, Blewitt T H, Scott T L and Klank A C 1974 Low-temperature fast-neutron radiation damage studies in superconducting materials *J. Nucl. Mater.* **52** 215-28

[143] Wallace J P 2011 Proton in SRF niobium. In: *Symposium on the Superconducting Science and Technology of Ingot Niobium*: (American Institute of Physics p 205)

[144] Sumin V V 1989 *Kristallografiya* **34** 655

[145] Schweizer H J and Gruehn R 1982 *Zeitschrift fuer Naturforschung, Teil B. Anorganische Chemie, Organische Chemie* **37**

[146] Gatehouse B M and Wadsley A D 1964 *Acta Cryst.* **17**

[147] Gupta M 1984 Why does hydrogen destroy superconductivity in niobium and lanthanum *Solid State Commun.* **50** 439-44

[148] Wachs I E, Chen Y, Jehng J M, Briand L E and Tanaka T 2003 *Catal. Today* **78**

[149] Dudarev S L, Botton G A, Savrasov S Y, Humphreys C J and Sutton A P 1998 *Phys. Rev. B* **57** 1505

[150] Wang L, Maxisch T and Ceder G 2006 Oxidation energies of transition metal oxides within the GGA + U framework *Phys. Rev. B* **73** 195107

[151] Internet Version 2013 *CRC Handbook of Chemistry and Physics* (Boca Raton, FL: CRC Press/Taylor and Francis)

[152] Sebastian J T, Seidman D N, Yoon K E, Bauer P, Reid T, Boffo C and Norem J 2006 Atom-probe tomography analyses of niobium superconducting RF cavity materials *Physica C* **441** 70-4

[153] Yoon K E, Seidman D N, Antoine C and Bauer P 2008 Atomic-scale chemical analyses of niobium oxide/niobium interfaces via atom-probe tomography *Appl. Phys. Lett.* **93** 132502

[154] Yoon K E, Seidman D N, Bauer P, Boffo C and Antoine C 2007 Atomic-scale chemical-analyses of niobium for superconducting radio-frequency cavities *Ieee T. Appl. Supercon.* **17** 1314-7

[155] Marucco J F 1978 Electrical resistance and defect structure of stable and metastable phases of the system Nb12029-Nb205 between 800 and 1100°C *J. Chem. Phys.* **70** 649-54

[156] Schmidt M W, Baldridge K K, Boatz J A, Elbert S T, Gordon M S, Jensen J H, Koseki S, Matsunaga N, Nguyen K A, Su S J, Windus T L, Dupuis M and Montgomery J A 1993 General Atomic and Molecular Electronic-Structure System *J. Comput. Chem.* **14** 1347-63

[157] Stevens W J, Basch H and Krauss M 1984 *J. Chem. Phys.* **81** 6026-33

[158] Becke A D 1993 *J. Chem. Phys.* **98** 5648-52

[159] 2010 *National Institute of Standards and Technology Computational Chemistry Benchmark DataBase* (http://cccbdb.nist.gov)

[160] Muller H and Weymann K 1986 *J. Less Comm. Metals* **119** 115

[161] Parlinski K, Li Z Q and Kawazoe Y 1997 *Phys. Rev. Lett.* **78**

[162] Hardcastle F D and Wachs I E 1991 Determination of niobium oxygen bond distances and bond orders by Raman-spectroscopy *Solid State Ionics* **45** 201-13

[163] Jehng J M and Wachs I E 1991 Structural chemistry and Raman-spectra of niobium oxides *Chem. Mater.* **3** 100-7

APPENDIX 1. CALCULATIONS OF THE VIBRATIONAL SPECTRA OF ELECTROPOLISHING SOLUTION SPECIES

The Raman and IR spectra for species relevant to the EP solution were calculated using the GAMESS program [156] to aid in the interpretation of the spectra presented in Chapter 5. I modeled the plausible species as isolated gas phase molecules and used the Hartree-Fock method to solve the quantum mechanical system:

$$-\left(h_i + \sum_i (2J_i - K_i)\right)\phi_i = \varepsilon_i \phi_i$$

where ϕ_i are the orbitals, ε_i are the orbital energies, h_i is the kinetic plus potential energies, J_i is the Coulomb energy and K_i is the exchange energy. I used the SBK [157] basis set for these calculations, which includes pseudopotentials to describe the core electrons and Gaussian functions to describe the valance orbitals. One orbital quantum number past the ground state configuration was included, which allows for flexible descriptions of bonding between atoms. Diffuse functions were also used, which allows one to extend the basis set beyond the length of the orbitals to describe phenomena such as anions and hydrogen bonding. This method neglects electron correlation, so I add that contribution by performing DFT calculations using the B3LYP hybrid exchange-correlation functional [157, 158].

The vibrational frequencies were calculated in the harmonic approximation. The IR intensities were calculated from the dipole derivative tensor and the Raman intensities were calculated from the polarizability derivative tensor.

The frequencies and relative intensities are given in Table A1.1 and are in good agreement (within ~5%) with gas phase reference data available from NIST cccbdb [159].

Table A1.1. Vibrational frequencies and Raman and IR intensities for the gas phase model of plausible species existing in the electropolishing solution.

Location (cm^{-1})	Relative Intensity (%) Raman, IR	Location (cm^{-1})	Relative Intensity (%) Raman, IR
$HFSO_3$		FSO_3^{-1}	
3722	100, 50	1273	16, 100
1468	6, 100	1271	16, 100
1225	28, 59	1046	100, 15
1162	5, 31	667	12, 69
856	12, 84	561	5, 8
781	19, 63	560	5, 8
537	4, 11	515	12, 1
524	3, 5	379	3, 0
501	2, 10	377	3, 0
404	1, 8	H_3O^+	
365	2, 0	3651	18, 98
266	1, 27	3623	16, 100
H_2O		3533	100, 10
3876	30, 100	1643	4, 21
3769	100, 20	1639	3, 21
1624	2, 93	847	1, 92

Table A1.1. continued.

H_2SO_4		$H_3SO_4^+$	
	Relative Intensity (%)		Relative Intensity (%)
Location (cm^{-1})	Raman, IR	Location (cm^{-1})	Raman, IR
3755	100, 35	3629	100, 47
3718	91, 40	3613	61, 80
1452	5, 90	3599	47, 100
1203	25, 50	1445	9, 49
1162	4, 30	1136	3, 16
1149	5, 25	1131	3, 18
845	4, 100	1071	6, 22
799	29, 34	965	2, 70
543	3, 7	939	1, 85
532	4, 12	843	25, 9
491	2, 11	514	2, 4
427	1, 3	498	3, 8
369	2, 1	484	2, 12
304	0, 18	429	1, 9
219	3, 31	400	1, 5
HSO_4^{-1}		324	1, 43
3787	100, 6	273	1, 20
1280	7, 89	218	3, 15
1222	10, 100	SO_4^{-2}	
1133	8, 27	1030	33, 100
1030	47, 20	1028	34, 100
697	15, 68	1027	34, 100
559	2, 8	909	100, 0
550	3, 3	583	2, 4
538	7, 3	582	2, 4
409	1, 2	582	2, 3
389	1, 1	416	2, 0
56	2, 13	416	2, 0
HF		HFH^+	
4024	100, 100	3434	100, 77
FHF^-		3421	75, 100
1298	0, 100	1402	8, 43
1285	0, 2		
618	100, 0		

APPENDIX 2. CALCULATIONS OF THE PHONON SPECTRA OF THE OXIDES AND HYDRIDES OF NIOBIUM

Raman backscatter spectroscopy combined with DFT offers a direct approach to detecting imperfections in the niobium surface and subsurface that may play a critical role in the performance of an SRF cavity. The probing depth in pure Nb is approximately 10 nm, which is estimated from the skin depth of a 785 nm laser. Pure bcc Nb is not Raman active, so any backscatter signal would originate from surface oxides, dissolved or precipitated species in the subsurface region, or disorder in the crystal structure. The incorporation of impurities also increases the probing depth.

I calculated the phonon DOS for dissolved H, O, N, and C in bcc niobium and the niobium hydrides and oxides modeled in Chapters 5, 6, and 7; which can be compared with Raman spectra collected from niobium coupon samples and SRF cavity cutout samples to detect the presence of these structures. Additionally, the δ niobium hydride structure was modeled as NbH_2 (Fm-3m, 1 formula unit per unit cell); the calculated lattice parameters are less < 1% different from those determined experimentally [160]. The phonon spectra were calculated using the Phonon module in the MedeA software package. This program applies the direct method [161] for calculating vibrational frequencies and uses forces calculated with VASP. Supercells extending approximately 10 Å or more in each lattice direction were created to minimize the interactions between equivalent atoms in adjacent cells, and atoms were displaced 0.02 Å from their equilibrium positions for the force calculations.

The calculated vibrational frequencies for the interstitial impurities in bulk bcc niobium are presented in Table A2.1, which indicates where we may expect to observe Raman activity for these species alloyed with niobium.

Table A2.1. Vibrational frequencies of interstitial impurity atoms in the bcc niobium lattice from DFT calculations. H is in a tetrahedral lattice interstitial site and O, N, and C are located in octahedral lattice interstitial sites.

	H	O	N	C
Mode 1 (cm^{-1})	968	307*	423*	489*
Mode 2 (cm^{-1})	1404*	698	759	806

* doubly degenerate

The calculated phonon DOS of NbO, NbO_2, and two Nb_2O_5 structures are presented in Figure A2.1. NbO does not have any Raman active modes. The Raman spectra of the oxides are available in the literature, and particularly, the calculated phonon DOS for Nb_2O_5 agrees well. The location of the modes depends on the Nb-O bond lengths [162] and degree of distortion of the octahedra [163]. Amorphous oxides are not Raman active, so if a signal is obtained, it indicates that a specific crystalline form of the oxide is present.

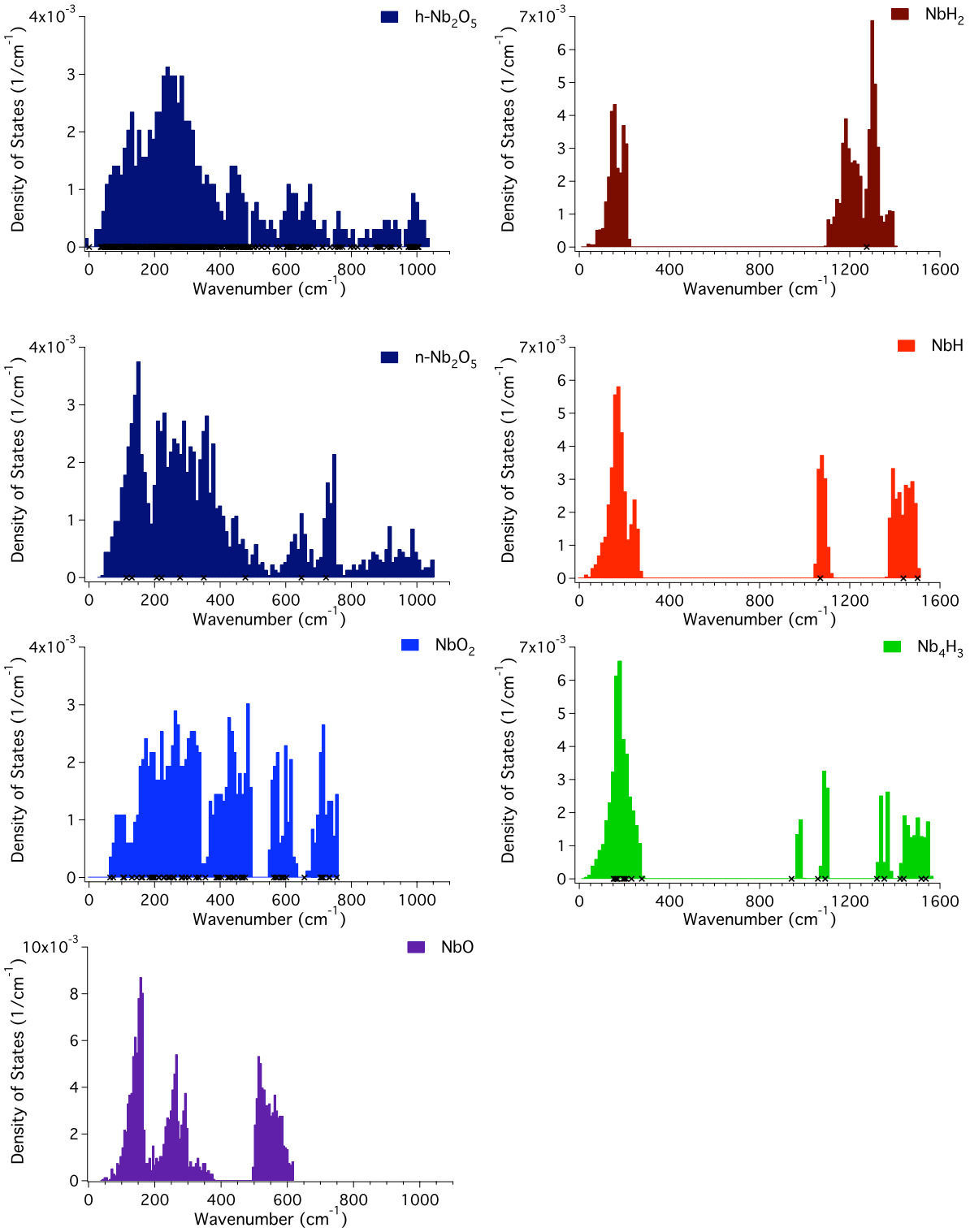

Figure A2.1. Phonon DOS of crystalline niobium oxides and hydrides. Raman active Gamma point modes are marked with a black 'x'.

Several spectra of a niobium sample cutout from a hot spot of an SRF cavity exhibiting high-field Q-slope are shown in Figure A2.2. They were obtained with the aid of Chaoyue Cao at the Illinois Institute of Technology using a Renishaw, inVia, Raman microscope with a 785 nm laser source and a 50X objective. Often the oxide is not detected, but occasionally clear oxide signals were obtained. The example spectrum shown was obtained near the edge of a topographical defect. Continued work in correlating the oxide spectra obtained from hot spots versus cold spots may lead to information about the role that the oxide plays in Q degradation.

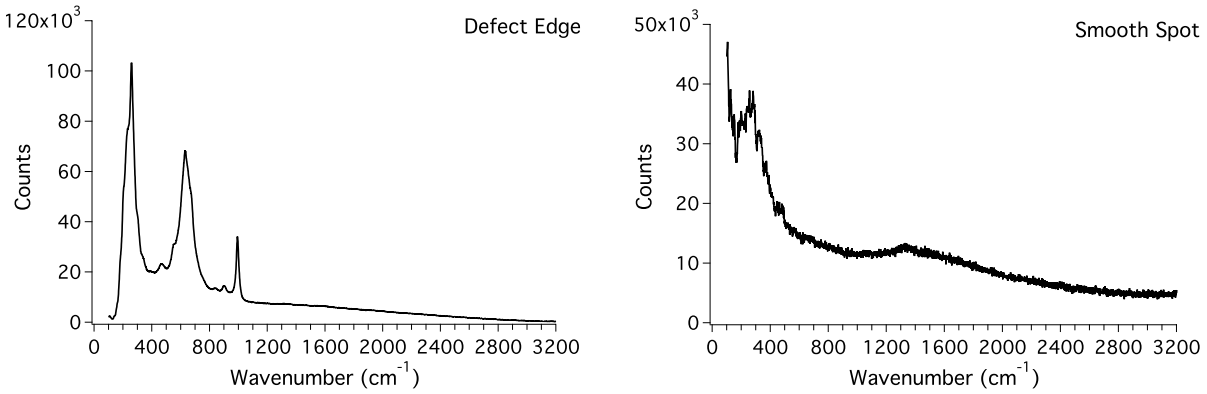

Figure A2.2. Raman spectra of the edge of a topographical defect and a smooth spot of a niobium sample cutout from a cavity high-field Q-slope hot spot.

The calculated phonon DOS for the niobium hydride modes are also shown in Figure A2.1, indicating that the hydrides should be easily distinguishable from the oxides. Typically a broad bump around 1350 cm^{-1} appears in the niobium spectra obtained at IIT, Figure A2.2, but we are not able to definitively assign any of the experimental spectra to the hydrides presently. The collaboration with IIT is ongoing.

VITA

Denise C. Ford

Education
M.S. Chemical Engineering, June 2009
Northwestern University, Evanston, IL

B.S. Chemical Engineering, August 2007
Certificate in Technical Communications, August 2007
University of Wisconsin, Madison, WI

Fundamentals of Accelerator Physics and Technology, June 2012
United States Particle Accelerator School / Michigan State University, Grand Rapids, MI

RF Technology Course, November 2011
Sixth International Accelerator School for Linear Colliders, Pacific Grove, CA

Publications
Denise C. Ford, Charlie Cooper, Lance D. Cooley, Chad Thompson, Donald Bouchard, Brian Albee, Sandra Bishnoi, "Chemical analysis of the fluorine in niobium electropolishing," submitted to *Journal of the Electrochemical Society*

Denise C. Ford, Lance Cooley, David Seidman, "Suppression of hydride precipitates in niobium superconducting radio-frequency cavities," submitted to *Superconductor Science & Technology*

Denise C. Ford, Lance Cooley, David Seidman "First principles calculations of niobium hydride formation in superconducting radio-frequency cavities," submitted to *Superconductor Science & Technology*

Denise C. Ford, David Dubbeldam, Randall Q. Snurr, Volker Künzel, Markus Wehring, Frank Stallmach, Jörg Kärger, Ulrich Mueller, "Self-diffusion of chain molecules in the metal-organic framework IRMOF-1: Simulation and experiment," *Journal of Physical Chemistry Letters* 2012, 3, 930-933

L. D. Cooley, D. Burk, C. Cooper, N. Dhanaraj, M. Foley, D. Ford, K. Gould, D. Hicks, R. Novitski, A. Romanenko, R. Schuessler, C. Thompson, and G. Wu, "Impact of forming, welding, and electropolishing on pitting and the surface finish of SRF cavity niobium," *IEEE Transactions on Applied Superconductivity* 2011, 21, 2609-2614

Denise C. Ford, Anand U. Nilekar, Ye Xu, Manos Mavrikakis, "Partial and complete reduction of O_2 by hydrogen on transition metal surfaces," *Surface Science* 2010, 604, 1565-1575

Denise C. Ford, David Dubbeldam, Randall Q. Snurr, "The effect of framework flexibility on diffusion of small molecules in the metal-organic framework IRMOF-1," *Diffusion Fundamentals III*, edited by C. Chmelik, N. Kanellopoulos, J. Kärger, D. Theodorou, Leipziger Universitatsverlag, Leipzig, 2009, 459-466

David Dubbeldam, Denise C. Ford, Donald E. Ellis, Randall Q. Snurr, "A new perspective on the order-n algorithm for computing correlation functions," *Molecular Simulation* 2009, 35, 1084-1097

Z. Gerald Liu, Denise C. Ford, Victoria N. Vasys, Da-Ren Chen, Timothy R. Johnson, "Influence of engine operating conditions on diesel particulate matter emissions in relation to transient and steady-state conditions," *Environmental Science & Technology* 2007, 41, 4593-4599

Denise C. Ford, Ye Xu, Manos Mavrikakis, "Atomic and molecular adsorption on Pt(111),"*Surface Science* 2005, 587, 159-174 – ***Surface Science 'Top Cited Articles' list 2005-2010***

Presentations

The detection and role of a molecular reservoir for fluorine in the electropolishing of niobium SRF cavities, poster presented at the Applied Superconductivity Conference, Portland, OR, 2012

A first principles investigation of impurities in niobium, talk presented at the Applied Superconductivity Conference, Portland, OR, 2012

DFT Analyses of structures that limit SRF cavity performance, talk presented at the 7th SRF Materials Workshop, Newport News, VA, 2012

Building the next generation of particle accelerators: Atomic scale insight to the mechanisms of cavity limitation, poster presented at the 45th Fermilab Users Meeting, Batavia, IL, 2012

First principles investigation of processing impurities in niobium superconducting radio-frequency cavities, poster presented at the Gordon Research Conference and Gordon-Kenan Research Seminar on Physical Metallurgy, Easton, MA, 2011 – ***Awarded one of the top five student poster presentations***

First principles investigation of hydrogen in niobium, poster presented at the 15th International Conference on RF Superconductivity, Chicago, IL, 2011 – ***Awarded 2nd place in the student poster competition***

Electropolishing superconductors: Understanding chemistry via density functional theory and spectroscopy, poster presented at USC-DOE Emerging Trends in Materials Simulations and Experiments Conference, Rancho Palos Verdes, CA, 2010

Molecular dynamics studies of n-alkane and benzene self-diffusion in the metal-organic framework IRMOF-1, talk presented at 2009 Midwest Thermodynamics and Statistical Mechanics Conference, Detroit, MI, 2009

Design and validation of a diesel exhaust speciation test stand, poster presented at Cummins World Wide TSFE Conference, Columbus, IN, 2006

Low temperature fuel cells – A first principles study, poster presented at UW-Madison Undergraduate Research Symposium, Madison, WI, 2003

Patent

Z. Gerald Liu, Thaddeus A. Swor, Joseph C. Lincoln, Denise C. Ford, "Source dilution sampling system for emissions analysis," US Patent Number 7587950, 2009